

TWO ZONE SSC MODEL FOR BLAZAR JETS

DIPLOMA THESIS

BY

LEONARD BURTSCHER



LEHRSTUHL FÜR ASTRONOMIE

INSTITUT FÜR THEORETISCHE PHYSIK UND ASTROPHYSIK
BAYERISCHE JULIUS-MAXIMILIANS-UNIVERSITÄT WÜRZBURG

WÜRZBURG, JULY 2007

Contents

1	Introduction	1
1.1	Blazars in the unified model of Active Galactic Nuclei	1
1.2	AGN Jet Modelling	3
1.3	Outline	4
2	Theoretical Background	7
2.1	AGN ingredients	7
2.1.1	Relativistic Jet(s)	7
2.1.2	Cosmological redshift	9
2.1.3	Particle Acceleration at Shock Fronts	10
2.2	Radiation Processes	13
2.2.1	Definitions	13
2.2.2	Overview of relevant loss processes for electrons	14
2.2.3	Photon losses	16
2.2.4	Synchrotron Radiation	16
2.2.5	Inverse Compton Effect	18
2.3	Luminosity distance	22
2.4	Extragalactic Background Light (EBL)	22
2.5	Data fitting	23
3	Analytic Model	25
3.1	Generic Blazar SED	25
3.2	Homogeneous two zone model	26
3.3	Acceleration zone	27
3.3.1	Kinetic Equation	27
3.3.2	Solution	28
3.4	Radiation Zone	32
3.4.1	Kinetic Equation	32
3.4.2	Analytic Approximation for x_{cool} ?	37

3.5	Synchrotron Spectrum	39
3.5.1	Contribution from the acceleration zone	39
3.5.2	Contribution from the radiation zone	40
3.5.3	Transformation to the observer's frame	40
3.5.4	Synchrotron fit for Markarian 501	41
4	Inverse Compton (IC) contribution	43
4.1	Extension of the model	43
4.2	Computation of the IC spectrum	44
4.3	Time-dependent Inverse Compton Spectrum	45
4.4	SSC fit for Mrk 501	46
5	Variability	49
5.1	Modelling a flare	49
5.2	Flaring behaviour I: Intensity profiles	50
5.3	Flaring behaviour II: Spectral Index variation	53
5.4	Variation of spectral index with flux (Hysteresis)	53
5.5	Timescales	58
5.6	Observations of variable high-energy spectra	59
6	Summary and Discussion	61
6.1	Summary	61
6.2	Discussion	62
6.3	Prospects	64
7	Zusammenfassung (German Summary)	65
	Bibliography	69
A	Acknowledgements	73
B	Numerical Calculations with Mathematica	75
C	Program Listing	77
C.1	Init.nb	77
C.2	Run.nb	81
D	Eigenständigkeitserklärung (Declaration of Autonomy)	87

1 Introduction

Blazar jet modelling is a tightly interconnected field of study. If one could study a relativistic jet with sufficiently high temporal and spatial resolution and over large enough times, one could resolve many of the issues discussed below. But, as astronomy is the science of observation – not experimentation –, one has to be content with what can be observed from earth, although many such observations do not stand for themselves but depend on a couple of other unsolved problems. I want to show up some of these interconnections in this introduction, concentrating more on the details in the following sections.

1.1 Blazars in the unified model of Active Galactic Nuclei

The systematic study of active galactic nuclei began about twenty years after Edwin Hubble showed in 1923 that the Andromeda ‘Nebula’ was in fact a galaxy far away and not some nearby galactic nebulous object. In 1943, Carl Seyfert obtained spectrograms with emission lines of several galaxies clearly demonstrating the non-stellar origin of the radiation coming from the very centre of star-like galaxies.

The amount of radiation coming from these galaxies’ core regions which have diameters of the order of parsecs or less, sometimes can exceed the radiation from the entire rest of the galaxy with hundreds of billions of stars spread over typical diameters of 30 kpc. As nuclear fusion is not efficient enough to produce luminosities as high as the ones observed in such a small volume, more efficient emission mechanisms were sought, and found: Nowadays there is little doubt that the so called active galactic nuclei (AGN) are powered by accretion onto a central supermassive black hole with typically some hundred million solar masses (Rees 1984).

Interestingly many of these AGN drive jets of several kiloparsecs length into the intergalactic medium. The exact mechanism for the production of these jets is still not entirely clear although many ideas have been proposed (Blandford and Znajek 1977; Meier et al 2001). In any case, the visibility of the jet to an observer on earth seems to depend mostly on the angle between the jet axis and the line of sight. In the unified model for

1 Introduction

AGN, see Fig. 1.3 for an illustration and Antonucci (1993); Urry and Padovani (1995) as a reference, the line of sight and possibly the spin of the central black hole determine the appearance and radio-loudness of an AGN. For example, a blazar, and in particular BL Lac objects, which are the most extreme AGN with the shortest time variabilities, is a radio-loud active galaxy observed under a very small angle to the jet. This is the type of galaxy I want to focus on for this thesis. Due to special relativistic effects, variability times in blazars appear to be shorter, radiation appears to be bluer and luminosities appear to be higher than in radio galaxies (that are more or less "edge-on" active galaxies). For recent reviews see (Mukherjee 2002; Coppi 2002).

While the galaxy's radiation is dominated by the thermal emission from stars, the core and jet of an AGN are dominated by a wide range of nonthermal and line emission from radio to ultra-high-energy gamma rays. In the case of blazars, no emission lines are seen which is generally attributed to the fact that the jet's emission is so strongly Doppler boosted (see section 2.1.1) that it outshines the line emission from the (broad and narrow line) clouds at the centre of the AGN. The fact that no emission lines are seen also implies that the target radiation for inverse Compton radiation (see section 2.2.5) is dominated by the synchrotron emission of the jet, therefore an SSC model (see later) appears very attractive for blazars. A blazar's spectrum can roughly be described as a double hump structure in the spectral energy distribution of the emitted photons. The origin of these two humps has been discussed extensively in the literature, see chapter 1.2 for an overview and references.

Apart from being one of the most luminous gamma-ray emitters in the known universe (and therefore their nature is important to understand anyway), the field of blazar research is intimately connected to several other areas of current research. Concerning accretion, the production and emission mechanism of jets, microquasars exhibit very similar phenomena, when reducing the relevant scales to the respective central mass – a super massive black hole of several million solar masses in the case of AGNs and a stellar mass black hole in the case of microquasars (see Fig. 1.1).

Even stronger is the link between blazars and early star formation and cosmology as the TeV photons emitted by the blazar jets are attenuated due to $\gamma\gamma \rightarrow e^+e^-$ pair production. The cross section for this process is largest when $\epsilon_{\text{IR}} \approx 2(mc^2)^2/E_\gamma = 0.5(1\text{TeV}/E)\text{ eV}$, corresponding to a wavelength of $\approx 2.5\mu\text{m}$ for a 1 TeV photon, which is just the wavelength where dust-enshrouded galaxies emit. Lower energy photons will be absorbed by near-IR, optical or UV photons that come predominantly from stars. What at first sight appears to be a disadvantage to blazar research (only nearby blazars will be seen at energies above 1 TeV) is at second sight a unique probe for star-formation in the

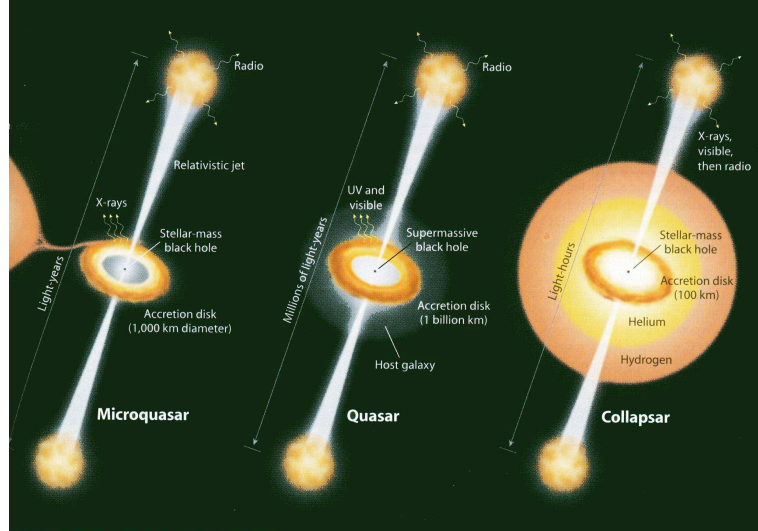


Figure 1.1: *The ‘microquasar connection’ suggests that similar processes are at work in quasars, microquasars and Gamma Ray Bursts alike with time scales scaling according to the mass of the central black hole. By observing both microquasars and ‘real’ quasars, different time scales can thus be probed. Image credit: Mirabel and Rodriguez (2002)*

early universe.

1.2 AGN Jet Modelling

Many models have been constructed to account for the multitude of AGN observations. Generally one has to distinguish between leptonic and hadronic models. In hadronic models protons are accelerated to very high energies ($\approx 10^{20}$ eV) and initiate synchrotron cascades that are responsible for the spectra we see (Mannheim 1993). These models are promising as they could also explain the origin of Cosmic Rays that are seen up to such high energies. A possible verification of these models would be neutrino emission from extragalactic point sources – but the angular resolution of today’s neutrino telescopes unfortunately is not good enough yet to detect those.

In leptonic models, the dynamical content of the jet is electrons and positrons that are responsible for the synchrotron radiation and upscatter photons to very high energies. The source of those low-energy photons (‘seed photons’) differs depending on the flavour of the leptonic model. In so called ‘External Compton’ models the seed photons come from the accretion disk (Dermer and Schlickeiser 1993) or are reflected into the jet by surrounding material (Sikora et al 1994) and numerous other sources of seed photons have also been proposed. The most widely used and, indeed, most successful model for AGN jets has proven to be the so called ‘Synchrotron Self-Compton’ (SSC) model, where

synchrotron photons are Compton up-scattered by the very same high energy electrons that produced them via synchrotron radiation in the first place. SSC models are popular as in those models X-ray flares are naturally correlated with VHE flares, as observed. Those correlated flares can also be produced in the context of hadronic models (e.g. Rachen 2001; Mannheim and Biermann 1992) but the calculations involved are a little more complicated than with the SSC model, so – for economy and for the sake of Occam’s razor – SSC models are the ones that are most widely ones.

Within those models one further distinguishes between homogeneous and inhomogeneous models with the former consisting of a constant magnetic field and particle distribution function throughout the source region. This constraint is dropped in the inhomogeneous models.

Further distinctions can be made regarding the number of electron populations (e.g. to account for a low-energy radio emission of the jet and a variable high-energy emission of a blob) and, importantly, the number of zones the source region consists of. While one zone models inject a distribution of high-energy electrons, two zone models can also explain the acceleration, thus producing some spectral features that one-zone models cannot explain as will be seen.

1.3 Outline

In chapter 2 the physical processes and mathematical relations relevant for the model are explained such as relativistic Doppler boosting, (a simplistic view of) particle acceleration at shock fronts and synchrotron and inverse Compton radiation formulae. The analytic model of Kirk et al (1998) is explained and some minor corrections are given in chapter 3. Here it will become clear why it is necessary to use numerical calculations in deriving the IC spectrum. In chapter 4 the assumptions and simplifications are given that lead to the IC spectrum and a sample SSC fit for the Mrk 501 spectral energy distribution (SED) is given. The time-dependence of the model will be discussed in chapter 5 where the evolution of the spectrum and spectral index during a flare is shown. Chapter ?? will give a brief overview of the currently available very high energy data on hour-scale variability and discuss the possibility of future (multiwavelength) observations. In chapter 6 a brief summary is given and some of the limitations of the model are discussed and possibilities to validate or falsify the model are pointed out.

In appendix B a brief explanation of the Mathematica program written for the calculation of the spectra is given, I want to thank several people in appendix A and appendix D contains the mandatory Declaration of Autonomy.

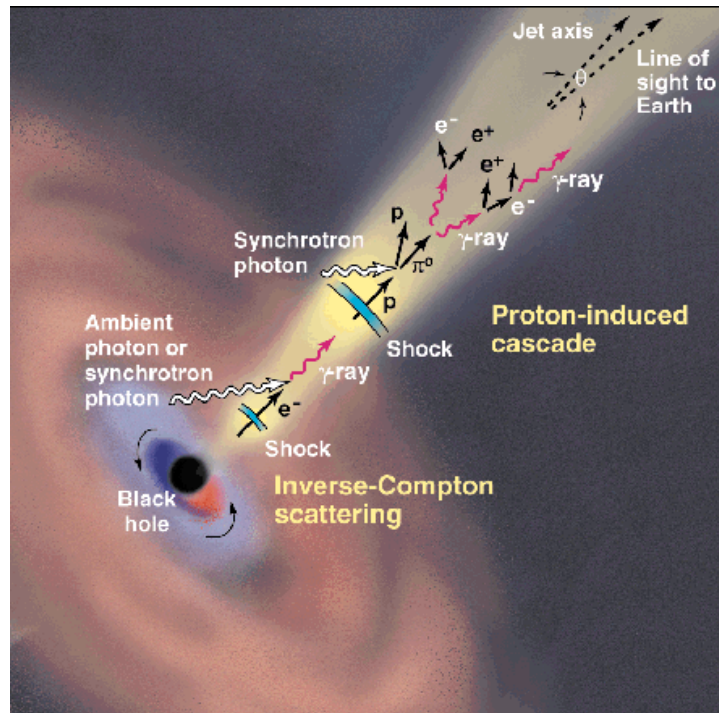


Figure 1.2: ‘The Cosmic Cascade’, an illustration by K. Sutliff from Buckley (1998), depicting various scenarios for gamma-ray production in AGN jets, see chapter 1.2.

All calculations and units are written in the CGS system for better comparability with the relevant literature.

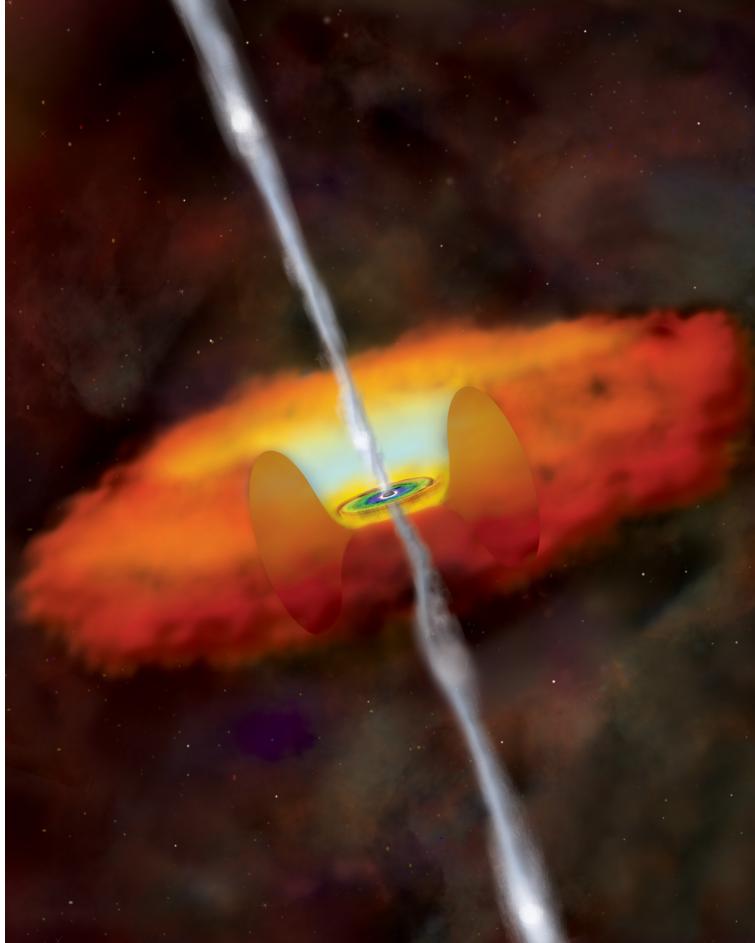


Figure 1.3: *An illustrative drawing showing the main ingredients of an active galactic nucleus: Surrounded by an accretion disk a supermassive black hole with Schwarzschild radius $R_S \approx 1.5 \cdot 10^{13} \text{cm} \frac{M_{\text{BH}}}{10^8 M_{\odot}}$, weighing some $10^6 \dots 10^8 M_{\odot}$, is thought to be the ultimate power source of AGN. Further out the scenario is enshrouded by an opaque dusty torus with $R \approx 1 \text{pc} = 3.09 \cdot 10^{18} \text{cm}$. In the symmetry axis of the accretion disk a relativistic jet streams outward, well collimated by magnetic fields that have been greatly amplified in the accretion process. Image Credit: NASA/CXC/M. Weiss*

2 Theoretical Background

This chapter gives an overview of the theoretical background, including the relevant formulae, for the calculations done in this work. As the model describes radiation coming from relativistic jets I will give the relevant relativistic transformation formulae. A main part of this chapter covers particle acceleration (at shock fronts) where I want to justify the use of an energy-independent ‘acceleration time’ in the model. After some definitions concerning radiation processes, loss mechanisms for high energy electrons traversing dilute plasmas will be discussed, finding that only synchrotron and Inverse Compton losses are relevant here. Those two processes are then discussed in greater detail. The section on the ‘luminosity distance’ will explain how the distance to a blazar can be calculated from the observationally measured redshift z . For large z or very high energies (VHE, above 100 GeV), the Extragalactic Background Light (EBL) attenuates high-energy gamma radiation. Although all data points used are already unfolded for EBL absorption, i.e. the spectra used are the ones one would see on earth if there were no EBL, I will give a short explanation of why EBL is important for blazar spectra modellers. Finally, a section on data fitting describes the commonly used χ^2 value to test the quality of a fit.

2.1 AGN ingredients

2.1.1 Relativistic Jet(s)

The jets of AGN show several remarkable features: they are very well collimated over vast distances, sometimes up to a MPc, show (apparent) superluminal motion of individual ‘knots’, as identified by radio interferometry, and have highly variable polarised emission from radio to gamma-rays – sometimes on the order of minutes. In some sources only one jet is visible and the termination shock of the presumed ‘counter-jet’ seems to come from nowhere. Some of these phenomena can easily be explained by the relativistic Doppler effect.

Relativistic Doppler Effect

Let us look at the Doppler factor δ for a blob of matter moving relativistically towards an observer in a relativistic jet

$$\delta = [\Gamma(1 - \beta \cos \theta)]^{-1} \quad (2.1)$$

$\Gamma = (1 - \beta^2)^{-1/2}$, the (bulk) Lorentz factor of the blob, $\beta = \frac{v}{c}$ and θ is the angle between the line of sight and the direction of motion of the jet / blob.

To get rid of θ , let us have a look at blazars where $\cos \theta \approx 1$ and one can write

$$\delta \approx [\Gamma(1 - \beta)]^{-1} = [\Gamma(1 - \beta)(1 + \beta)(1 + \beta)^{-1}]^{-1} \approx 2\Gamma \quad (2.2)$$

Several observable quantities are transformed by the Doppler factor, see Blandford and Konigl (1979) for detailed calculations. I will express the relevant transformations here in terms of Γ for better comparability with blazar models. All quantities in the blob frame are denoted by $_{em}$, quantities in the observer's frame by $_{obs}$.

Due to relativistic dilation, time scales are shortened in the observer's frame with respect to the jet frame,

$$t_{obs} = \frac{t_{em}}{\Gamma}, \quad (2.3)$$

frequencies are shifted towards higher values,

$$\nu_{obs} \approx 2\Gamma\nu_{em}, \quad (2.4)$$

and intensities are 'boosted' to

$$I_{obs}(\nu_{obs}) \approx (2\Gamma)^{3-\alpha} I_{em}(\nu_{obs}) \quad (2.5)$$

The intensity transformation ('Doppler boosting') can hand-wavingly be explained by attributing two factors of Γ to the effect of relativistic aberration (radiation is only emitted in a narrow cone of half angle Γ) and one that comes from time dilation of the dt in the definition of the intensity (see chapter 2.2.1). The additional factor of $(2\Gamma)^\alpha$ accounts for the blue-shift of the intensity.¹

Now one-sided jets can readily be explained as one of them being 'Doppler boosted' while the other, moving away from us (with $\cos \theta < 0$ in Eq. (2.1)), being 'Doppler de-boosted'

¹Since the specific intensity is assumed to be $I_\nu \propto \nu^\alpha$, this is equivalent to $I_{obs}(\nu_{obs} \approx 2\Gamma\nu_{em}) \approx 8\Gamma^3 I_{em}(\nu_{em})$.

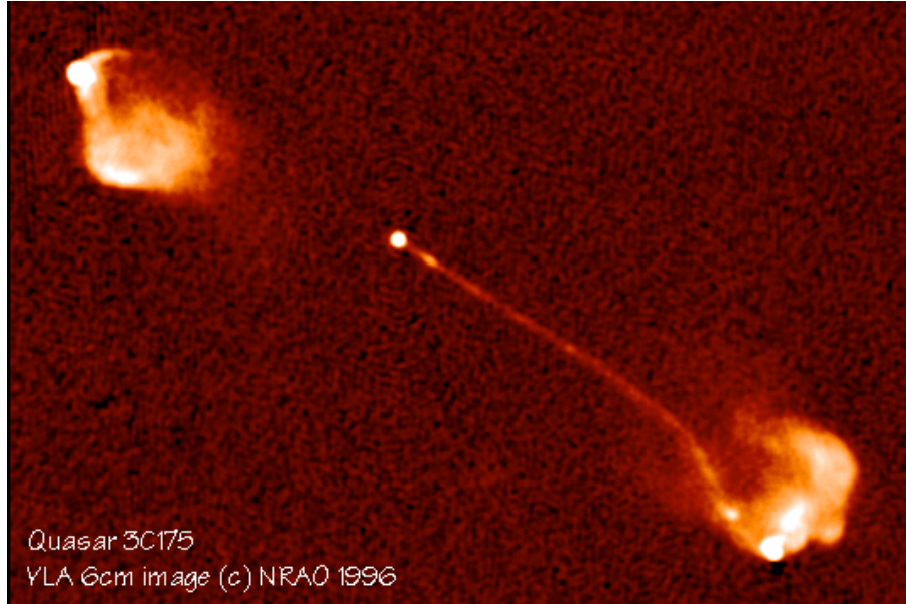


Figure 2.1: A radio image of the quasar 3C175 (the tiny bright spot in the centre), its over a million light years long one-sided radio jet and its radio lobes. Although this jet is not thought to be directed at a very small angle towards an observer (3C175 is no blazar), the angle between the jet and the line of sight might still be narrow enough that a possible counter-jet is ‘Doppler-hidden’ and so we only see one jet. Large radio lobes are seen on both sides of the quasar as here the bulk motion is thought to be non-relativistic, allowing the electrons to radiate their synchrotron emission isotropically. Also visible is another characteristic of radio galaxies: the hot spots, the very bright spots visible in both lobes where the jets are thought to collide with the intergalactic medium. Image Credit: Alan Bridle (NRAO Charlottesville) VLA, NRAO, NSF

and thus emission from the far side of the AGN is only visible when the motion has slowed down to sub-relativistic speeds (see Fig. 2.1).

2.1.2 Cosmological redshift

To fully switch to the observer’s frame one further has to take into account the cosmological redshift z so that the transformation formula for the frequencies becomes

$$\nu_{obs} \approx \frac{2\Gamma}{1+z} \nu_{em} \quad (2.6)$$

For the two best studied nearby BL Lac objects Mrk 421 and Mrk 501, z is ≈ 0.03 , TeV blazars have been detected up to $z = 0.186$ (Aharonian et al. (H.E.S.S. collaboration) 2007) with a possible detection at $z = 0.74$ (Albert et al. (MAGIC collaboration) 2007a) and the highest redshift blazar detected so far being at $z \approx 5.5$ (Romani 2006). Those very

distant blazars are not detectable at very high energies, however, as high-energy gamma-rays are efficiently absorbed by Extragalactic Background Light (EBL, see section 2.4).

2.1.3 Particle Acceleration at Shock Fronts

A mechanism is needed to explain the acceleration of charged particles up to energies of 10^{20} eV and possibly beyond (Sigl 2001) that we see in the form of isotropic cosmic rays. Also, the nearly perfect power-laws both in the energy distribution of these cosmic rays and in the spectra of most extragalactic nonthermal sources such as radio galaxies and quasars need theoretical understanding.

As Longair (1994) has noted, it is ironic that we have to build the world's largest experiments to accelerate particles to a mere 10^{12} eV, but when we try to store high-temperature plasmas inside a fusion reactor, we run into trouble because of numerous plasma instabilities that readily accelerate particles to suprathermal energies. As it is generally implausible that natural mechanisms rely on extremely fine-tuned 'machines', a simple process is sought to produce power-laws that reach up to very high energies.

Long before sophisticated plasma instabilities could be calculated to great detail numerically, Enrico Fermi has come up with a simple, yet brilliant idea (Fermi 1949). Trying to explain the origin of cosmic rays, he presumed that particles were accelerated in the interstellar space of the galaxy by the 'collision against moving magnetic fields', nowadays known as collisionless shock acceleration. The term 'collisionless' refers to the fact that particles in tenuous interstellar plasmas get scattered only via collective plasma interactions and not by their immediate electric fields.

There are two classes of approaches to calculate the spectra that would result from such a physical scenario: one can either treat the interstellar plasma as a fluid, model the shock using the magnetohydrodynamic (MHD) approximation and put in particles using test-particle simulations, or one can use the more physical microscopic approach and follow the particles' distribution function, the diffusion-loss equation. While the first method is more suited for incorporating many concurring effects and numerically calculating the resulting spectra, kinetic equations for distribution functions can more easily describe physical processes that are self-similar over several orders of magnitude in particle energy. Also, only the kinetic approach is suited for analytic calculations giving greater insight into the physics going on but with the disadvantage of requiring some crude approximations to keep the equations simple.

Here, only the original version of Fermi acceleration ('second order Fermi') shall be discussed briefly to justify the energy-independent 'acceleration time' used in the model to

describe particle acceleration. A good starting point for a more detailed overview of shock acceleration and an enjoyable reading for almost any topic in high energy astrophysics is Longair (1994). Jones and Ellison (1991) cover the plasma physics of shock acceleration in parallel shocks (the simplest scenario, where the magnetic field direction is parallel to the normal of the shock front), give a review of computer simulations and introduce to nonlinear theories for shock acceleration.

The second order Fermi Mechanism of particle acceleration Consider a particle's reflection off an infinitely massive² 'magnetic mirror' – in reality that might be a massive cloud of plasma – moving at an average velocity V relative to the particle. The mirror reflects the particle so that the angle between the initial direction of the particle and the normal of the mirror is θ . Then the particle's energy is conserved in the collision and its momentum reversed.

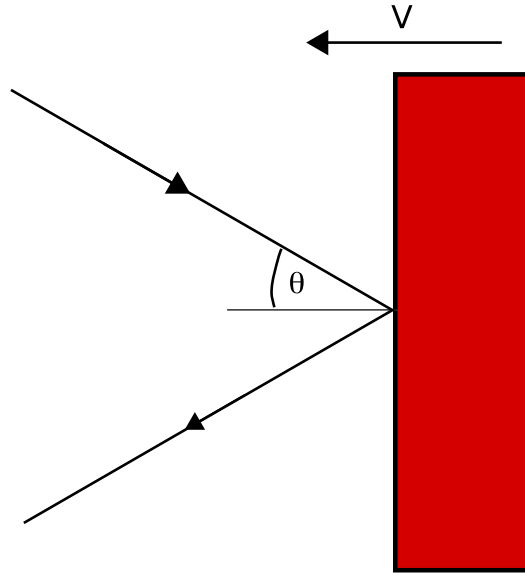


Figure 2.2: A particle of speed c collides head-on with a 'magnetic mirror' of infinite mass moving at velocity V and subtends an angle θ between the incoming direction and the mirror's normal.

Working out the relativistic transformations – into the cloud's frame (the centre of momentum frame) and back into the observer's frame – and expanding in second order of V/c , one readily arrives at, assuming the particle's velocity is c ,

$$\frac{\Delta E}{E} = \frac{2V \cos \theta}{c} + 2 \left(\frac{V}{c} \right)^2 \quad (2.7)$$

²so that its velocity is unchanged by the collision

2 Theoretical Background

From this equation one can easily see that, when $\cos \theta = 1$, i.e. when only head-on collisions are considered, the energy gain is first order in V/c which is the outcome of the so-called ‘Fermi I’ mechanism. Now for Fermi II, let us assume that particles quickly lose their directional information due to isotropic ‘pitch-angle scattering’ (the pitch-angle is the angle between the direction of motion of the particle and the magnetic field) in the irregular magnetic fields of the clouds. They will then leave the cloud isotropised so that we can average over all angles to get the average energy gain of a particle

$$\left\langle \frac{2V \cos \theta}{c} \right\rangle = \frac{2}{3} \left(\frac{V}{c} \right)^2 \quad (2.8)$$

Thus, one arrives at the famous result first derived by Fermi

$$\frac{\Delta E}{E} = \frac{8}{3} \left(\frac{V}{c} \right)^2 \quad (2.9)$$

stating that the energy gain is only second order in V/c .

Second order Fermi acceleration was originally applied to randomly moving clouds and Fermi could demonstrate that statistical acceleration leads to a power law energy spectrum. Although in strong shocks Fermi I acceleration is normally said to be more efficient, this is not true when considering also decelerating effects. In fact, the acceleration efficiencies of Fermi I and II are not much different, even in strong shocks (Jones 1994). Furthermore, large shocks are not expected at the base of the jet where the gamma radiation is thought to originate (Pelletier 1997) so that Fermi II seems to be a plausible mechanism there albeit with some difficulties and limitations (see below).

To derive the fractional increase per unit time, we further need to consider the time between collisions which is given by $2L/c$ when L is the mean free path between clouds. So the rate of energy increase is then given by

$$\frac{dE}{dt} = \frac{4}{3} \left(\frac{V^2}{cL} \right) E = \frac{E}{t_{acc}} \quad (2.10)$$

This is a very important and useful equation as it says that particles are accelerated within an energy-independent acceleration time t_{acc} . With the further assumption that the particle will leave (‘escape’) the acceleration region after a time t_{esc} , we can substitute the relevant expressions in the equation describing the evolution of the electron density Eq. (3.2) and get

$$-\frac{d}{dE} \left[\frac{E}{t_{acc}} N(E) \right] - \frac{N(E)}{t_{esc}} = 0 \quad (2.11)$$

The solution to this equation is the simple power-law relation

$$N(E) \propto E^{-x} \quad (2.12)$$

with $x = 1 + t_{acc}/t_{esc}$. The choice of $t_{acc}/t_{esc} = 1/2$ leads to the desired (i.e. measured) low-frequency spectral index $\alpha = 0.25$. Taking synchrotron losses (chapter 2.2.4) into account, we will get a spectral break at a characteristic energy where cooling and escape are balanced and the electron spectrum will steepen by 1, i.e. from 1.5 to 2.5, see chapter 3.1.

This mechanism has received much attention because it explains naturally the power-law shape of the spectrum. Another benefit is that this mechanism works ‘in situ’, i.e. particles are accelerated where the energetic phenomena like strong shocks are, thus avoiding adiabatic (expansion) losses. But we had to put in $t_{acc}/t_{esc} = 1/2$ a posteriori to get the desired spectral index of 2.5 which fits very well to the power-law spectra of radio-sources and is close enough to the one measured over most part of the cosmic ray spectrum (2.7). Also, losses in the acceleration process such as ionisation losses and geometrical effects expected to arise in non-parallel shocks have not been considered and are expected to modify the spectrum more or less dramatically. Furthermore, this has only been a test particle approach where the back-reaction effects of the particles on the shock are neglected. For a recent review of the applicability of Fermi acceleration to astrophysical jets see Rieger (2006).

Although there are certainly many objections to this simple picture of particle acceleration at shock fronts, it can nonetheless be used as a simple method to implement acceleration in a time-dependent model of blazar spectra.

2.2 Radiation Processes

2.2.1 Definitions

For the further discussion we need a few definitions concerning radiative processes (Rybicki and Lightman 1979). When calculating the synchrotron and Inverse Compton spectrum, one usually gets the spectrum in the form of the specific intensity:

$$I_\nu = \frac{dI}{d\nu} = \frac{dE}{dA \cos \theta dt d\nu d\Omega} \quad [\text{erg cm}^{-2} \text{s}^{-1} \text{Hz}^{-1} \text{sr}^{-1}] \quad (2.13)$$

where I , the intensity ($\text{erg cm}^{-2} \text{s}^{-1} \text{sr}^{-1}$), is the amount of energy E received in the area dA (perpendicular to the direction of incidence of the radiation) in the time dt , frequency

interval $[\nu, \nu + d\nu]$, from the solid angle $d\Omega$.

For an unresolved source, i.e. a source which appears smaller than the smallest resolved angle θ_{min} , the specific radiative flux is more appropriate

$$F_\nu = \int d\Omega \cos \theta I_\nu \quad (2.14)$$

For the graphical display, one usually plots $\log \nu F_\nu$ on the ordinate and $\log \nu$ on the abscissa as this is a plot of logarithmic radiation energy density per logarithmic frequency interval and therefore it is easy to see at which frequencies most of the radiation energy density is: an equal amount of energy emitted per logarithmic frequency interval would be a horizontal line.

2.2.2 Overview of relevant loss processes for electrons

Four main processes are to be discussed when considering the problem of a high energy electron traversing a dilute partially ionised gas (Blumenthal and Gould 1970). Here I will give a brief overview and then discuss in more detail the two most important ones in this context: synchrotron and Inverse Compton radiation. See Schlickeiser (2002, p. 100 et seq.) for a detailed account of all processes possible.

None of the following processes causes more losses for an electron in a blazar than synchrotron and IC losses (see Fig. 2.3).

Ionisation Losses / inelastic collisions occur when electrons scatter inelastically with other particles, thereby ionising them:

$$-\left(\frac{dE}{dt}\right)_{ion} = 7.64 \cdot 10^{-21} N (3 \ln \gamma + 19.8) \text{eV s}^{-1} \text{cm}^{-3} \quad (2.15)$$

where N is the number density of hydrogen atoms per cubic centimetre. Ionisation losses are only important at very low energies.

Bremsstrahlung – sometimes referred to as ‘free-free radiation’ – is emitted by the electrons in scatterings as they are deflected by the electric fields of other particles. In a fully ionised plasma the loss rate is:

$$-\left(\frac{dE}{dt}\right)_{brems} = 3.6 \cdot 10^{-23} N \gamma (\ln \gamma + 0.36) \text{eV s}^{-1} \text{cm}^{-3} \quad (2.16)$$

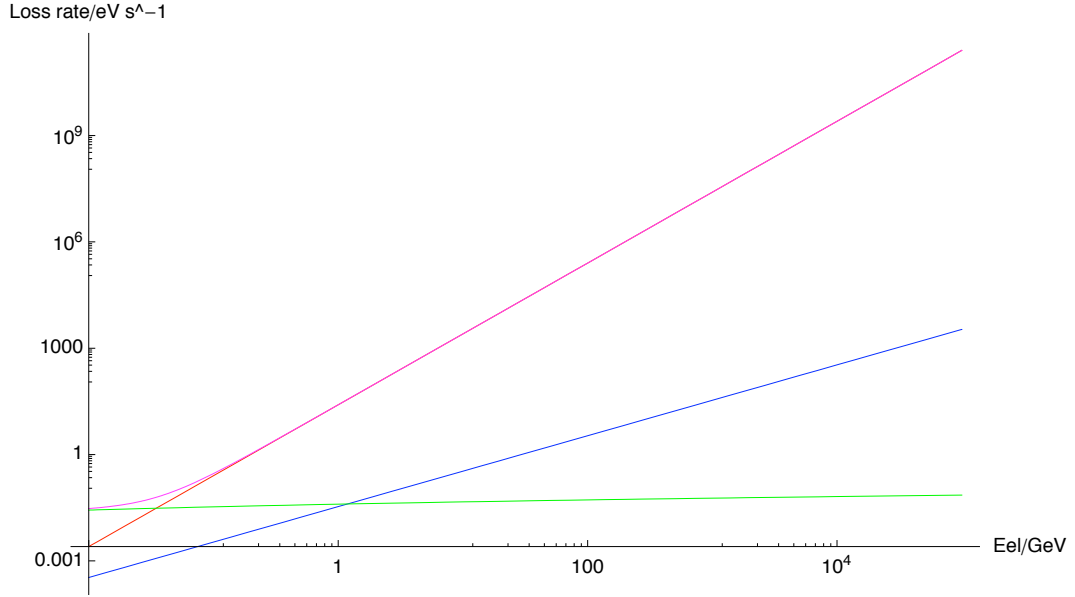


Figure 2.3: Overview of loss processes for high-energy electrons traversing a thin plasma with values appropriate for blazar jets: magnetic field $B = 0.1$ G, number density of hydrogen atoms $N = 10^5$ cm $^{-3}$. The curves correspond to synchrotron / Inverse Compton losses (red), ionisation losses (horizontal blue line) and bremsstrahlung losses (blue). The total loss rate is displayed in purple. As it can clearly be seen, only synchrotron / IC losses are relevant for the the blazar environment. This plot was created using a MATHEMATICA notebook written by Tobias Hein.

Adiabatic Losses occur when the relativistic gas carries out volume work in the expansion and therefore loses internal energy. In the simple case of a uniformly expanding sphere, the energy loss is given by

$$-\left(\frac{dE}{dt}\right)_{adiabatic} = 1.2 \cdot 10^5 \gamma \left(\frac{1}{R^4} \frac{dR}{dt}\right) \text{eV s}^{-1} \text{cm}^{-3} \quad (2.17)$$

Synchrotron and Inverse Compton losses In the Thomson limit of Inverse Compton scattering (see later) and assuming roughly equipartition between the energy densities in the magnetic field and in the synchrotron radiation field, both processes contribute equally to the energy loss of electrons, namely (expressed for synchrotron losses)

$$-\left(\frac{dE}{dt}\right)_{syn} = 6.6 \cdot 10^{-4} \gamma^2 B^2 \text{eV s}^{-1} \text{cm}^{-3} \quad (2.18)$$

2.2.3 Photon losses

Photon losses relevant here are mainly catastrophic losses such as losses due to Compton-upscattering of synchrotron photons. The low energy synchrotron photon is destroyed in that process and a new high-energy electron is produced.

Another important loss mechanism for photons is pair production

$$\gamma\gamma \longrightarrow e^+ e^- \quad (2.19)$$

From the fact that we see sources at TeV energies (i.e. they are transparent to gamma rays) we can derive a lower limit on the Doppler factor (Dondi and Ghisellini 1995) which generally agrees with estimates from spectral modelling ($\delta \approx 10 \dots 50$).

Another photon sink is synchrotron self absorption. This process becomes important at low frequencies as the brightness temperature³ of the source equals the kinetic temperature of the electrons. According to the principle of detailed balance a source cannot emit radiation of brightness temperature greater than its kinetic temperature.

2.2.4 Synchrotron Radiation

Synchrotron Emissivity The total synchrotron power (summed over all polarisations) is given by Ginzburg and Syrovatskii (1965)

$$P_s(\nu, \gamma) = \frac{\sqrt{3} e^2 B_\perp \nu}{m c^2 \nu_c} \int_{\nu/\nu_c}^{\infty} K_{5/3}(\eta) d\eta \quad [\text{erg s}^{-1} \text{ Hz}^{-1}] \quad (2.20)$$

where e is the elementary charge, m the electron rest mass, ν_c the characteristic synchrotron frequency (see below) and $K_{5/3}$ the modified Bessel function of order 5/3.

The synchrotron intensity that a distribution of electrons $n(\gamma)$ produces, is then calculated by convolving the distribution with the synchrotron power:

$$I(\nu) = \int d\gamma P(\nu, \gamma) n(\gamma) \quad (2.21)$$

Monochromatic Approximation A characteristic synchrotron frequency is introduced to quickly estimate the emission of a (power-law) distribution of electrons, see Fig. 2.4. If the spectral shape of the synchrotron emission is governed by the power-law of the electrons (i.e. if it is not too steep) rather than by $P_s(\nu, \gamma)$, the synchrotron emissivity

³A radio astronomers' quantity that refers to the temperature a source would need to have if it attempted to emit the radiation at a certain frequency sustaining a black-body distribution.

can be written as (Felten and Morrison 1966)

$$P_s(\nu, \gamma) \approx P_s(\gamma) \delta(\nu - \nu_c(\gamma)) \equiv P_s(\gamma) (6\nu\nu_0)^{-\frac{1}{2}} \delta(\gamma - \gamma_0) \quad (2.22)$$

where the characteristic frequency ν_c is given by

$$\nu_c = \frac{3e}{4\pi m_e c} B_\perp \gamma^2 = \frac{3}{2} \nu_0 \gamma^2 \quad (2.23)$$

and the total power in synchrotron radiation $P_s(\gamma)$ is

$$P_s(\gamma) = \int_0^\infty d\nu P_s(\nu, \gamma) = \frac{2}{3} r_0^2 c \gamma^2 B_\perp^2 \quad (2.24)$$

with the classical electron radius $r_0 = e^2/mc^2$.

Integrating this ‘monochromatic approximation’ over a power law distribution of electrons with index s , defined by $n(\gamma) \propto \gamma^s$, a power law in photons with index $\alpha = (s + 1)/2$ is obtained, where α is defined as⁴

$$F(\nu) \propto \nu^\alpha \quad (2.25)$$

Melrose Approximation The monochromatic approximation is not good for electron distributions where the electron number density rises too steeply because of mathematical rather than physical effects like the electron distribution that will result from the first-order differential equation Eq. (3.18). In those cases a smoother approximation like the one given by Felten and Morrison (1966) and later by Melrose (1980) is needed to avoid the numerically expensive integration of the modified Bessel function. This approximation is

$$P(\nu, \gamma) = a_s z^{0.3} \exp(-z) \quad (2.26)$$

where $a_s = \sqrt{3} e^2 \Omega / (2\pi c)$ with the electron gyro frequency $\Omega = e B / (mc)$ and the parameter $z = 4\pi\nu / (3\Omega\pi/4\gamma^2)$. Here, the isotropic magnetic field has already been averaged over θ , the angle between the magnetic field direction and the line of sight, to yield the average perpendicular magnetic field for an electron (see right below).

⁴In the literature the spectral index of a power-law is often defined as $\alpha_{lit} = -\alpha$. When following spectral changes during flares, it is more intuitive, however, to define the spectral index positively.

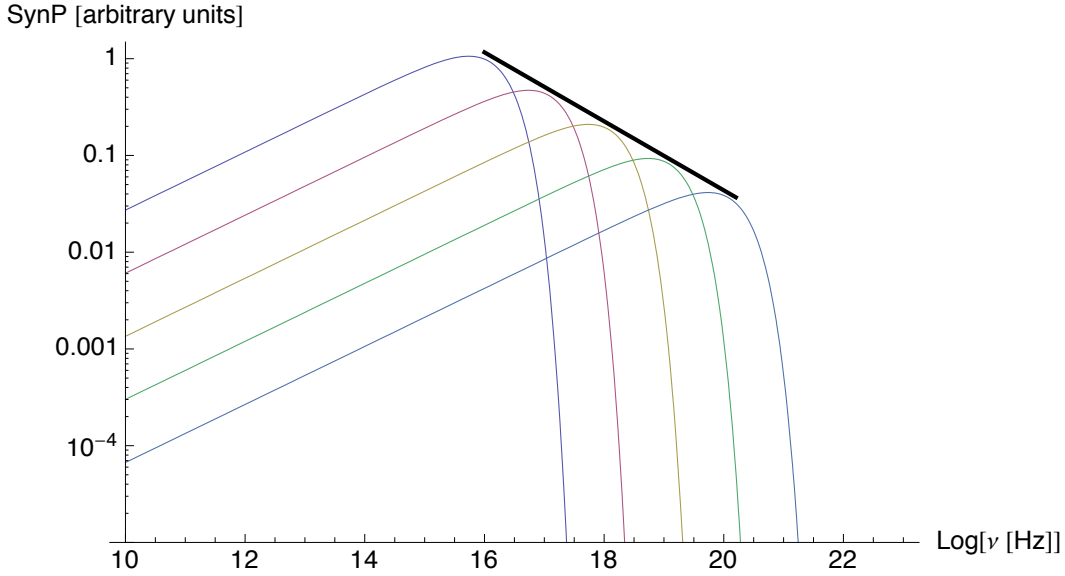


Figure 2.4: *The Synchrotron power as calculated from equation Eq. (2.26) for electrons whose number density follows a power-law in energy. The combination of multiple such synchrotron-emissivities (note the rise $\propto \nu^{0.3}$ and the exponential fall) results in a power-law in the intensity spectrum.*

Isotropic Magnetic field Assuming an isotropic magnetic field \vec{B} with the perpendicular component $B_{\perp} = |\vec{B}| \sin \theta$, the average perpendicular magnetic field \bar{B}_{\perp} that the electrons feel and which is needed for the synchrotron emissivity can easily be calculated from the following integration:

$$\bar{B}_{\perp} = B \overline{\sin \theta} = B \frac{\int \sin \theta \, d\Omega}{\int d\Omega} = B \frac{\pi}{4} \quad (2.27)$$

2.2.5 Inverse Compton Effect

The Inverse Compton (IC) effect occurs when a high-energy electron up-scatters a low energy photon. The cross section for this process depends on the energies of the incoming and outgoing photon and on the energy of the electron before the scattering. Those values determine the so called ‘domain’ of scattering whose limits are the Thomson and Klein-Nishina regimes. Here I will give the relevant formulae for IC scattering following loosely the discussion and closely the notation of Blumenthal and Gould (1970), see table 2.1. For completeness and to increase the physical understanding of the process, the most widely used approximations are also given.

ϵ	Energy of the photon before collision (far observer's frame)
ϵ_1	Energy of the photon after collision (far observer's frame)
γ	Lorentz factor of the electron before collision (far observer's frame)

Table 2.1: *IC notation*

General case – Scattered photon distribution The exact expression for the spectrum of Compton upscattered photons as calculated from quantum electrodynamics (Jauch and Rohrlich 1976) is a rather unwieldy expression (Jones 1968; Coppi and Blandford 1990). However, spectra calculated with the approximate expression given by Jones (1968) and Blumenthal and Gould (1970) are almost indistinguishable from the spectra calculated from the exact expression as long as the electron Lorentz factor $\gamma \gg 1$, which is certainly the case for the radiation that is of interest here. Then, one can write

$$\frac{dN_{\gamma,\epsilon}}{dt d\epsilon_1} = \frac{2\pi r_0^2 m c n(\epsilon) d\epsilon}{\gamma^2 \epsilon} \underbrace{\left[2q \ln q + (1+2q)(1-q) + \frac{1}{2} \frac{(\Gamma_\epsilon q)^2}{1+\Gamma_\epsilon q} (1-q) \right]}_{F(\hat{E}_1, \Gamma_\epsilon)} \quad (2.28)$$

where $E_1 = \epsilon_1(\gamma m c^2)$ is the outgoing photon energy in terms of the electron rest mass, $\Gamma_\epsilon = 4\epsilon\gamma/(m c^2)$ denotes the ‘domain of scattering’ and $q = E_1/[\Gamma_\epsilon(1-E_1)]$ is a parameter. In the Thomson limit $\Gamma_\epsilon \ll 1$ and also $E_1 \ll 1$ and so Eq. (2.28) reduces to the Thomson limit expression Eq. (2.31). Eq. (2.28) is valid for any value of Γ_ϵ , but the assumption $\gamma \gg 1$ has been made in its derivation.⁵

The function $F(\hat{E}_1, \Gamma_\epsilon)$, where the energy of the scattered photon is expressed in terms of its maximum value $\hat{E}_1 = E_1(1+\Gamma_\epsilon)/\Gamma_\epsilon$, is plotted in Fig. 2.5. The transition from the Thomson regime – where the scattered photon distribution is broad and favours the low-energy photons – to the Klein-Nishina regime – where the high-energy end is favoured and a single scattering results in a large energy loss for the scattering electron – can be seen.

It is important to note that only a small region in the parameter space $(\epsilon, \epsilon_1, \gamma)$ contributes to the scattered spectrum. The range of values for E_1 that have to be considered for the spectrum is given by

$$1 \gg \epsilon/(\gamma m c^2) \leq E_1 \leq \Gamma_\epsilon/(1+\Gamma_\epsilon) \quad (2.29)$$

Outside that range there is no IC effect.

⁵The assumption $\gamma \gg 1$ is useful in the derivation because in that case in the electron's frame all photons come from inside a cone with the small half-angle $\theta = 1/\gamma \rightarrow 0$.

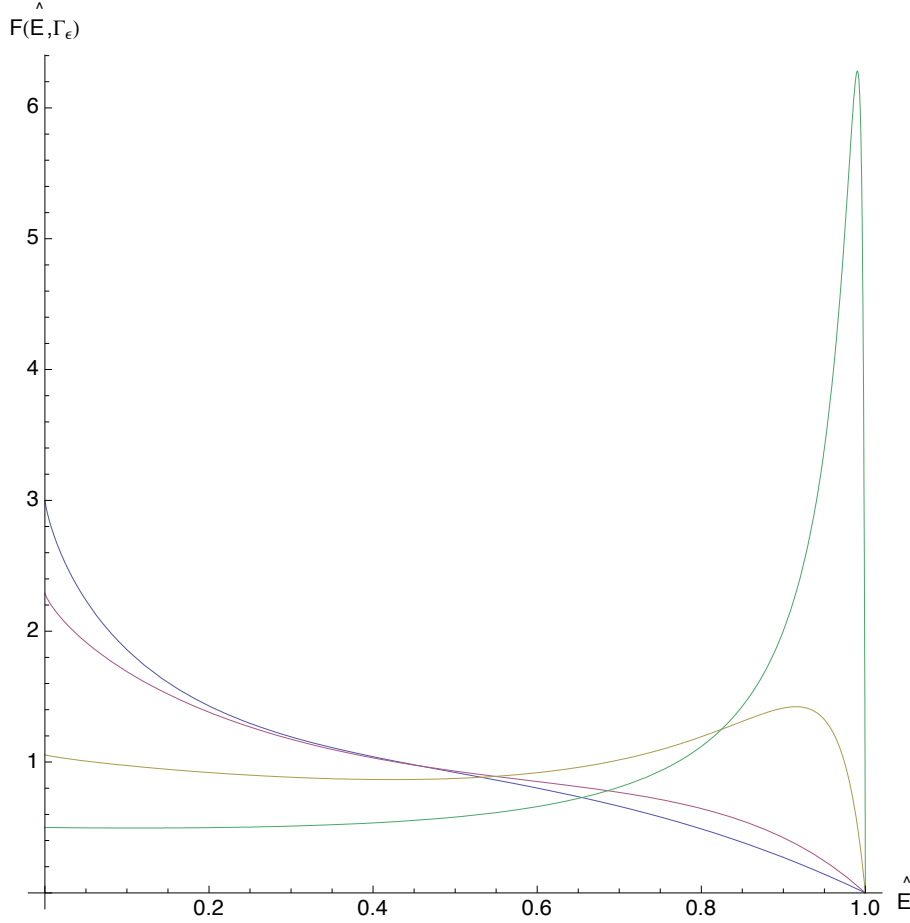


Figure 2.5: The spectrum of Compton scattered photons, $F(\hat{E}_1, \Gamma_\epsilon)$, as calculated from Eq. (2.28) and normalised so that the integral over each curve is 1. The curves correspond to $\Gamma_\epsilon = 0.001$ (blue), 1 (purple), 10 (yellow), 100 (green). The transition from the Thomson to the extreme Klein-Nishina regime can clearly be seen.

General case – Electron energy loss The total energy loss rate for IC scattering in the general case is given by

$$-\frac{dE}{dt} = \int (\epsilon_1 - \epsilon) \frac{dN}{dt d\epsilon_1} d\epsilon_1 \quad (2.30)$$

The exact solution of this integral is a little complicated (Jones 1968; Blumenthal and Gould 1970) but approximate expressions can be given (see below).

Thomson limit In the Thomson limit Eq. (2.28) reduces to (Blumenthal and Gould 1970)

$$\frac{dN_{\gamma,\epsilon}}{dt d\epsilon_1} = \frac{\pi r_0^2 c n(\epsilon) d\epsilon}{2\gamma^4 \epsilon^2} \left(2\epsilon_1 \ln \left[\frac{\epsilon_1}{4\gamma^2 \epsilon} \right] + \epsilon_1 + 4\gamma^2 \epsilon - \frac{\epsilon_1^2}{2\gamma^2 \epsilon} \right) \quad (2.31)$$

The expression vanishes for scattered energies larger than the maximum scattered energy $4\epsilon\gamma^2$.

The expression for electron losses due to IC scattering in the Thomson regime is very similar to the expression for synchrotron losses (Blumenthal and Gould 1970).⁶

$$-\frac{d\gamma}{dt} = \beta_{ic}\gamma^2 \quad (2.32)$$

where

$$\beta_{ic} = \frac{4}{3m_e c} \sigma_T \mathcal{E}_{iso} \quad (2.33)$$

and

$$\mathcal{E}_{iso} = \frac{1}{c} \int d\nu I_\nu \quad (2.34)$$

is the energy of the isotropic radiation field.

Klein-Nishina limit In the extreme Klein-Nishina limit $F(\hat{E}_1, \Gamma_\epsilon)$ from Eq. (2.28) becomes

$$F(\hat{E}_1, \Gamma_\epsilon) = (\ln \Gamma_\epsilon)^{-1} \left[1 + \frac{1}{2} \frac{(\Gamma_\epsilon q)^2}{1 + \Gamma_\epsilon q} (1 - q) \right] \quad (2.35)$$

For the electron losses, an integral expression is introduced as individual losses can alter the energy of the electrons significantly in this limit and therefore make the use of a differential expression inaccurate.

$$-\frac{dE}{dt} = \pi r_0^2 m_e^2 c^5 \int \frac{n(\epsilon)}{\epsilon} \left[\ln \left(\frac{4\epsilon\gamma}{mc^2} \right) - \frac{11}{6} \right] d\epsilon \quad (2.36)$$

Total Compton Spectrum The expressions $\frac{dN_{\gamma,\epsilon}}{dt d\epsilon_1}$ stated above give the spectrum of Compton-scattered photons from the interaction of electrons of energy $\gamma m_e c^2$ with an isotropic density segment $dn = n(\epsilon) d\epsilon$ of photons within energy $d\epsilon$. To calculate the total Compton spectrum, one needs to integrate over all initial photon energies ϵ and over all scattering electron Lorentz factors γ . With the differential number density of electrons $dN_e = N_e(\gamma) d\gamma$, the total Compton spectrum is given by

⁶This is not by chance as both processes can be ascribed to Compton scattering of photons: IC is electrons scattering real photons, while the synchrotron process can be understood as Compton scattering of the virtual photons from the static magnetic field.

$$\frac{dN_{tot}}{dt d\epsilon_1} = \int_{\epsilon} \int_{\gamma} d\gamma N_e(\gamma) \frac{dN_{\gamma,\epsilon}}{dt d\epsilon_1} \quad (2.37)$$

The order of integration is irrelevant.

2.3 Luminosity distance

The luminosity distance is defined as the distance that has to be used for the inverse square law for the observed flux:

$$d_L^2 \equiv \frac{L}{4\pi F} \quad (2.38)$$

In astrophysics, the measurable quantity is usually the redshift z . So one wants a relation between z and d_L :

$$d_L(z) \approx \frac{cz}{H_0} \left[1 + \frac{1}{2}(1 - q_0)z \right] \quad (2.39)$$

where H_0 is the Hubble parameter today ($H_0 = 73.2_{-0.032}^{+0.031} \text{ km s}^{-1} \text{ Mpc}^{-1}$) and $q_0 = \Omega_{m,0}/2 - \Omega_{\Lambda,0}$ is the cosmological deceleration parameter. With WMAP values for the (baryonic and dark) matter and dark energy densities $\Omega_{m,0}$ and $\Omega_{\Lambda,0}$, the deceleration parameter $q_0 = -0.60$ (Spergel et al 2007). More about cosmological distance measurements can be found in any astrophysics textbook (e.g. Carroll and Ostlie 2006).

2.4 Extragalactic Background Light (EBL)

Far away blazars cannot be observed at Very High Energies, though, due to absorption of high-energy gamma rays by pair production with the Extragalactic Background Light (EBL), produced by galaxies throughout the history of the universe and possibly also by first stars. The observed spectra F_{obs} are modified by gamma - gamma pair production

$$F_{obs}(E) = F_{int}(E) \exp[-\tau_{\gamma\gamma}(E, z)] \quad (2.40)$$

where $\tau_{\gamma\gamma}(E, z)$ is the optical depth for this process, effectively producing a ‘gamma-ray horizon’ that depends on the threshold of the gamma-ray telescope used (see Fig. 2.6). This so called ‘Fazio-Stecker relation’ can already become important for nearby extreme blazars (such as Mrk 501) whose IC emission peaks at energies greater than about a TeV. To compare measured SEDs with model SEDs one has to unfold the measured data points

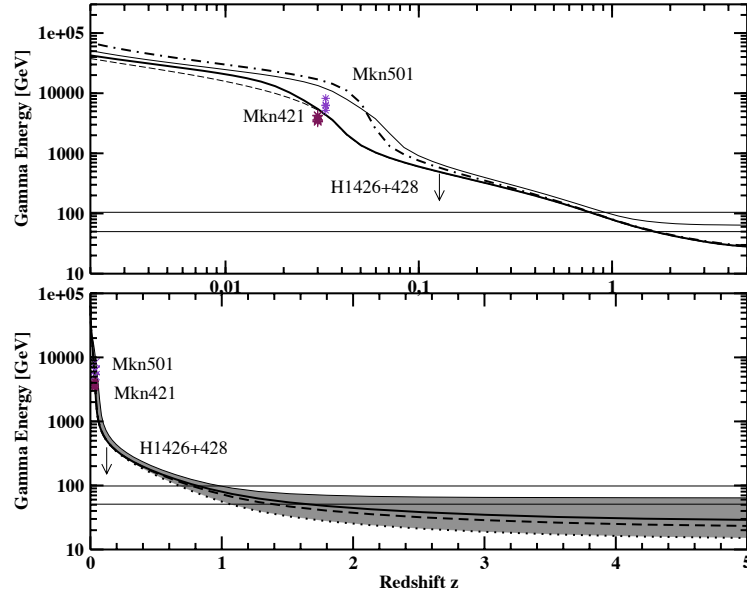


Figure 2.6: Fazio-Stecker relation for different amounts of extragalactic background light (different curves) dividing the Gamma Energy cutoff – Redshift z plane into a region where gamma-rays can reach earth (below the curves) and a region where they are effectively absorbed by intergalactic absorption. Measured cut-offs for three blazars are also shown. The two horizontal curves correspond to 100 and 50 GeV and show that with current gamma-ray telescopes the gamma-ray horizon lies at $z \approx 1$. One can also see that a gamma-ray telescope with a threshold energy of about 10 GeV would be able to observe the very early universe.

using an EBL absorption model like the one described by Kneiske et al (2004). On the other hand, measurements of blazar cut-off energies can give an upper limit on the EBL (Aharonian et al. (H.E.S.S. collaboration) 2006).

2.5 Data fitting

The χ^2 test To test whether a specific set of parameters for a specific model matches a set of data points, the χ^2 test is used, where χ^2 is defined as

$$\chi^2 = \frac{1}{N - dof} \sum_{i=1}^N \left(\frac{\hat{y}_i - y_i}{\sigma_i} \right)^2. \quad (2.41)$$

Here, N is the number of data points and dof are the degrees of freedom, i.e. the number of free parameters used for the plot. The \hat{y}_i are the expected values from the model and the y_i are the observed values (data). σ_i is the (symmetric) Gaussian standard deviation for each data point.

2 Theoretical Background

χ^2 is an expression of how good the fit matches the data scaled to the square-averaged standard deviation of the data points. If the sample is large enough and dof and the σ_i are correct, one would expect $\chi^2 = 1$, much smaller χ^2 s are indicative of either too large σ_i or too few stated degrees of freedom. Values for χ^2 much larger than 1 mean that the model doesn't fit the data points, potentially because the chosen parameters – or the entire model – are wrong.

A χ^2 fit has been used to find the best parameters for Fig. 4.2 on page 47.

3 Analytic Model

In this section I will describe in detail the (semi-)analytic model used by Kirk et al (1998) to explain spectral hysteresis curves in the X-ray band after short sections on the generic form of blazar spectra and a motivation for using a two-zone model instead of a simpler one-zone model. I will also explain why this model cannot be used for an analytic expression of the IC spectrum and show a fit to the synchrotron model.

3.1 Generic Blazar SED

A blazar's spectral energy distribution (SED) generally consists of two broad humps which together cover about 19 orders of magnitude in energy, from $\approx 10^9$ Hz up to $\approx 10^{28}$ Hz. As can be imagined, different energy processes dominate when going from low to high frequencies. At very low frequencies (below about 10^9 Hz, but differing from source to source) the source is self-absorbed (section 2.2.3). This leads to a generic spectral index α (where α is defined as $I_\nu \propto \nu^\alpha$) of $5/2$. In a νI_ν plot the slope of the power-law is of course $\alpha + 1$.

Going further up, we start with the low frequency spectral index that is canonically $\alpha = -0.25$ ($+ 0.75$ in νI_ν) arising from the standard electron acceleration scenario (chapter 2.1.3) where electrons have $s = 2$. In this regime escape losses dominate, as cooling is much slower than escape. At higher energies, synchrotron cooling eventually dominates as synchrotron losses are $\propto \gamma^2$ (and escape losses are at least less energy-dependent). The electron index then gets reduced by one and the photon spectrum steepens to $\alpha = -0.75$ ($+ 0.25$ in νI_ν). At some point the maximum electron Lorentz factor γ_{max} is reached, as losses ($\propto -\gamma^2$) balance gains ($\propto \gamma$) and the spectrum falls off steeply after that.

Generally the shape of the spectrum is reproduced in the high-energy range but taking into account the distribution of scattered photons according to the Klein-Nishina cross section (see Fig. 2.5), the features of the synchrotron branch (see below) get washed out. As the IC peak results roughly from multiplying the synchrotron spectrum with γ_{max}^a with $a > 1$ (and dependent on the scattering regime), it is also broader than the synchrotron peak.

3.2 Homogeneous two zone model

Most current homogeneous SSC models for blazar jets (e.g. Tavecchio et al 1998; Krawczynski et al 2004) use only one zone, but sometimes several electron populations (Krawczynski et al 2004) to account for the blob and jet emission. In those ad-hoc-models a power-law of particles is injected in just the way needed to produce the observed spectrum. If available, the optical - X-ray data are used to find the break energy where the spectral index changes. The spectral indices before and after the break do not result from physical modelling here but are free fit parameters. By varying Doppler factor, magnetic field and source region, the IC peak is then fitted which normally is much easier as the error bars are quite large there. It is obvious that those models produce ‘better’ fits in terms of smaller values of χ^2 . . . But do they also *explain* the observations?

During a flare most times a ‘soft lag’ (i.e. the spectral index hardens / flattens first and softens / steepens later) is observed (e.g. Gear et al 1986; Takahashi et al 1996). This behaviour could already be explained by the above-mentioned one zone models: It arises whenever the cooling mechanism is more efficient at higher energies and a flare is produced by enhancing the injected power-law distribution by an energy-independent factor. Then, of course, more radiation is first produced at high energies, flattening the spectrum and thus leading to the desired behaviour.

But in some sources the spectral index softens *first* and hardens later (e.g. Sembay et al 1993) which cannot be explained in those one zone models.

To overcome this difficulty, Kirk et al (1998) used a time-dependent model that was originally applied to the expansion of supernova shock waves (Ball and Kirk 1992) and that splits the source region into two spatially separated zones: an acceleration and a radiation zone. In the former, thought to be around the shock, particles are accelerated from some initial value of the electron Lorentz factor γ_0 up to γ_{max} and then escape after an energy-independent time t_{esc} into the radiation zone which lies downstream. A finite extent of the radiation zone is used to get a very hard low frequency spectral index and a break at a characteristic energy where the cooling time equals the escape time. See Fig. 3.3 on page 36 for a sketch of the model geometry.

3.3 Acceleration zone

3.3.1 Kinetic Equation

If the electrons suffer continuous losses (as in synchrotron cooling and in the Thomson regime of IC scattering), one can formulate the total rate of energy loss for an electron as $\dot{\gamma}(\gamma)$ where $-\dot{\gamma}/\gamma \ll N_s c \sigma$ with $\gamma = \left(\sqrt{1 - \beta^2}\right)^{-1}$, $\beta = v/c$, N_s the number density of particles scattering off the electron and σ is the total cross-section for the process. In other words, the electron must not lose a significant amount of energy per collision for this approximation to be good.

Using the reasoning presented in e.g. Blumenthal and Gould (1970); Longair (1994), one can then write a differential equation for the evolution of the number of electrons $N(\gamma, t) d\gamma$ within the interval $[\gamma, \gamma + d\gamma]$ at time t since $N(\gamma, t) \dot{\gamma}(\gamma)$ is the flux of electrons entering this interval $d\gamma$ and $N(\gamma + d\gamma, t) \dot{\gamma}(\gamma + d\gamma)$ is the flux leaving it. If $d\gamma > 0$ the electrons gain energy. One then arrives at the differential equation by equating the net flux entering the interval to the increase of electrons within $d\gamma$;

$$\frac{\partial}{\partial t} N(\gamma, t) d\gamma = N(\gamma, t) \dot{\gamma}(\gamma) - N(\gamma + d\gamma, t) \dot{\gamma}(\gamma + d\gamma) + \sum_i Q_i(\gamma, t) dE \quad (3.1)$$

where $Q_i(\gamma, t)$ stands for sources and sinks of electrons. A possible source would arise in the rest frame of the blob simply from the fact that the blob picks up electrons while moving through space. A possible sink would be electrons that ‘escape’ from the region, cf. the section about Fermi acceleration (2.1.3). One then arrives at the continuity equation for electrons in energy space¹

$$\frac{\partial N(\gamma, t)}{\partial t} + \frac{\partial}{\partial \gamma} (\dot{\gamma} N(\gamma, t)) = \sum_i Q_i \quad (3.2)$$

The general solution for this equation has been given by Ginzburg and Syrovatskii (1964) and several applications have been discussed by Kardashev (1962). Specific solutions for this equation will be discussed in sections (3.3.2) and (3.4.1).

In the model of Kirk et al (1998), two instances of this equation are used for the two different zones. In the acceleration zone, the electrons gain energy by stochastic acceleration and suffer synchrotron losses:

$$\dot{\gamma} = \frac{\gamma}{t_{acc}} - \beta_s \gamma^2 \quad (3.3)$$

¹I.e. the diffusion-loss equation without diffusion

3 Analytic Model

where t_{acc} is the characteristic time for shock acceleration gains. See section 2.1.3 for a motivation of this energy-independent acceleration time scale.

$$\beta_s = \frac{4 \sigma_T B^2}{3 mc 8\pi} \quad (3.4)$$

describes the synchrotron losses with the electron rest mass m and the isotropic magnetic field B .

To account for the losses that occur when particles leave the acceleration region, the simple ‘leaky box’ term is used where catastrophic losses are described by the characteristic (energy independent) time t_{esc} it takes for a particle to ‘escape’ from the acceleration region.

$$Q_{\text{escape}} = -\frac{N}{t_{esc}} \quad (3.5)$$

Other losses such as synchrotron self-absorption (SSA) are not included. SSA in particular is not included because this model tries to explain radiation processes at or near the peak frequency of the spectrum where SSA is irrelevant. Besides, the SSA cut-off so far is not measurable.²

We further need to include a source term that describes the injection of low energy electrons of energy γ into the acceleration process:

$$Q_{\text{injection}} = Q_0 \Theta(\gamma_1(t) - \gamma) \delta(\gamma - \gamma_0) = Q(\gamma, t) \delta(\gamma - \gamma_0) [\text{cm}^{-2}\text{s}^{-1}] \quad (3.6)$$

Summing up all energy gain and loss terms and all source terms, one then gets the kinetic equation that governs the number density³ $N(\gamma, t)d\gamma$ of particles in the acceleration zone.

$$\frac{\partial N(\gamma, t)}{\partial t} + \frac{\partial}{\partial \gamma} \left[\left(\frac{\gamma}{t_{acc}} - \beta_s \gamma^2 \right) N(\gamma, t) \right] + \frac{N(\gamma, t)}{t_{esc}} = Q_0 \delta(\gamma - \gamma_0) \Theta(\gamma_1(t) - \gamma) \quad (3.7)$$

3.3.2 Solution

To solve this linear inhomogeneous first order partial differential equation (PDE) the method of characteristics is employed. This method is described in more detail in section 3.4.1 for the radiation zone equation as the latter is more compact and the method is

²This might change in the near future by observing the SSA cut-off in the submillimetre to FIR range with satellites like Planck and ground-based telescopes like APEX (Rachen and Enßlin 2007)

³The number density has units cm^{-2} here because the acceleration zone is thought to be infinitely thin (like a plane) in the model.

more obvious there. For a strictly mathematical treatment see Meyberg and Vachenaer (2003).

The ‘kernel’ of the PDE is

$$\frac{\partial \gamma}{\partial t} = \frac{\gamma}{t_{acc}} - \beta_s \gamma^2 \quad (3.8)$$

Integrating the kernel from $t_0 = 0$ to t and from ξ to γ and solving for $\xi(\gamma, t)$ and $\gamma(\xi, \hat{t})$ respectively we get the transformation rules for $(\gamma, t) \leftrightarrow (\xi, \hat{t})$, where $t = \hat{t}$:

$$\xi(\gamma, t) = \left(t_{acc} \beta + \frac{e^{\frac{t}{t_{acc}}} (1 - t_{acc} \beta \gamma)}{\gamma} \right)^{-1} \quad (3.9)$$

$$\gamma(\xi, \hat{t}) = \frac{e^{\frac{\hat{t}}{t_{acc}}} \xi}{1 + \left(e^{\frac{\hat{t}}{t_{acc}}} - 1 \right) t_{acc} \beta \xi} \quad (3.10)$$

As desired, the PDE in $N(\gamma, t)$ reduces to an ordinary differential equation (ODE) in $\tilde{N}(\xi, \hat{t})$ that is easy to solve:

$$\frac{\partial \tilde{N}(\xi, \hat{t})}{\partial \hat{t}} + \left(\frac{1}{t_{acc}} + \frac{1}{t_{esc}} - 2\beta_s \gamma(\xi, \hat{t}) \right) \tilde{N}(\xi, \hat{t}) = Q_0 \Theta(\gamma_1(t) - \gamma) \delta(\gamma(\xi, \hat{t}) - \gamma_0) \quad (3.11)$$

The homogeneous solution is

$$\tilde{N}(\xi, \hat{t}) = \tilde{N}_0 \exp \left[- \int_0^{\hat{t}} d\hat{t}' \left(\frac{1}{t_{acc}} + \frac{1}{t_{esc}} - 2\beta_s \gamma(\xi, \hat{t}') \right) \right] \quad (3.12)$$

Varying the constant $\tilde{N}_0 \rightarrow \tilde{N}_0(\xi, \hat{t})$ one arrives at

$$\tilde{N}_0(\xi, \hat{t}) = \int_0^{\hat{t}} d\hat{t}' \exp \left[\int_0^{\hat{t}'} d\hat{t}'' \left(\frac{1}{t_{acc}} + \frac{1}{t_{esc}} - 2\beta_s \gamma(\xi, \hat{t}'') \right) \right] Q_0 \Theta(\gamma_1(\hat{t}') - \gamma) \delta(\gamma(\xi, \hat{t}') - \gamma_0) \quad (3.13)$$

Now, using the definition of the δ -function (Bronstein et al 2001)

$$\delta(g(x)) = \sum_{i=1}^n \frac{1}{|g'(x_i)|} \delta(x - x_i) \quad (3.14)$$

with $g(x_i) = 0$ and $g'(x_i) \neq 0$, ($i = 1, 2, \dots, n$),

we can transform

$$\delta(\gamma(\xi, \hat{t}) - \gamma_0) \equiv \left| \left[\frac{\partial \gamma(\xi, \hat{t})}{\partial \hat{t}} \right]_{t_0}^{-1} \right| \delta(\hat{t} - \hat{t}_0) \equiv \frac{t_{acc}}{\gamma_0(1 - t_{acc}\beta\gamma_0)} \delta(\hat{t} - \hat{t}_0) \quad (3.15)$$

where

$$t_0 = t_{acc} \ln \left[\frac{\gamma_0(t_{acc}\beta\xi - 1)}{\xi(t_{acc}\beta\gamma_0 - 1)} \right]. \quad (3.16)$$

So the solution in (ξ, \hat{t}) is

$$\begin{aligned} \tilde{N}(\xi, \hat{t}) = & \Theta(\hat{t} - \hat{t}_0) Q_0 \Theta(\gamma_1(\hat{t}) - \gamma) \frac{t_{acc}}{t_{acc}\beta\gamma_0^2 - \gamma_0} \\ & \exp \left[\int_0^{\hat{t}_0} d\hat{t}' \left(\frac{1}{t_{acc}} + \frac{1}{t_{esc}} - 2\beta_s \gamma(\xi, \hat{t}') \right) \right] \\ & \exp \left[- \int_0^{\hat{t}} d\hat{t}' \left(\frac{1}{t_{acc}} + \frac{1}{t_{esc}} - 2\beta_s \gamma(\xi, \hat{t}') \right) \right] \end{aligned} \quad (3.17)$$

where the first Θ -function comes from the integration over the δ -function.

Evaluating the integrals and transforming back to (γ, t) , one finally arrives at

$$N(\gamma, t) = a \frac{1}{\gamma^2} \left(\frac{1}{\gamma} - \frac{1}{\gamma_{max}} \right)^{\frac{t_{acc} - t_{esc}}{t_{esc}}} \Theta(\gamma - \gamma_0) \Theta(\gamma_1(t) - \gamma) \quad (3.18)$$

for $\gamma_0 < \gamma < \gamma_1(t)$, $N(\gamma, t) = 0$ otherwise. $\Theta(x)$ is the Heaviside step function

$$\Theta(x - x_0) = \begin{cases} 0 & \text{for } x \leq x_0 \\ 1 & \text{for } x > x_0 \end{cases} \quad (3.19)$$

and $\Theta(\hat{t} - \hat{t}_0) \equiv \Theta(\gamma - \gamma_0)$, see (3.15). The following abbreviations from Kirk et al (1998) have been used:

$$a = Q_0 t_{acc} \gamma_0^{\frac{t_{acc}}{t_{esc}}} \left(1 - \frac{\gamma_0}{\gamma_{max}} \right)^{-\frac{t_{acc}}{t_{esc}}} [\text{cm}^{-2}] \quad (3.20)$$

$$\gamma_1(t) = \left(\frac{1}{\gamma_{max}} + \left[\frac{1}{\gamma_0} - \frac{1}{\gamma_{max}} \right] e^{-\frac{t_{acc}}{t_{esc}}} \right)^{-1} \quad (3.21)$$

with $\gamma_{max} = (\beta_s t_{acc})^{-1}$. The solution is identical to equation (3) in Kirk et al (1998) but note that they omitted the definition of $Q = Q_0 \Theta(\gamma_1(t) - \gamma)$.

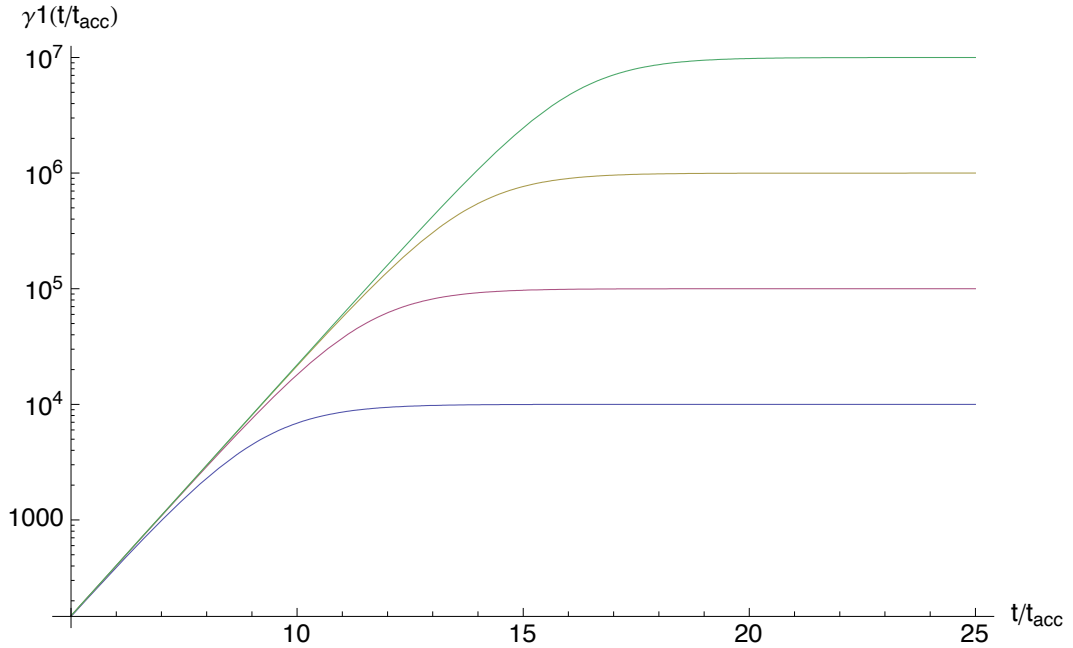


Figure 3.1: $\gamma_1(t/t_{acc})$ as a function of t/t_{acc} for $\gamma_{max} = 1 \cdot 10^4$ (blue), $1 \cdot 10^5$ (purple), $1 \cdot 10^6$ (yellow) and $1 \cdot 10^7$ (green). γ_{max} is reached after ca. 11, 13, 15, 17 acceleration times respectively.

As one can see from the solution, Eq. (3.18), the particle density in the acceleration zone rises steeply for $t_{esc}/t_{acc} > 1$ near γ_{max} and would diverge if it were not cut off abruptly by the second Θ function (Kardashev 1962). Although t_{esc}/t_{acc} needs to be set to 2 (> 1) to get the hard low frequency spectral index of 0.25 in the context of Fermi acceleration (see section 2.1.3), this does not make the use of such an equation unphysical since it is still possible to integrate the distribution. But one has to take care when computing the synchrotron and IC emissivities from such a distribution: The monochromatic (Delta) approximation is not applicable here.

Other than that, the equation represents a simple power-law in energy with a fixed low energy cut-off at γ_0 and a time-dependent high-energy cut-off at $\gamma_1(t)$. $\gamma_1(t) \rightarrow \gamma_{max}$ for large times, see Fig. 3.1 for a plot of the time evolution of $\gamma_1(t)$. The power-law solution Eq. (3.18) is plotted together with the electron density in the radiation zone (see below) in Fig. 3.2.

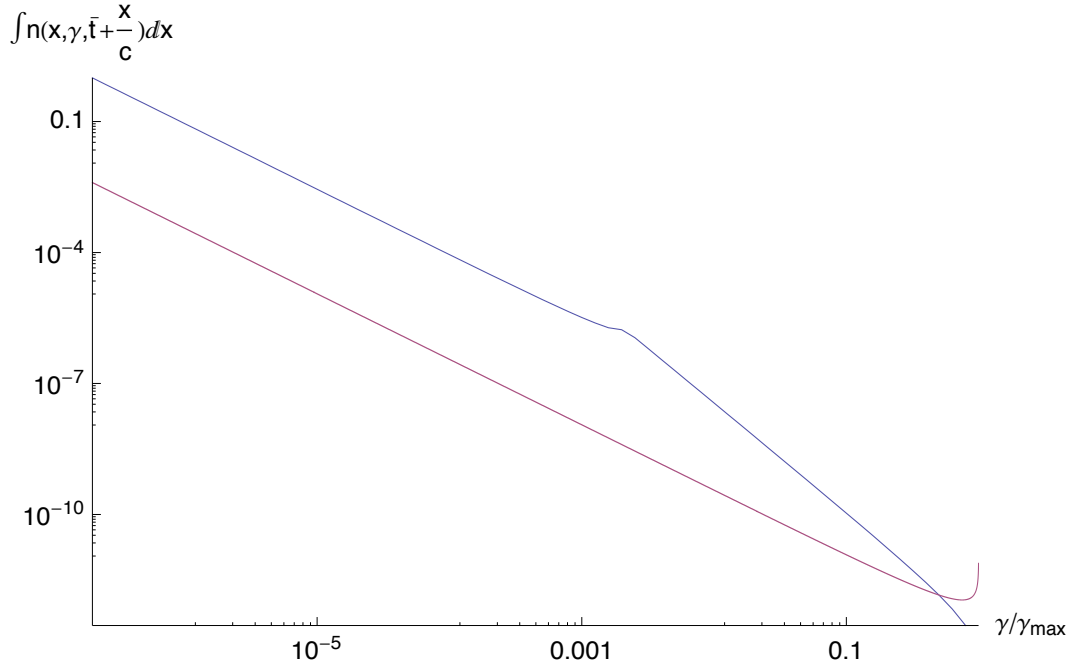


Figure 3.2: The integrated electron density (normalised) in the acceleration zone (red) and in the radiation zone (blue) for large times. The steep increase of the electron number in the acceleration zone near γ_{max} occurs in this model when $t_{esc}/t_{acc} > 1$ (Kardashev 1962). Other parameters as in Fig. 3.4.

3.4 Radiation Zone

3.4.1 Kinetic Equation

The differential electron density $dn(x, \gamma, t)$ [cm^{-3}] for particles in the radiation zone in the range $dx, d\gamma$ at time t obeys the following kinetic equation (see section 3.3)

$$\frac{\partial n(\gamma, t)}{\partial t} - \frac{\partial}{\partial \gamma} (\beta_s \gamma^2 n(\gamma, t)) = \frac{N(\gamma, t)}{t_{esc}} \cdot \delta(x - x_s(t)) \quad (3.22)$$

The term $-\beta_s \gamma^2$ again describes synchrotron losses, the acceleration term of Eq. (3.7) is not included here because particles only get accelerated in the shock zone in this model. The source function is equivalent to the rate of electrons that escape from the acceleration zone, i.e. $\frac{N(\gamma, t)}{t_{esc}}$. They enter the radiation zone at the shock, i.e. at $x = x_s(t)$.

Solution

Again, the method of characteristics is used to solve this PDE. It is described in more detail here.

The kernel of the PDE (3.22) is

$$\frac{\partial \gamma}{\partial t} = -\beta_s \gamma^2 \quad (3.23)$$

To find the characteristic equation of the PDE, the kernel has to be integrated:

$$\left[-\frac{1}{\gamma'} \right]_{\xi}^{\gamma} = \frac{1}{\xi} - \frac{1}{\gamma} = -\beta_s (t - t_0) \quad (3.24)$$

t_0 will be set to 0 in the following. The integration over γ can be thought as looking for the value of the Lorentz factor ξ an electron had to have at time t_0 to have γ at time t .

The integrated kernel gives the transformation rules for $(\gamma, t) \rightarrow (\xi, \hat{t})$:

$$\xi(\gamma, t) = \left(-\beta_s t + \frac{1}{\gamma} \right)^{-1} \quad (3.25)$$

$$\hat{t} = t \quad (3.26)$$

and for $(\xi, \hat{t}) \rightarrow (\gamma, t)$:

$$\gamma(\xi, \hat{t}) = \left(\beta_s \hat{t} + \frac{1}{\xi} \right)^{-1} \quad (3.27)$$

$$t = \hat{t} \quad (3.28)$$

To substitute the transformation into the PDE, one needs to evaluate the transformation rules for the derivatives:

$$\left(\frac{\partial \tilde{n}(\xi, \hat{t})}{\partial t} \right)_{\gamma} = \left(\frac{\partial \tilde{n}(\xi, \hat{t})}{\partial \xi} \right)_{\gamma} \frac{\partial \xi}{\partial t} + \left(\frac{\partial \tilde{n}(\xi, \hat{t})}{\partial \hat{t}} \right)_{\gamma} \underbrace{\frac{\partial \hat{t}}{\partial t}}_{=1} \quad (3.29)$$

$$\left(\frac{\partial \tilde{n}(\xi, \hat{t})}{\partial \gamma} \right)_{\hat{t}} = \left(\frac{\partial \tilde{n}(\xi, \hat{t})}{\partial \xi} \right)_{\hat{t}} \frac{\partial \xi}{\partial \gamma} + \left(\frac{\partial \tilde{n}(\xi, \hat{t})}{\partial \hat{t}} \right)_{\hat{t}} \underbrace{\frac{\partial \hat{t}}{\partial \gamma}}_{=0} \quad (3.30)$$

$\partial \hat{t} / \partial \gamma$ vanishes as $\hat{t} = t$ and therefore $\partial \hat{t} = \partial t = 0$ as we are evaluating the partial derivative with t fixed.

In going from $n(\gamma, t) \rightarrow \tilde{n}(\xi, \hat{t})$ we now have

$$\frac{\partial \tilde{n}(\xi, \hat{t})}{\partial \hat{t}} + \left(\frac{\partial \tilde{n}(\xi, \hat{t})}{\partial \xi} \frac{\partial \xi}{\partial t} \right) - 2\beta_s \gamma(\xi, \hat{t}) \tilde{n}(\xi, \hat{t}) - \beta_s \gamma^2 \left(\frac{\partial \tilde{n}(\xi, \hat{t})}{\partial \xi} \frac{\partial \xi}{\partial \gamma} \right) = \frac{N(\gamma(\xi, \hat{t}), \hat{t})}{t_{esc}} \delta(x - x_s(\hat{t})) \quad (3.31)$$

3 Analytic Model

with

$$\frac{\partial \xi}{\partial \gamma} = \frac{-1/\gamma^2}{(-\beta t + 1/\gamma)^2} \quad (3.32)$$

and

$$\frac{\partial \xi}{\partial t} = \frac{-\beta_s}{(-\beta_s t + 1/\gamma)^2}. \quad (3.33)$$

Substituting in Eq. (3.31), the PDE reduces to

$$\frac{\partial \tilde{n}(\xi, \hat{t})}{\partial \hat{t}} - 2\beta_s \gamma(\xi, \hat{t}) \tilde{n}(\xi, \hat{t}) = \frac{N(\gamma(\xi, \hat{t}), \hat{t})}{t_{esc}} \delta(x - x_s(\hat{t})) \quad (3.34)$$

which is the ODE we wanted to arrive at.

The homogeneous solution is

$$\tilde{n}(\xi, \hat{t}) = \tilde{n}_0 \exp \left[\int_0^{\hat{t}} d\hat{t}' 2\beta_s \gamma(\xi, \hat{t}') \right]. \quad (3.35)$$

Varying the constant $\tilde{n}_0 \rightarrow \tilde{n}_0(\xi, \hat{t})$, we get

$$\tilde{n}_0 = \int_0^{\hat{t}} d\hat{t}' \frac{N(\gamma(\xi, \hat{t}'), \hat{t}')}{t_{esc}} \delta(x - x_s(\hat{t}')) e^{\int_0^{\hat{t}'} 2\beta_s \gamma(\xi, \hat{t}'') d\hat{t}''}. \quad (3.36)$$

To evaluate the integration over t , the Delta function needs to be rewritten with $x_s = tu_s$ using the definition (3.14):

$$\delta(x - x_s(t)) \longrightarrow \frac{1}{u_s} \delta \left(t - \frac{x}{u_s} \right) \quad (3.37)$$

Substituting in $\hat{n}(\xi, \hat{t})$ and integrating over the Delta function

$$\tilde{n}(\xi, \hat{t}) = e^{\int_0^{\hat{t}} d\hat{t}' 2\beta_s \gamma(\xi, \hat{t}')} \left[\frac{N(\gamma(\xi, \frac{x}{u_s}), \frac{x}{u_s})}{t_{esc} u_s} \Theta \left(\hat{t}' - \frac{x}{u_s} \right) e^{\int_0^{\frac{x}{u_s}} 2\beta_s \gamma(\xi, \hat{t}'') d\hat{t}''} \right] \quad (3.38)$$

With the definition of the Heaviside function (3.19). The Θ function comes again from the integration over the δ -function.

Evaluating

$$\int_0^{\hat{t}} \gamma(\xi, \hat{t}') d\hat{t}' = \int_0^{\hat{t}} d\hat{t}' \left(\beta_s \hat{t}' + \frac{1}{\xi} \right)^{-1} = \frac{\ln(1 + \beta_s \hat{t} \xi)}{\beta_s} \quad (3.39)$$

and substituting in (3.38) with (3.18) we have the solution for $\hat{n}(\xi, \hat{t})$:

$$\begin{aligned} \tilde{n}(\xi, \hat{t}) = & \frac{a}{u_s t_{esc}} \frac{(1 + \beta \hat{t} \xi)^2}{\left(1 + \beta \frac{x}{u_s} \xi\right)^2} \left(\frac{1}{\xi} + \beta \frac{x}{u_s}\right)^2 \left[\left(\beta_s \frac{x}{u_s} + \frac{1}{\xi}\right) - \frac{1}{\gamma_{max}} \right]^{\frac{t_{acc} - t_{esc}}{t_{esc}}} \\ & \Theta \left(\left(\frac{1}{\xi} + \beta_s \frac{x}{u_s}\right)^{-1} - \gamma_0 \right) \Theta \left(\gamma_1 \frac{x}{u_s} - \left(\frac{1}{\xi} + \beta_s \frac{x}{u_s}\right)^{-1} \right) \Theta \left(t - \frac{x}{u_s} \right) \end{aligned} \quad (3.40)$$

Simplifying and transforming back to (γ, t) we arrive at the solution for $n(\gamma, t)$, valid for all $\gamma > \gamma_0$:

$$\begin{aligned} n(\gamma, t) = & \frac{a}{u_s t_{esc}} \frac{1}{\gamma^2} \left[\frac{1}{\gamma} - \beta_s \left(t - \frac{x}{u_s} \right) - \frac{1}{\gamma_{max}} \right]^{\frac{t_{acc} - t_{esc}}{t_{esc}}} \\ & \underbrace{\Theta(\gamma - \gamma_0)}_{=1} \Theta \left[\gamma_1 \left(\frac{x}{u_s} \right) - \left(\frac{1}{\gamma} - \beta_s t + \beta_s \frac{x}{u_s} \right)^{-1} \right] \Theta \left(t - \frac{x}{u_s} \right) \end{aligned} \quad (3.41)$$

The solution to the PDE (3.22) has also been given in equation (7) of Kirk et al (1998) but they omitted the last Θ function.

Integration over x

As we are not interested in the dependence on position of the synchrotron spectrum,⁴ we integrate the electron distribution over the emitting region. We note that the specific intensity at a position $x = X (> u_s t)$ on the symmetry axis of the jet at a time t depends on the retarded time $\bar{t} = t - \frac{X}{c}$.

$$\int_{x_0}^{x_1} dx n \left(x, \gamma, \bar{t} + \frac{x}{c} \right) = \frac{a}{\left(1 - \frac{u_s}{c}\right) \gamma_{max}^{\frac{t_{acc} + t_{esc}}{t_{esc}}}} \cdot \left(\frac{\gamma_{max}}{\gamma} \right)^2 \left[\left(\frac{\gamma_{max}}{\gamma} - \frac{\bar{t}}{t_{acc}} + \frac{x \left(1 - \frac{u_s}{c}\right)}{u_s t_{acc}} - 1 \right)^{\frac{t_{acc}}{t_{esc}}} \right]_{x_0(\gamma, \bar{t})}^{x_1(\bar{t})} \quad (3.42)$$

where the limits of the integration are given by the Θ -functions in Eq. (3.41) and are illustrated in Fig. 3.3.

The upper boundary is given by the retarded position of the shock front

⁴Otherwise we would have had to properly treat the diffusion-loss equation in the first place and not just approximate it by a delta-shaped shock and an energy-independent escape time.

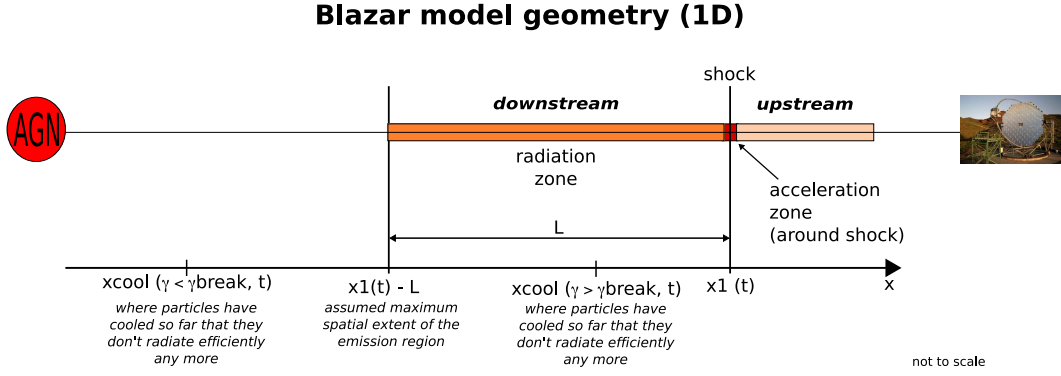


Figure 3.3: Blazar model geometry in the shock reference frame where the shock is at rest. Plasma flows towards the shock from upstream. Particles (electrons, positrons) thereby undergo diffusive shock acceleration and escape into the downstream region where they radiate. The limits for the spatial integration are given either by the assumed extent of the emitting region or by $x_{cool}(\gamma, \bar{t})$, the position where particles have cooled so far that their emission is negligible.

$$x_1(\bar{t}) = \frac{u_s \bar{t}}{1 - \frac{u_s}{c}} \quad (3.43)$$

The lower boundary is either given by the assumed maximum extent of the emitting region at $x_1(\bar{t}) - L$ or by $x_{cool}(\gamma, \bar{t})$, the point furthest from the shock at which particles have enough energy (Lorentz factor γ) to cool (radiate) efficiently at time $\bar{t} + \frac{x_0}{c}$ which is the physical reason for the appearance of the second Θ -function in Eq. (3.41). So the lower boundary is given by

$$x_0(\gamma, \bar{t}) = \mathbf{Max}[x_{cool}(\gamma, \bar{t}), x_1(\bar{t}) - L] \quad (3.44)$$

It is useful to express L in terms of the retarded time t_b (b for *break* as this time determines the break in the electron distribution) the plasma needs to cross the emitting region (measured in the plasma rest frame)

$$t_b = \frac{(1 - u_s/c)L}{u_s} \quad (3.45)$$

and x_{cool} can only be derived numerically from the transcendental equation one gets when substituting Eq. (3.21) into the second Θ -function of Eq. (3.41):

$$\left[\frac{\gamma_{max}}{\gamma} - \frac{\bar{t} + \frac{x_{cool}}{c}}{t_{acc}} + \frac{x_{cool}}{u_s t_{acc}} \right] = 1 + \left(\frac{\gamma_{max}}{\gamma_0} - 1 \right) \exp \left[-\frac{x_{cool}}{u_s t_{acc}} \right] \quad (3.46)$$

Note that Eq. (3.41) vanishes before the 'switch-on' time

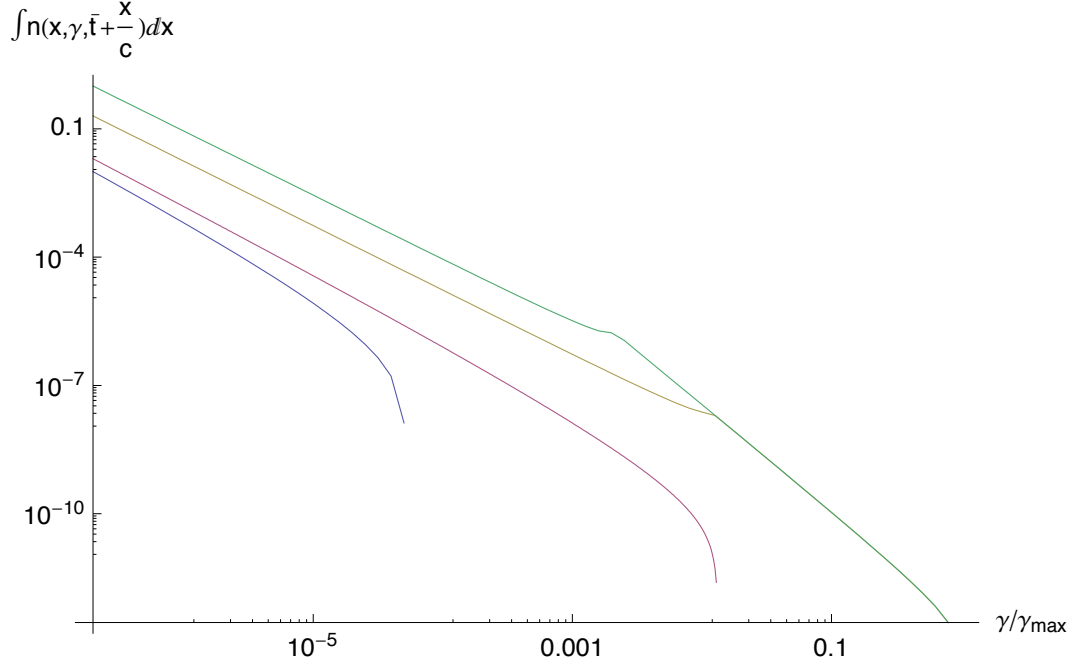


Figure 3.4: Time evolution of the integrated electron density (normalised) in the radiation zone as given by equation Eq. (3.42). The curves correspond to $5 t_{acc}$ (blue line), $10 t_{acc}$ (purple), $100 t_{acc}$ (yellow) and $500 t_{acc}$ (green). At later times the distribution does not change significantly for a shock speed $u_s = 0$ (as chosen for this plot), for $u_s > 0$ the break (see text) moves very slowly to lower energies until a power law with constant index is reached (at $\bar{t} \approx 10^8 t_{acc}$ for $u_s = 0.1 c$). Further parameters for this plot are $t_{esc} = 2 t_{acc}$, $t_b = 100 t_{esc}$.

$$\bar{t} > \bar{t}_{on} = t_{acc} \left(1 - \frac{u_s}{c} \right) \ln \left[\frac{\gamma_{max}/\gamma_0 - 1}{\gamma_{max}/\gamma - 1} \right] \quad (3.47)$$

This is the time it takes for particles of γ_0 to accelerate to γ and γ_{max} appears because all γ s are expressed in terms of γ_{max} .

The break in the distribution function appears only at times where electrons have had time to escape and then divides the region where escaping occurs faster than cooling (left, lower energies) from the region where the electrons cool so rapidly that they lose all their energy in the radiation zone before they have time to escape. The time-dependent integrated particle density in the radiation zone is plotted in Fig. 3.4.

3.4.2 Analytic Approximation for x_{cool} ?

x_{cool} can only be computed numerically since it is given as the solution of the transcendental equation Eq. (3.46), see Fig. 3.5 for a plot of x_{cool} vs. electron Lorentz factor

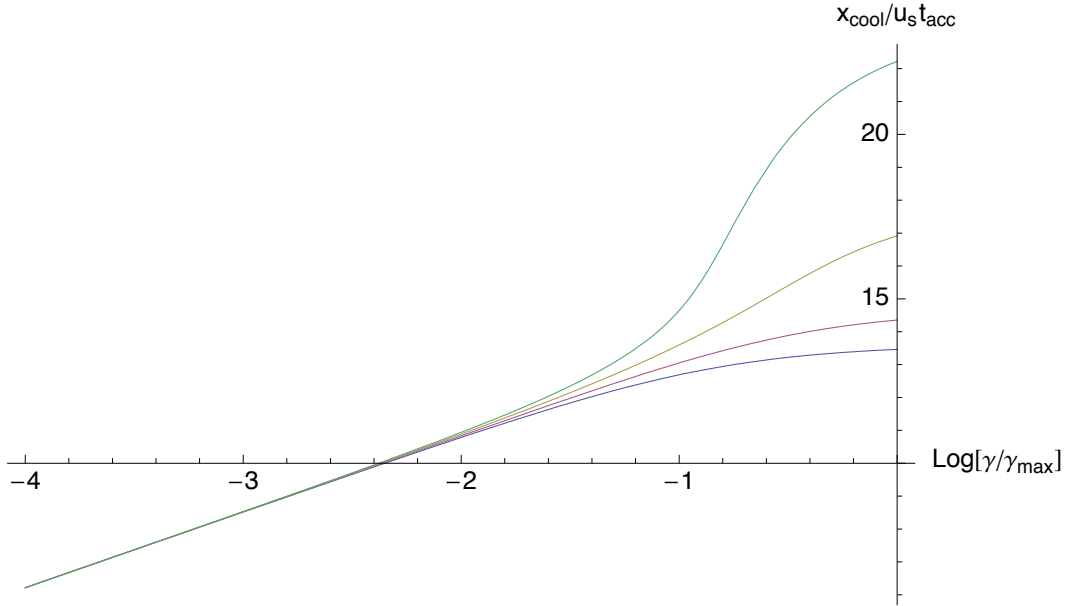


Figure 3.5: $x_{cool}/u_s t_{acc}$ as function of γ/γ_{max} at times 5 (blue), 10 (purple), 15 (yellow), 20 (green) t_{acc} . As particles reach γ_{max} at $\bar{t} \approx 15 t_{acc}$ (green curve) they cool much closer to the shock, i.e. at larger values of x_{cool} , see Fig. 3.3.

γ . An approximation good to about $\approx 10\%$ for all energy ranges can easily be found by splitting the equation into two parts: At small values of x_{cool} the exponential function dominates and one can neglect the x_{cool} term on the left hand side, resulting in a function $\propto \log \gamma/\gamma_{max}$. For larger values of x_{cool} the exponential function quickly goes to zero so that the resulting expression is $x_{cool} \propto \gamma_{max}/\gamma$.

The real problem, however, lies in the calculation of the synchrotron spectrum: performing the integrations Eqs. (3.49), (3.50) is only possible analytically when using the monochromatic synchrotron approximation Eq. (2.22). Using this approximation does not work well at all for the acceleration zone electron distribution function (for the reasons described in section 3.3.2) – but that is the zone dominating the part of the spectrum around ν_{max} so neglecting the acceleration zone emission does not seem to be a wise approximation.

One can still reproduce the clock-wise / counter-clockwise behaviour of the spectral hysteresis curves (chapter 5) with this crude approximation – but their shape is so much distorted that it does not seem wise to approximate any further (as would be necessary to further analytically calculate the IC emission). Therefore the IC emission is calculated numerically using the Melrose approximation (section 2.2.4) for the synchrotron spectrum and the approximation to the full IC kernel Eq. (2.28) that is undistinguishable from the exact expression for energetic electrons.

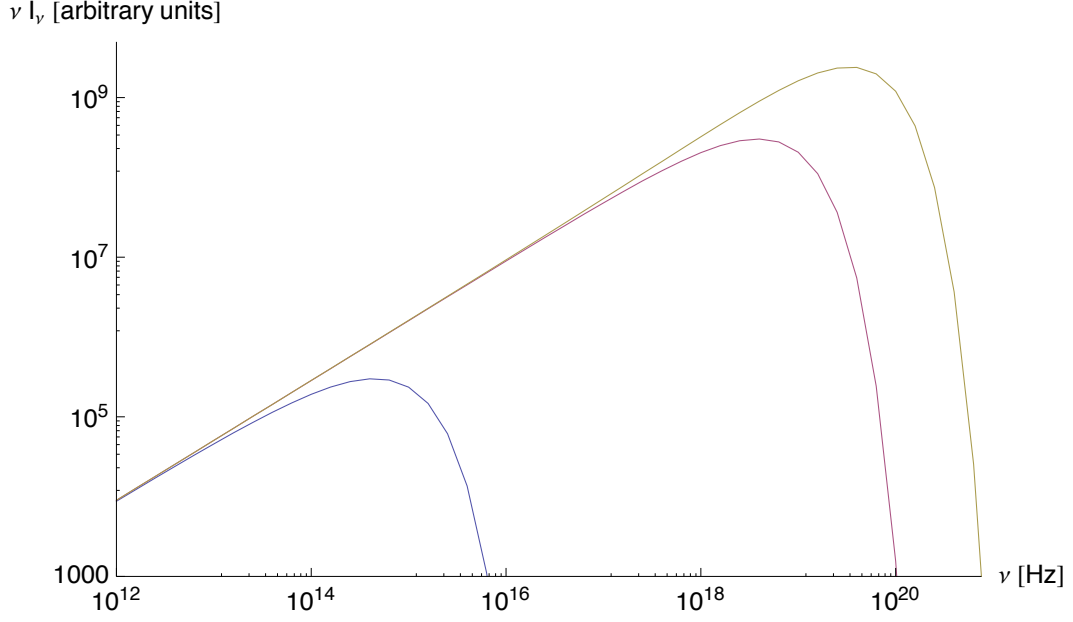


Figure 3.6: The spectrum from the acceleration zone as calculated from Eq. (3.49) for $\bar{t} = 10$ (blue), 15 (purple) and 20 (yellow) t_{acc} . For later times the spectrum does not change anymore as $\gamma_1(\bar{t} = 20t_{acc}) \approx \gamma_{max}$ for the parameters chosen.

3.5 Synchrotron Spectrum

Now to calculate the spectrum, the electron distributions that have already been integrated over the x coordinate need to be convolved with the synchrotron emissivity $P(\nu, \gamma)$, Eq. (2.26) and transformed into the observer's frame (see chapter 2.1.1).

3.5.1 Contribution from the acceleration zone

Since the acceleration zone is assumed to be infinitely thin the contribution to the intensity from the acceleration zone is easily found using a Dirac Delta function:

$$I_s(\nu, \bar{t}) = \int dx P(\nu, \gamma) \int dx N(\gamma, \bar{t}) \delta(x - u_s(\bar{t} + x/c)) \quad (3.48)$$

Rewriting the Delta function and performing the integration, one finds the intensity from the shock to be

$$I_s(\nu, \bar{t}) = \frac{a}{1 - u_s/c} \gamma_{max}^{-(t_{acc} + t_{esc})/t_{esc}} \int_{\gamma_0}^{\gamma_1(t)} d\gamma P(\nu, \gamma) \left(\frac{\gamma_{max}}{\gamma} \right)^2 \left(\frac{\gamma_{max}}{\gamma} - 1 \right)^{\frac{t_{acc} - t_{esc}}{t_{esc}}} \quad (3.49)$$

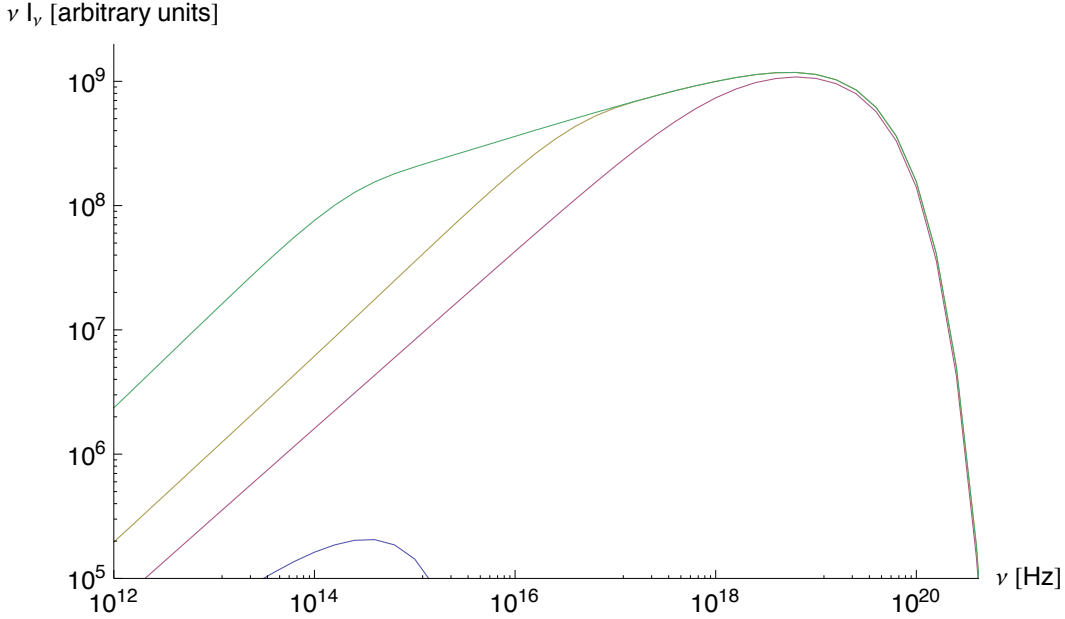


Figure 3.7: The spectrum from the radiation zone as calculated from Eq. (3.50) for $\bar{t} = 10$ (blue), 20 (purple), 50 (yellow), 500 (green) t_{acc} . One can clearly see how the break develops only at later times, because only then electrons have enough energy to cool completely inside the radiating region before escaping, resulting in a harder spectral index.

3.5.2 Contribution from the radiation zone

In the acceleration zone we have to perform a real integration over x , where the complicated behaviour of x_{cool} comes in (section 3.4.2). Again the spatially integrated electron distribution is convolved with the synchrotron power $P(\nu, \gamma)$ to yield the specific intensity:

$$I_0(\nu, \bar{t}) = \int d\gamma P_s(\nu, \gamma) \int_{x_0}^{x_1} dx n \left(x, \gamma, \bar{t} + \frac{x}{c} \right) \quad (3.50)$$

3.5.3 Transformation to the observer's frame

The total intensity is then given as the sum over the Eqs. (3.49), (3.50)

$$I_1(\nu, \bar{t}) = I_0(\nu, \bar{t}) + I_s(\nu, \bar{t}) \quad (3.51)$$

The specific intensity found this way (Fig. 3.8) has to be transformed to the observer's frame (see chapter 2.1.1) and multiplied by the ratio of projected jet cross section to the square of the distance to account for the size of the jet and the distance-square-law:

$$I_{obs}(\nu_{obs}, t_{obs}) = \frac{\pi R^2}{d_L^2} \frac{8\Gamma^2}{z+1} I_1(\nu_{obs}/2\Gamma, \Gamma(t_{obs} - \beta_b d_L/c)) \quad (3.52)$$

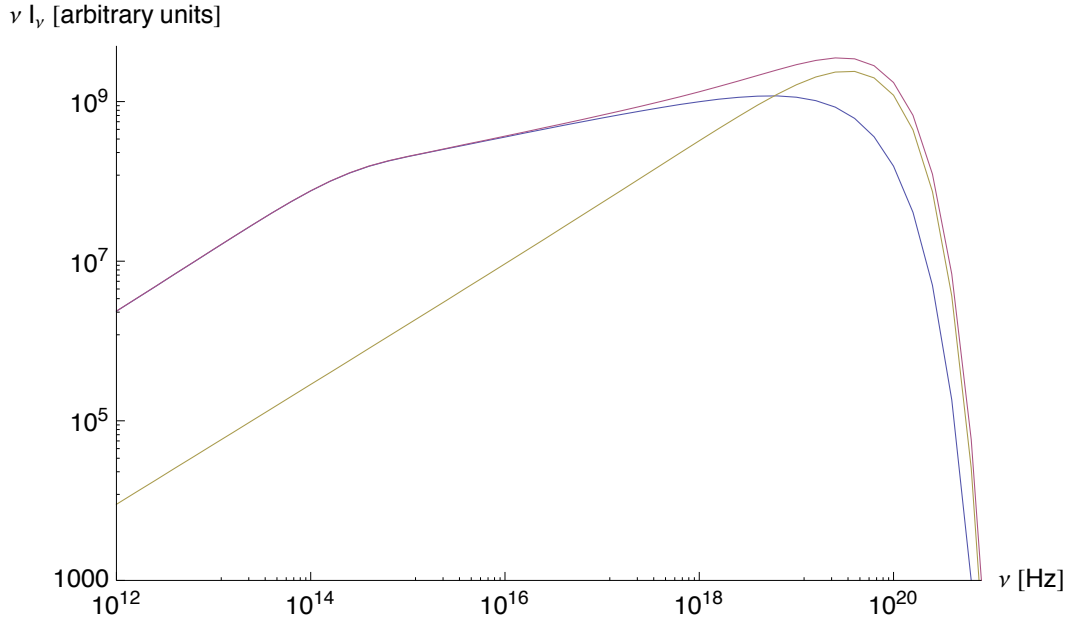


Figure 3.8: The synchrotron emissivity from both the acceleration (yellow) and radiation zones (blue) as calculated from Eq. (3.49) and Eq. (3.50) for the stationary case $\bar{t} = 500t_{acc}$. The total spectrum (purple) is dominated by the emission from the much larger radiation zone for all but the highest energies.

where $\Gamma(t_{obs} - \beta_b d_L/c)$ takes into account the (Lorentz transformed) light travel time from the distant blazar to the telescope on earth and d_L is the luminosity distance of the blazar (section 2.3). β_b is the bulk velocity in units of c .

3.5.4 Synchrotron fit for Markarian 501

Finally I show a fit to historical synchrotron data⁵ for the extreme BL Lac object Markarian (Mrk) 501 (Fig. 3.9). Mrk 501 has a redshift of $z = 0.034$ which corresponds to a luminosity distance of $4.43 \cdot 10^{26}$ cm using best values for the cosmological parameters (see section 2.3). One can clearly see the spectral break just above 10^{12} Hz. Below, electrons have so little energy that their cooling times $t_{cool} = 1/(\beta_s \gamma)$ are much longer than the energy-independent escape time t_{esc} so that they leave the source without having cooled completely, resulting in a relatively steep spectral index. Beyond the break all electrons cool completely within the source and the spectral index flattens from 0.75 to 0.25 in the νF_ν plot. At the maximum frequency observed, taken to be $5 \cdot 10^{17}$ Hz, $t_{cool} = t_{acc}$ so that particles cannot be accelerated any further. In fact, the electron distribution cuts

⁵Model and data (Catanese et al 1997) are the same as for Fig. 2 of Kirk et al (1998) but here all parameters are stated explicitly as needed later for the IC model – although some of them are not constrained by the synchrotron peak alone.

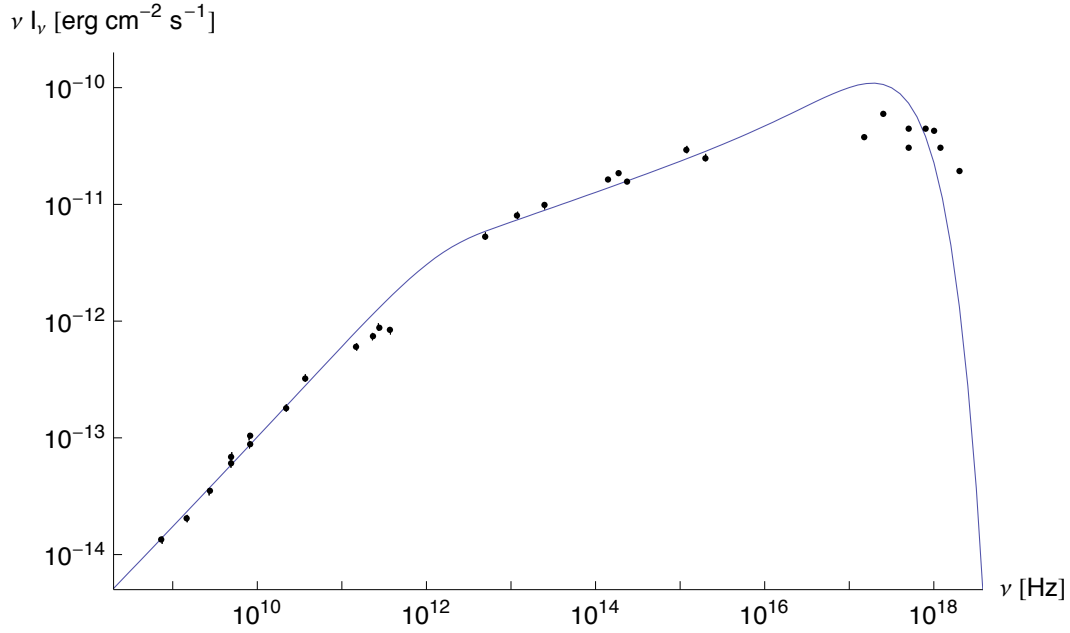


Figure 3.9: *The stationary Synchrotron spectrum from Mrk 501 with parameters as stated in table 4.1 and data from Catanese et al (1997). Further discussion see text.*

off sharply where $t_{cool} = t_{acc}$, corresponding to $\gamma_{max} = 1/(\beta_s t_{acc})$ and the radiation from above the peak frequency comes solely from the exponential cut-off of the synchrotron emissivity after the peak.

The parameters for the fit are given in table 4.1. The relation between the particle density K (cm^{-3}) and the injection function Q_0 ($\text{cm}^{-2} \text{s}^{-1}$) is given by $Q_0 = u_s K$ and the shock speed is set to $u_s = 0.1 c$ here. Note that some of the parameters (like the particle density and the blob radius) are not constrained by the synchrotron spectrum alone.

Table 3.1: *Fit parameters for the synchrotron fit to Mrk 501*

B	t_{esc}/t_{acc}	γ_0	γ_{max}	δ	K	t_b/t_{acc}	R
0.05	2	1	$3 \cdot 10^5$	10	$2.3 \cdot 10^3 \text{cm}^{-3}$	700	$6.7 \cdot 10^{14} \text{cm}$

4 Inverse Compton (IC) contribution

Here I will specify which parts of the model are affected in what way when IC scattering is considered. I will then carefully weigh those modifications against each other to find out which of them needs to be included for a first approximation. The IC spectrum is then calculated numerically and a fit for some of the latest correlated data for Mrk 501 is produced and discussed.

4.1 Extension of the model

To include the Inverse Compton (IC) effect in this model to a first approximation all losses will be neglected and the IC spectrum will be calculated from the scattering of the electron distributions, Eqs. (3.18) and (3.22), with the unaltered synchrotron spectra from both zones, Eqs. (3.49) and (3.50). The effects neglected and the reasons and justifications to do so are given here.

- **IC losses for the electron distributions** The electron distributions in both the acceleration and radiation zone would have to be corrected for IC losses according to Eq. (2.30). In BL Lac objects, however, IC scattering is thought not to dominate electron losses (Comastri et al 1997). Indeed, most observed BL Lacs show approximately equally strong synchrotron and IC peaks (in a νF_ν plot) suggesting (very roughly) equipartition between the energy densities in the magnetic field and in the synchrotron photons. Another indication that IC scatterings are not dominant in BL Lacs is that this model works very well for the synchrotron emission without considering these losses (see Fig. 3.9).
- **Losses for synchrotron photons due to Compton upscattering** IC losses for photons can also be neglected here since the number density of IC photons is smaller than the synchrotron photon number density by a factor $\approx \gamma_{max}^2$. All higher order photon loss processes, such as IC photon losses due to the ‘normal’ Compton effect will consequently also be neglected.
- **Photon pair production** ($\gamma\gamma \rightarrow e^+e^-$) becomes important for very high energy

gamma rays. But for a first approximation this can also be neglected, as the minimum required Doppler factor for gamma-ray transparency (Doni and Ghisellini 1995) is chosen so that pair production is not the dominant mechanism.

These are the physical reasons for neglecting those IC-related losses here. A more technical reason for not including IC losses of the electrons is that, in the current framework of this semi-analytical model, it would only be possible using very crude monochromatic approximations. But as the use of the Delta approximation for the synchrotron emissivity already leads to very distorted synchrotron spectra (cf. section 3.4.2), this does not seem the right way to go. On the other hand, if one wanted to include IC losses properly (Eq. (2.30)), it would require a completely numerical model as the resulting integro-differential equations are no longer analytically solvable.

So it seems a good compromise between computational effort and quality of the spectra to stay with the semi-analytical model for another while and calculate the IC spectrum for the unaltered electron and photon distributions but use the (approximation to the) full Klein-Nishina cross-section.¹

After all, as the result will demonstrate, the way I calculate the IC spectrum here can already give a good approximation to the IC emission of blazars.

4.2 Computation of the IC spectrum

The time-dependent Inverse Compton spectrum is obtained from two numerical integrations using the approximation to the full Klein-Nishina Compton kernel Eq. (2.28) in MATHEMATICA. The computer-algebra software MATHEMATICA is described in appendix B and complete and commented program (‘notebook’) listings are given in appendix C.

The IC spectrum is then given as

$$\frac{dN_{tot}(\bar{t})}{dt d\epsilon_1} = \int_{\epsilon} \int_{\gamma} d\gamma \left[N(\gamma, t) \frac{dN_{\gamma, \epsilon, acc}}{dt d\epsilon_1} \right] + \left[n(\gamma, t) \frac{dN_{\gamma, \epsilon, rad}}{dt d\epsilon_1} \right] \quad (4.1)$$

where $dN_{\gamma, \epsilon, acc, rad}/dt d\epsilon_1$ is the Compton kernel Eq. (2.28) with the number densities of photons for the two zones

$$n(\epsilon)_{acc, rad}(\bar{t}) \propto \frac{I_{0, s}(\epsilon/h, \bar{t})}{\nu} \quad (4.2)$$

¹Nonetheless it is somehow ironic to neglect IC losses: When the IC effect was first applied to astrophysical scenarios in the late 1940s, it was *only* included to describe energy *losses* and no one thought about the corresponding gains for photons. Only when the observational windows of X- and Gamma-ray astronomy were opened in the late 1950s, this process received interest as an energy gain mechanism for photons (Felten and Morrison 1966).

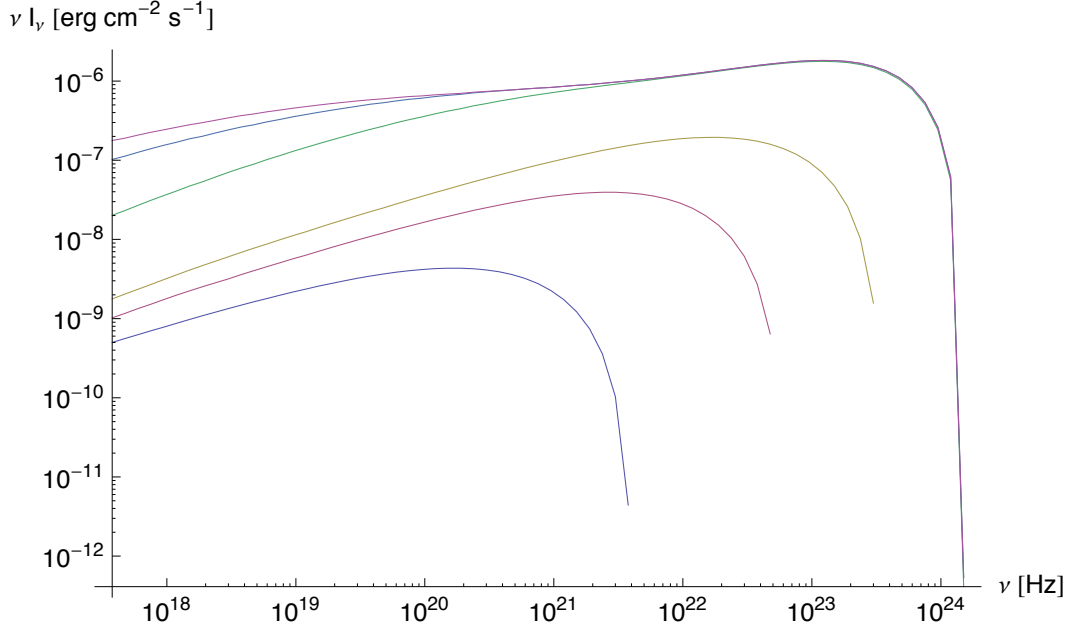


Figure 4.1: *The time-dependent Inverse Compton spectrum obtained from two numerical integrations as described in the text. The spectra are plotted for times $\bar{t} = 8, 9, 10, 20, 50$ and $500 t_{acc}$ (more energetic spectra correspond to later times). The spectral index before the peak is $\alpha = -0.5$ for early times and flattens to $\alpha \approx -0.8$ for high energies at later times.*

4.3 Time-dependent Inverse Compton Spectrum

In Fig. 4.1 the time-dependent IC spectrum is shown as it is building up from zero emission at $\bar{t} = 0$ to the spectra plotted. At early times, where the spectrum builds up with a spectral index of -0.75 (definition see Eq. (2.25)) in the synchrotron regime, it is already flatter in the IC branch with $\alpha = -0.5$. Also, the break, visible in the synchrotron spectrum (Fig. 3.7) for times greater than about $20 t_{acc}$ at the position where $t_{cool} = t_{esc}$, is smeared out here. At times later than $\approx 20 t_{acc}$, where the break begins to develop in the synchrotron spectrum, the spectrum flattens to $\alpha = -0.82$.²

While the spectral index of -0.5 is in accordance with other SSC models (e.g. Krawczynski et al 2004) one would still expect the IC spectral index to be the same as in the synchrotron regime, i.e. -0.25 for the early-time spectrum or at later times -0.25 and -0.75 before and after the break respectively. This is not the case here due to IC scattering in the Thomson regime which favours the low energy end and thus produces relatively flat spectra. The small curvature of the IC peak is problematic, however, as it does not fit very well to observations (see Fig. 4.2).

²For $-1 < \alpha < 0$ the spectrum flattens in the νF_ν plot when it steepens in the F_ν plot.

4.4 SSC fit for Mrk 501

In Fig. 4.2 the full spectral energy distribution for Mrk 501 is given as calculated from the synchrotron and IC emissions from both zones. Also plotted are simultaneous optical (KVA), X-Ray (ASM) and gamma-ray (MAGIC) data. The χ^2 value (section 2.5) has been used to find the best fit to the data. Still $\chi^2/ndof = 19.712/11 = 1.79$ for the VHE points because the curvature of the fit is a bit too large, but cannot be altered in this model.

The X-Ray peak is at $\nu_{max,X} = 6 \cdot 10^{20}$ Hz, very high compared to $\nu_{max,X} = 5 \cdot 10^{17}$ Hz from Fig. 3.9. But Mrk 501 is an extreme BL Lac object which has shown X-Ray radiation up to $\approx 10^{20}$ Hz in the past (Katarzyński et al 2001) and as this is a fit to one of the highest IC fluxes ever observed from Mrk 501 (Albert et al. (MAGIC collaboration) 2007b) the peak frequency might not be all to unrealistic.

Another feature that requires careful examination is the relation between the synchrotron and IC peak heights: In this fit the synchrotron peak outshines the IC peak by about one order of magnitude. Although this is a bit away from equipartition between magnetic and radiation field energy density, it seems required for these data also for other SSC models, see Albert et al. (MAGIC collaboration) (2007b) and references therein.

At least this synchrotron to IC peak flux ratio is consistent with the approximation that IC losses are not dominant here.

Table 4.1: *Fit parameters for the full SED for Mrk 501*

B	t_{esc}/t_{acc}	γ_0	γ_{max}	δ	K	t_b/t_{acc}	R
0.1	2	1	$7 \cdot 10^6$	25	$2.3 \cdot 10^3 \text{cm}^{-3}$	500	$2.42 \cdot 10^{14} \text{cm}$

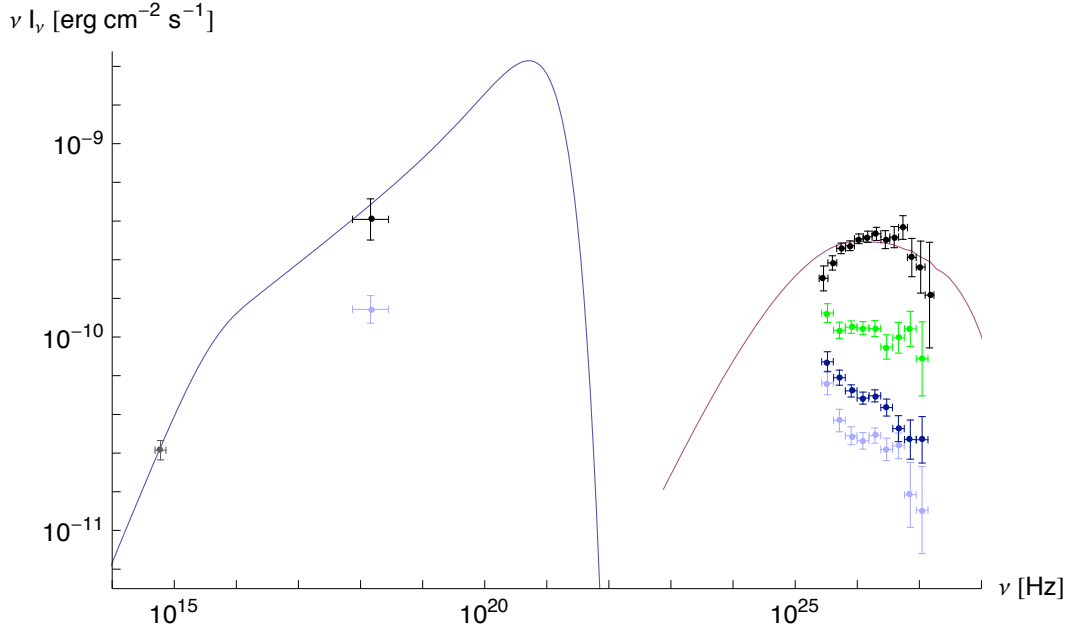


Figure 4.2: *The full synchrotron and Inverse Compton stationary spectral energy distribution from Mrk 501 with fit parameters as given in table 4.1 and data from the observational campaign from May through July 2005 (Albert et al. (MAGIC collaboration) 2007b). The optical data point is from the KVA observatory with the error coming mostly from the large uncertainty in subtracting the host galaxy. The X-Ray points are from the RXTE satellite’s all-sky monitor (ASM) and the high-energy points are from MAGIC. The gamma-ray data have been corrected for EBL using the ‘low’ EBL model from Kneiske et al (2004). Light blue points are the average low-flux emission during the observational campaign, dark blue points correspond to medium flux and green points to the high-flux dataset (integral flux above 150 GeV > 1.0 Crab unit, where one ‘Crab unit’ is the flux from the supernova remnant and gamma-ray standard candle Crab nebula). The optical data have been averaged over all times as they do not show much variability. Black points are from the strongest flare seen during that campaign (June 30) for which the parameters have been optimized. As can be seen, the curvature of the VHE points is not correctly given by the model, see text for further discussion.*

4 Inverse Compton (IC) contribution

5 Variability

Variability can occur for a number of reasons. In the shock-in-jet model the easiest way to produce a flare is to set the particle injection function $Q(t)$ to a higher value for a certain time. This could be the case if the shock runs over a region of increased particle density. As magnetic fields are frozen into the particles in highly conductive plasmas, one might then expect the magnetic field to vary, too, i.e. the maximum attainable electron Lorentz factor to change. Therefore, another value that could be varied to produce a flare is the maximum electron Lorentz factor $\gamma_{max} = 1/\beta_s t_{acc}$.

5.1 Modelling a flare

During a flare of time t_f , the injection function is enhanced by a factor of η_f simply by setting

$$Q(t) = \begin{cases} Q_0 & \text{for } t < 0 \text{ and } t > t_f \\ (1 + \eta_f) Q_0 & \text{for } 0 < t < t_f \end{cases} \quad (5.1)$$

The intensity during a flare is then given by

$$I_{flare}(\nu, \bar{t}) = I_1(\nu, \infty) + \eta_{f,syn,ic} [I_1(\nu, \bar{t}) - I_1(\nu, \bar{t} - (1 - u_s/c)t_f)] \quad (5.2)$$

where $\eta_{f,syn} = \eta_f$ and $\eta_{f,ic} = (1 + \eta_f)^2 - 1$ because in the inverse Compton regime the peak height is $\propto Q^2$ as both the particle density and the seed photons are increased by η_f .

The flare presented in the following discussion is produced using the model parameters of table 5.1 and the flare parameters $t_f = 10t_{acc}$, $\eta_f = 1$, i.e. a doubling of the injection function for 10 acceleration times. With respect to the fit parameters for the Mrk 501 fit, Fig. 4.2, less extreme values have been chosen to calculate the flare spectra. The choice of parameters is not overly important for the production of flares within this model. However, the reason for choosing a rather conservative set of parameters (no extreme value for γ_{max} , for example) is that these seem to be the more general case, applicable to a large

number of blazars.

Also the (unphysical) choice $u_s = 0$ is made to simplify calculations. At any time this does not alter the spectra in the region of interest here, namely the one close and around the maximum of the emission.

Table 5.1: *Model parameters for the flare*

B	γ_0	γ_{max}	δ	K	t_b/t_{acc}	R
0.3 G	1	$1 \cdot 10^4$	25	$6 \cdot 10^4 \text{cm}^{-3}$	100	$1 \cdot 10^{15} \text{cm}$

5.2 Flaring behaviour I: Intensity profiles

In Figures 5.1 and 5.2 a flare of duration $10t_{acc}$ is produced as described above and followed over $50t_{acc}$ with only characteristic times plotted. To reach $\gamma_{max} = 10^4$ electrons take $t_{rise} \approx 11$ acceleration times (cf. Fig. 3.1). Since for electrons with $\gamma = \gamma_{max}$ the cooling time equals the acceleration time it is to be expected that after $t_{max} \approx t_f + t_{rise}/2 = 15.5t_{acc}$ the maximum should be reached. Indeed, after $\approx 17t_{acc}$ (red curves) the maximum is reached. Cooling sets in after that and it can clearly be seen that cooling is more efficient at higher energies: $26t_{acc}$ (blue curves) after the beginning of the flare the emission has almost fallen back to the stationary level at the peak frequency, while it is still going on at lower frequencies. In the IC peak the flare takes longer at the peak frequency because lower energy photons still get upscattered to the maximum frequency when the synchrotron flare has already decayed at the peak frequency. Both spectra cover roughly five orders of magnitude in frequency and about one and a half orders of magnitude in intensity.

In Figures 5.3 and 5.4 the intensity (normalised to the stationary emission at the respective frequency) at the four frequencies $\nu/\nu_{max} = 1/100, 1/10, 1, 10$ is plotted against time. The most prominent feature here is that, at the lowest frequency (red curve), the fall time is considerably longer than at higher frequencies due to the energy-dependent cooling rate. The rise time, on the other hand, is similar for all four curves. Note that all curves start at later times in the IC plot since the IC emission can only flare after the seed photons have been produced. A discontinuity arises $10t_{acc}$ after the rise sets in due to the modelling of the emission mechanism, Eq. (5.1). Also, in order not to consume too much computer time, only one spectrum per t_{acc} has been produced which is responsible for the remaining parts where the curves are not differentiable.

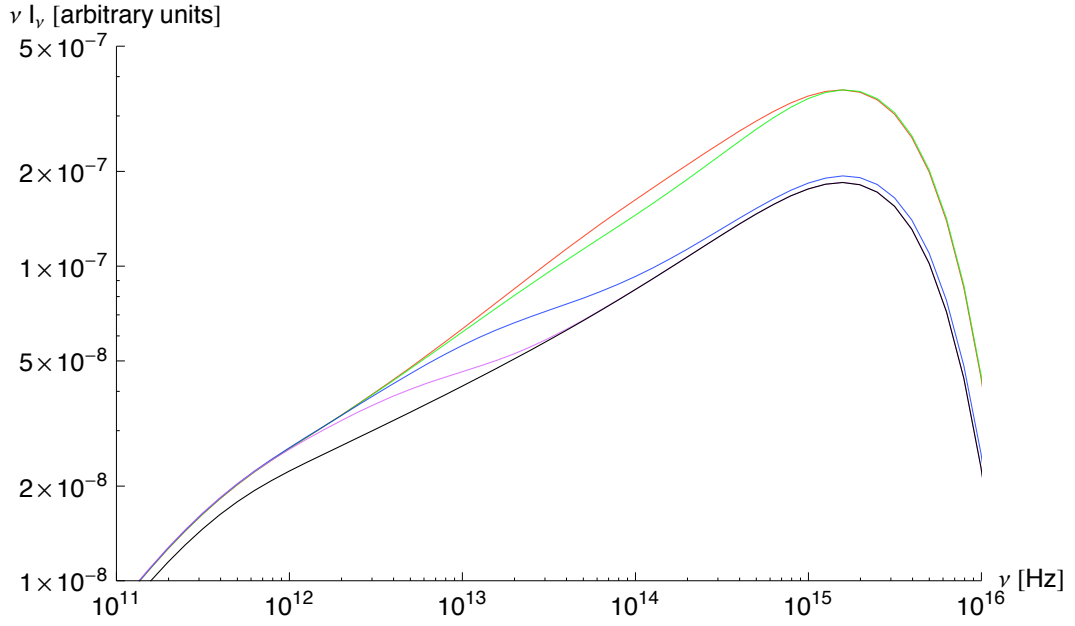


Figure 5.1: *The synchrotron spectrum at characteristic times during a flare as described in section 5.2. The stationary emission is plotted in black, the other colours correspond to $\bar{t}/t_{acc} = 17$ (red), 19 (green), 26 (blue), 36 (purple). See text for further discussion.*

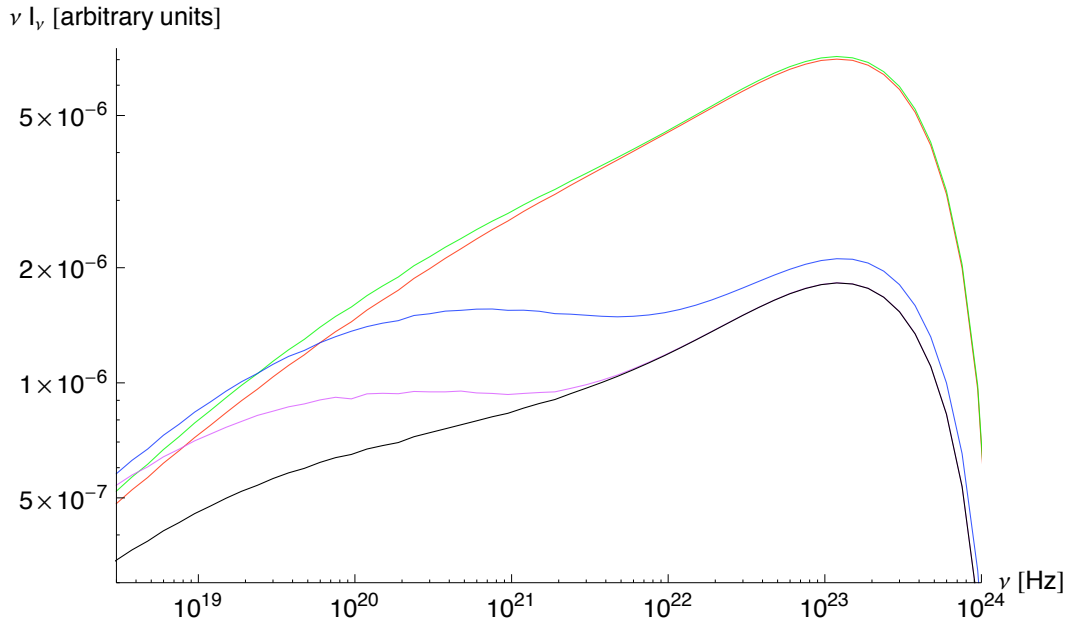


Figure 5.2: *The Inverse Compton spectrum at characteristic times during a flare as described in section 5.2. Colour coding is the same as above (Fig. 5.1). See text for further discussion. The wobbles around 10^{20} Hz are numerical artefacts.*

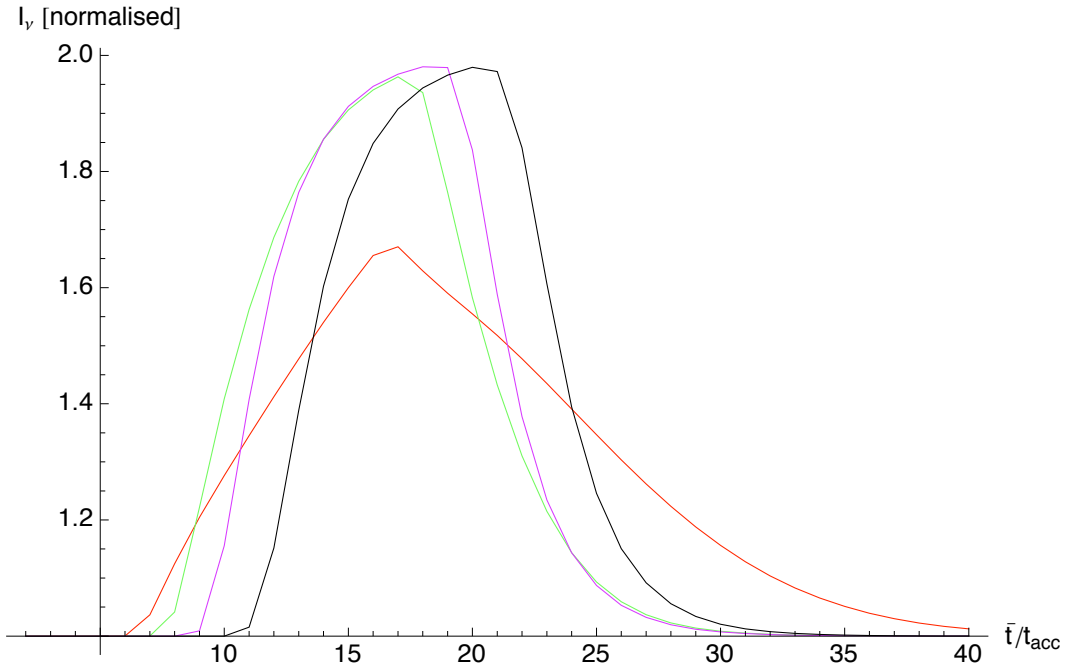


Figure 5.3: Plot of synchrotron intensity versus time of a flare as described in section 5.2 at frequencies $1/100$ (red), $1/10$ (green), 1 (purple), 10 (black) times ν_{max} . The intensity has been normalised to the stationary (pre-flare) emission at that frequency. Further discussion see text.

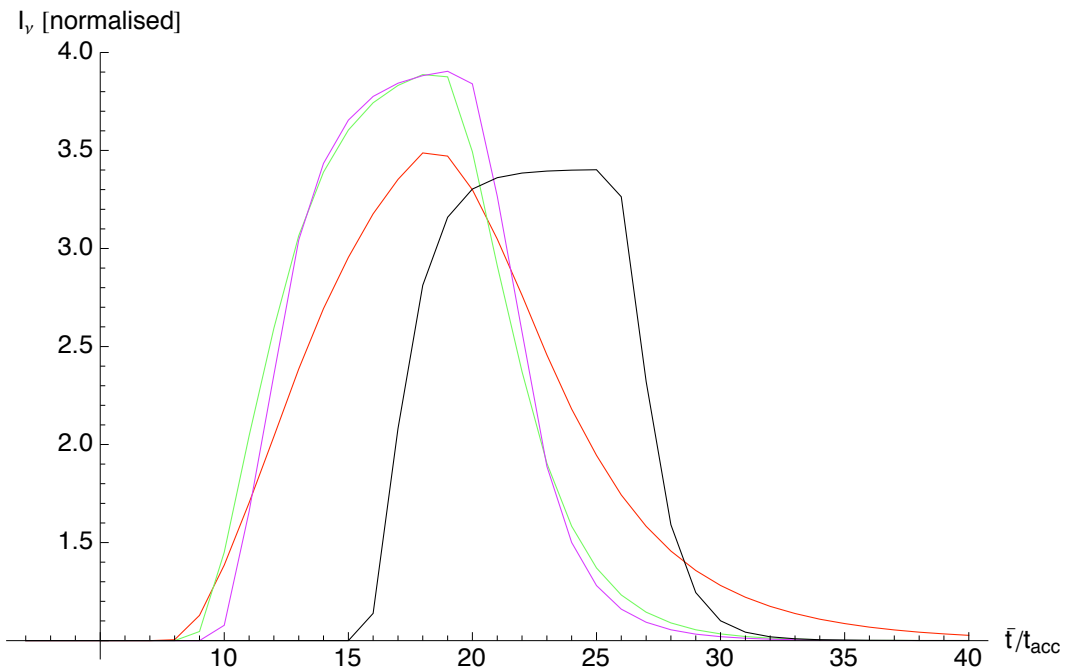


Figure 5.4: Plot of Inverse Compton intensity versus time (in t_{acc}) of a flare resulting from an increase in electron injection of a factor of 2 for a duration of $10 t_{acc}$ at different frequencies. Colour coding as in Fig. 5.3.

5.3 Flaring behaviour II: Spectral Index variation

In Figures 5.5 and 5.6 the change of the spectral index with respect to the spectral index for the stationary (pre-flare) state is plotted

$$\Delta\alpha(t) = \alpha_{flare}(\nu, \bar{t}) - \alpha(\nu) \quad (5.3)$$

So, curves for different frequencies (colour coding from low to high frequencies according to the visible spectrum of colours) can be shown in one plot and the differences can be seen easily. Also, as the absolute spectral index is not a very reliable prediction of this model, the relative values should compensate for some of the inaccuracies of the model.

The spectral index is defined here as

$$\alpha(\nu_1) = \log \left[\frac{F(\nu_2)}{F(\nu_1)} \right] / \log \left[\frac{\nu_2}{\nu_1} \right] \quad (5.4)$$

with $\nu_2 > \nu_1$ and close to each other.

The general behaviour is the same in both the synchrotron and the IC regime: At low frequencies a hard lag behaviour (hardening follows softening) is seen, at high frequencies the situation is vice versa, a soft lag is produced. Considering the discussion in this section the behaviour is immediately clear: Radiation is more efficient at high than at low frequencies so that more radiation is produced there at the beginning, resulting in a steepening (in the νF_ν plot, $\Delta\alpha > 0$) at low and a flattening ($\Delta\alpha < 0$) at high frequencies. Later, when electrons have had time to cool, more radiation is produced at lower frequencies resulting in the opposite behaviour. There is not much difference between the synchrotron and IC plots here, except that the amplitude of the spectral index variation is almost twice as large in the IC regime. Non-differentiable and ragged parts of the curves are due to numerical resolution effects. But notice how e.g. the second peak of the red curve (more distinguished in the synchrotron plot) evolves to the purple ‘full’ peak for higher frequencies.

5.4 Variation of spectral index with flux (Hysteresis)

Now, plotting the flare-intensity and spectral index curves in one plot using the flare time as the parameter one arrives at the well known spectral hysteresis curves that are shown in Figures 5.7 to 5.12 for $\nu/\nu_{max} = 1/100, 1/10, 1$ on the following pages. Discussion follows in section 5.6.

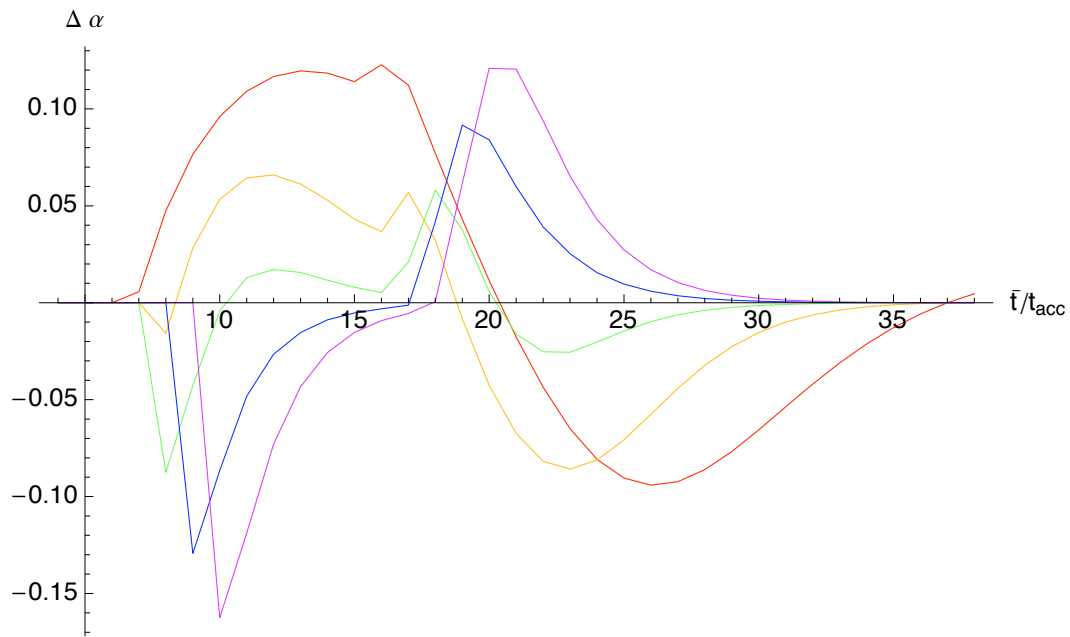


Figure 5.5: Plot of the synchrotron spectral index versus time of a flare as described in section 5.3. The curves correspond to $\nu/\nu_{max} = 1/100, 1/30, 1/10, 1/3, 1$ (from red to purple).

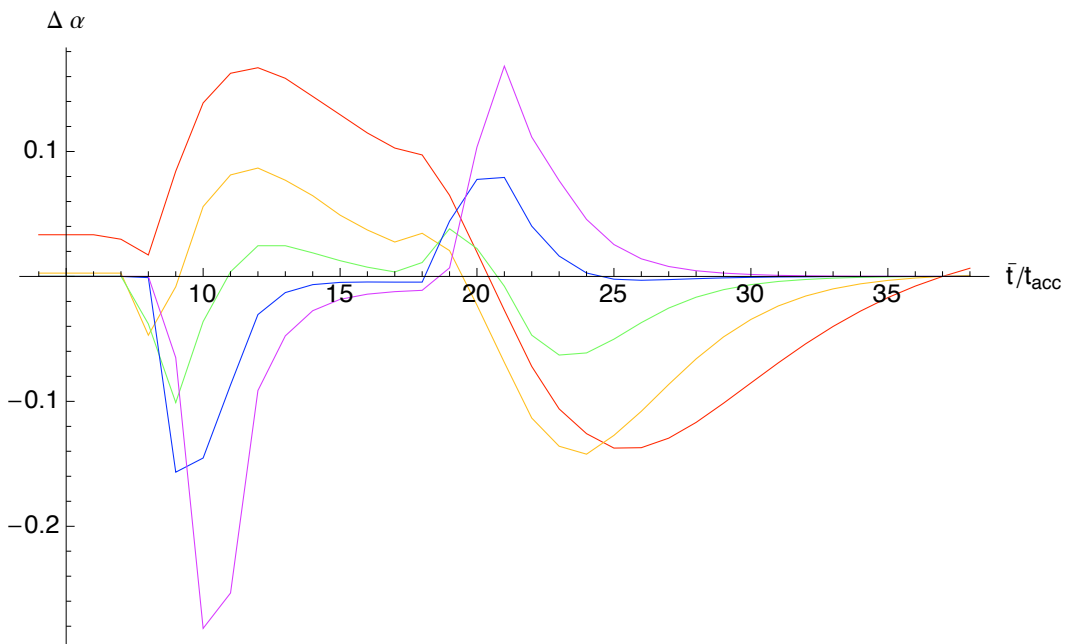


Figure 5.6: Plot of the Inverse Compton spectral index versus time of a flare. Colour coding as in Fig. 5.5.

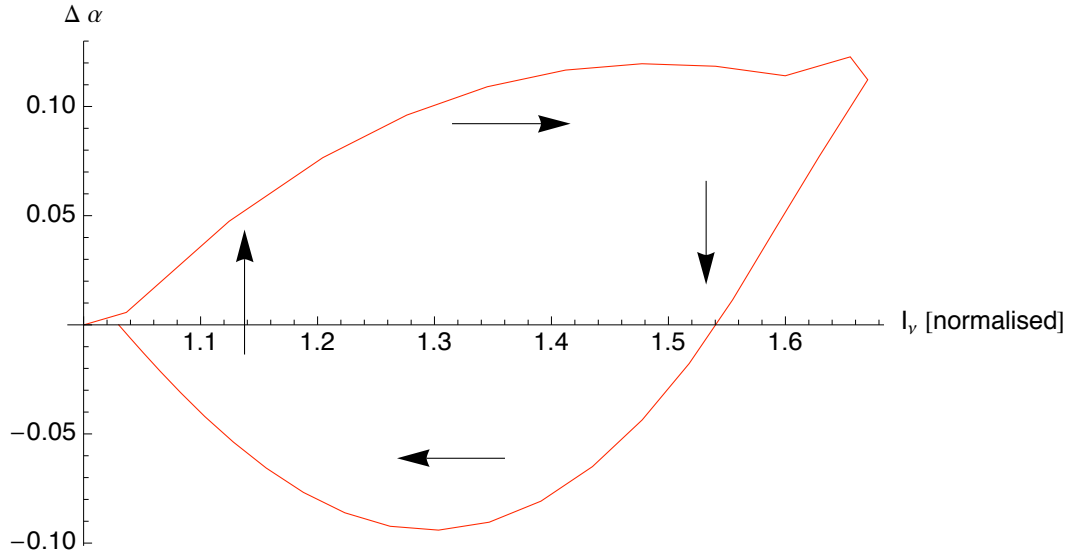


Figure 5.7: Parametric plot of synchrotron intensity versus synchrotron spectral index with the parameter time ($\bar{t}/t_{acc} = 1 \dots 34$) of a flare resulting from an increase in electron injection of a factor of 2 for a duration of $10 t_{acc}$ at low frequencies, $\nu = 1/100\nu_{max}$.

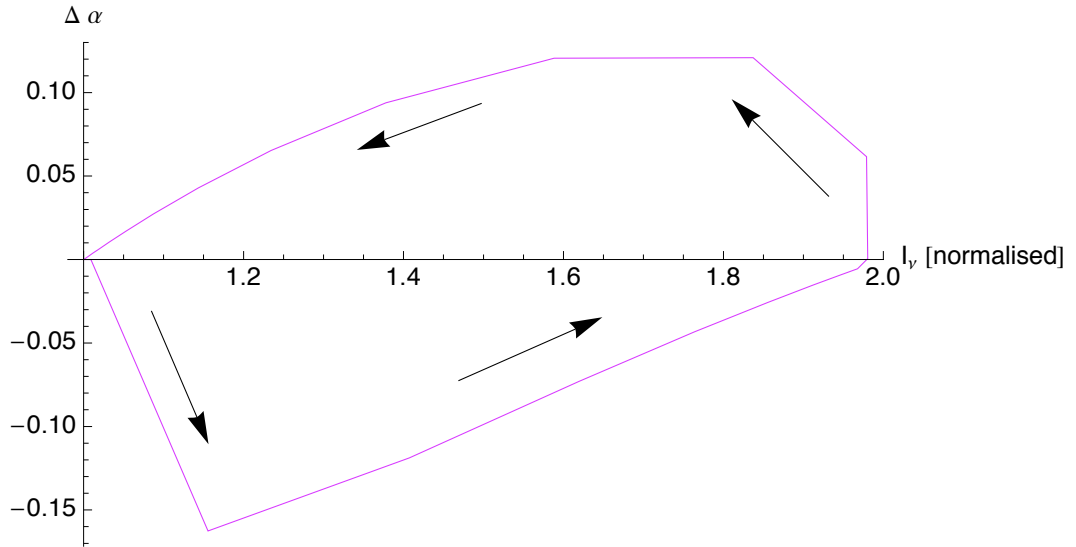


Figure 5.8: Spectral hysteresis curve of the synchrotron flare as in Fig. 5.7, but at the maximum frequency.

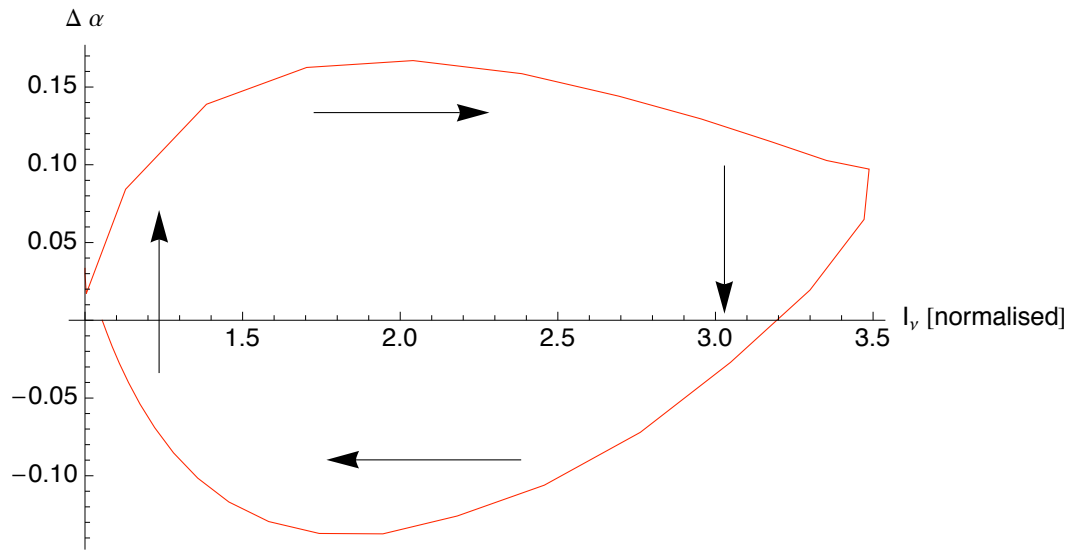


Figure 5.9: Parametric plot of Inverse Compton intensity versus Inverse Compton spectral index with the parameter time ($\bar{t}/t_{acc} = 1 \dots 34$) of a flare resulting from an increase in electron injection of a factor of 2 for a duration of $10 t_{acc}$ at low frequencies, $\nu = 1/100\nu_{max}$.

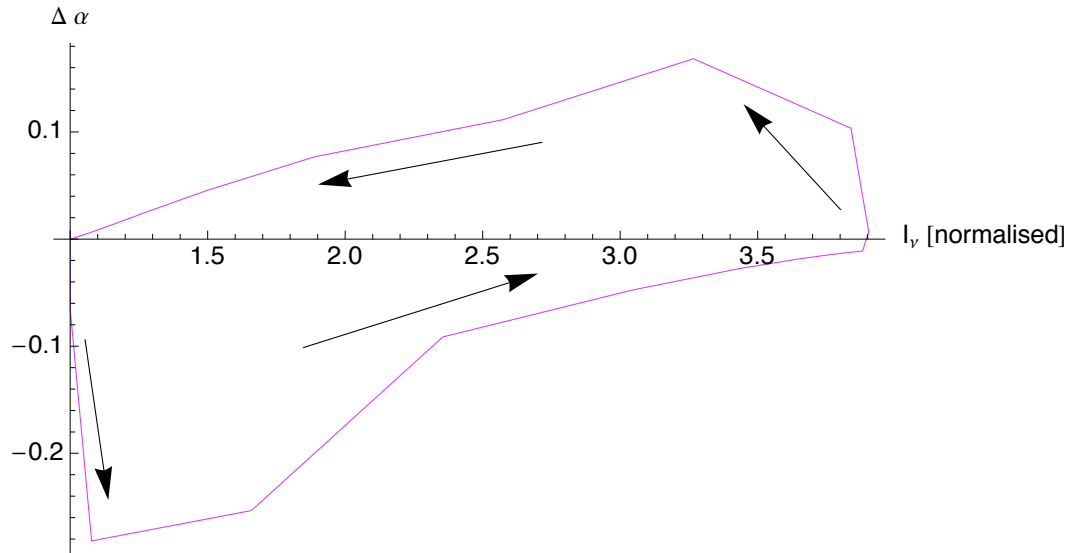


Figure 5.10: Spectral hysteresis curve of the IC flare as in Fig. 5.9, but at the maximum frequency.

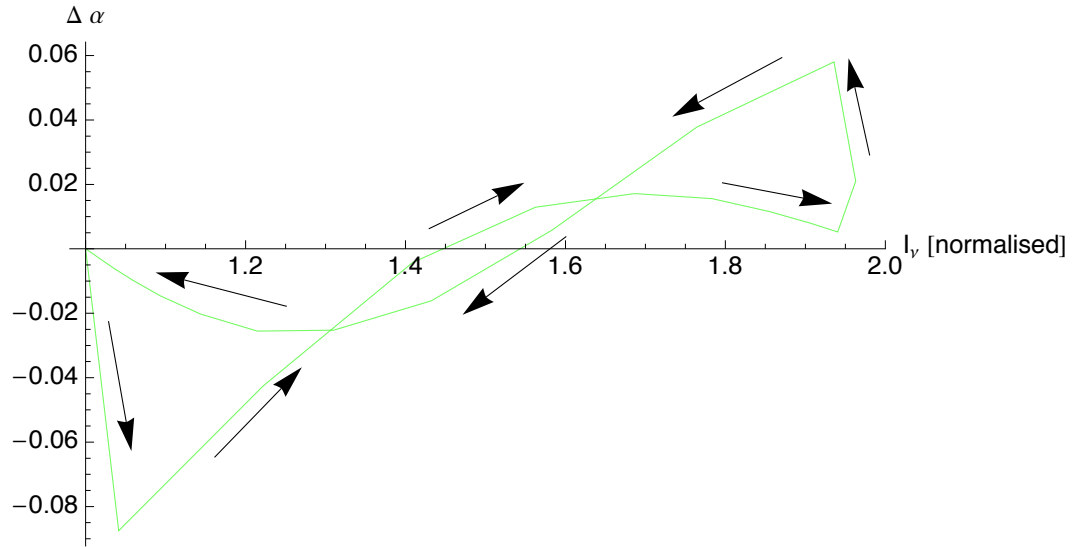


Figure 5.11: *Parametric plot of synchrotron intensity versus synchrotron spectral index with the parameter time ($\bar{t}/t_{acc} = 1 \dots 34$) of a flare resulting from an increase in electron injection of a factor of 2 for a duration of $10 t_{acc}$ at medium frequencies, $\nu = 1/10\nu_{max}$ where the transition between clock-wise and counter-clock-wise behaviour occurs.*

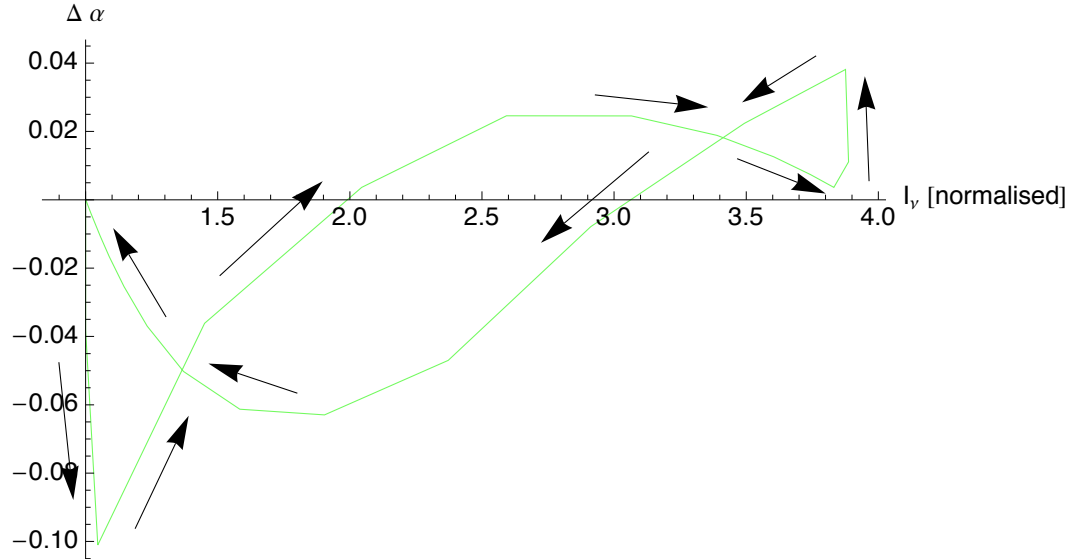


Figure 5.12: *Spectral hysteresis curve at the medium frequency as in Fig. 5.11, but for the IC regime.*

5.5 Timescales

The Synchrotron model was originally built to explain spectral variability in X-Rays of the order of several hours ($10^3 \dots 10^4$ s) as observed in various sources (Gear et al 1986; Sembay et al 1993; Takahashi et al 1996). It is obvious to first apply the IC extension to the same timescales since the IC spectrum is produced by the same electrons that are made responsible for the synchrotron flares. However, the model is largely scale-invariant since all transient phenomena are expressed in terms of t_{acc} . But of course there are physical limits for the observable variability time scale. A lower limit is given by the causality relation $t_{var} \gg R/c$, reasoning, that time variability shorter than the light travel time through the source would be dominated by geometrical effects rather than the intrinsic spectral behaviour ascribed to acceleration and cooling. Assuming $t_{var} \approx t_{cool}$ one gets the following lower limit on the observable variability time that could be explained with this model

$$t_{var,obs,min} \geq 400 \text{ s} \left(\frac{0.1 \text{ G}}{B} \right)^2 \left(\frac{10^7}{\gamma_{max}} \right) \left(\frac{25}{\delta} \right) \left(\frac{R_{jet}}{10^{14} \text{ cm}} \right) \quad (5.5)$$

So, time variability much shorter than several hours could be explained in principle and variability in the range of the very fast flux doubling times of just two minutes that MAGIC has recently seen in Mrk 501 (Albert et al. (MAGIC collaboration) 2007b) can also be described with the model. Although the flare was produced for different parameters as the SSC fit for the Mrk 501 emission, the model can also produce spectral hysteresis curves for different parameters. Nonetheless it would be very interesting to observe the same variability also on an hour-scale – if it looks similar one might reason that the same processes are at work on different time scales.

Variability in the VHE band might also be modulated by a precessing jet, bent by the tidal forces of a putative central super-massive black-hole binary system, as has been put forward to explain the 23 day variability in Mrk 501 (Rieger and Mannheim 2000).

To get an impression of the size of the emitting blob, consider the knot HST-1 in M87 that is believed to be a site of gamma ray flaring emission. In the blob in jet model only a small region inside this structure could be responsible for the gamma-ray emission as the size of the blob is canonically $10^{15} \text{ cm} = 3 \cdot 10^{-4} \text{ pc}$ whereas the HST-1 knot is about 1 pc in diameter. The VLBI knots C2, 3, 4 of Mrk 501 are also $\approx 1 \text{ pc}$ in diameter.

5.6 Observations of variable high-energy spectra

In Figures 5.7 to 5.12, spectral hysteresis curves for the synchrotron and IC regime and at different frequencies were plotted, showing that both a clock-wise (at lower frequencies) and a counter-clockwise (at higher frequencies) behaviour can be produced with this model – also in the IC regime, which, in the context of an SSC model, has not been shown before. Again, differences between the synchrotron and IC curves are small and probably more due to numerical resolution problems than due to physical differences (in this model). Of course the intensity amplitude is larger in the IC case, but we put that in in the beginning, Eq. (5.2).

In a recent campaign MAGIC has observed Mrk 501 over several months in 2005 and caught two very bright flares on June 30 and July 9 for which it was possible to produce spectra – or at least the so called ‘hardness ratio’ that is defined as the ratio of the flux at two specified energy ranges. Here, as the peak lies at ≈ 1 TeV (see Fig. 4.2), the energy bins to calculate the hardness ratio from were chosen as 0.25 to 1.2 TeV and 1.2 to 10 TeV. The so derived hardness ratio vs. flux plots are reproduced in Fig. 5.13. The comparison with the corresponding theoretical curve Fig. 5.10 on page 56 is very encouraging: The qualitative behaviour of the observed hysteresis is consistent with the prediction from the model. By lucky coincidence the peak emission during that flare was in the observable window of the MAGIC telescope and so the comparison with the model was easily possible. The observed intensity amplitude of the July 9th’s flare, taken to be the ratio of the fluxes from points ‘9’ and ‘7’ of Fig. 5.13, is about 3.3 – suggesting roughly doubling of the injected electrons. Of course absolute values for the hardness ratio do not correspond to the calculated $\Delta\alpha$ values. A model plot of hardness ratio against flux might try to even give a quantitative fit to the observed short-time variability, constraining the acceleration mechanism at work. Future simultaneous observations of a peak in the IC spectrum at energies well below the peak could help confirming – or disproving – the model.

To better constrain the model it would be very helpful to have good simultaneous X-Ray data. Then one could test if the spectral hysteresis is described in the same sense in the X-Ray regime or, with even better spectral coverage, if the different variability patterns can be seen at different frequencies.

Let me add a short note concerning the observability of hour-scale variability with a ground-based gamma-ray telescope. It would be difficult for such a telescope to observe a specific source over more than a few hours as the zenith angle of the sources changes dramatically in that time and with that the energy-cutoff of the telescope changes as

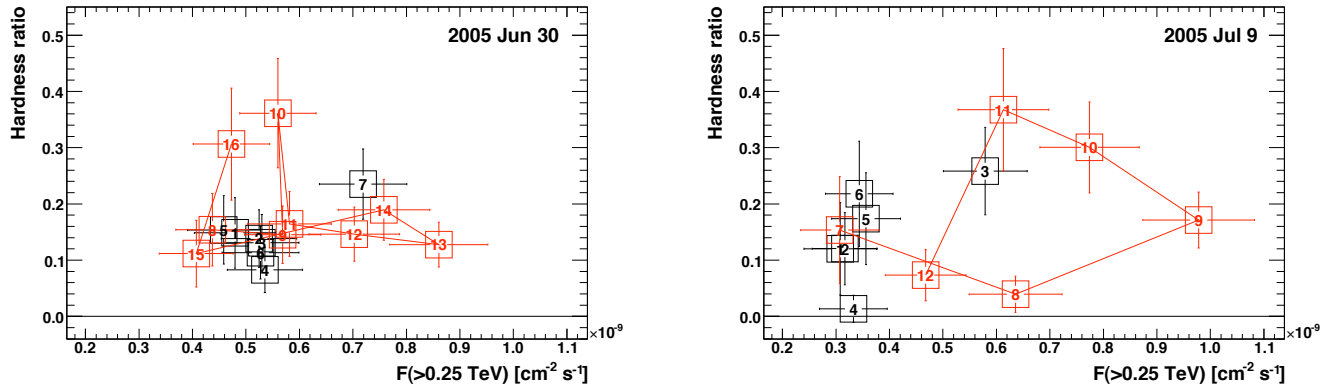


Figure 5.13: *Spectral hysteresis curves for two strong flares in Mrk 501 seen by MAGIC on June 30 and July 9, 2005 (Albert et al. (MAGIC collaboration) 2007b). Black and red numbers indicate pre-burst and in-burst emission and the numbers give correspond loosely to the time with the total time of the flares being about 20 minutes. Note the close resemblance to the spectral hysteresis pattern that has been produced from the model, Fig. 5.10.*

well, leading to higher cut-off energies for larger zenith distances. Observing a source with multiple gamma-ray telescope spread over the longitudes, this problem could in principle be overcome.

6 Summary and Discussion

6.1 Summary

In this work I extended the semi-analytic two-zone model for particle acceleration and synchrotron emission in blazar jets of Kirk et al (1998) with the Self-Compton contribution and looked at the time-dependence of the spectra in the Inverse Compton (IC) regime. As expected, spectral variations were found that are very similar to those in the synchrotron regime. The most important point here is that, both in the synchrotron and in the IC branch, spectral hystereses are produced by that model when looking at a flare.

After giving a brief introduction, chapter 1, where the complexity of the topic was illustrated and some connections to other areas of current research in astrophysics and cosmology were shown up, I explained the most important theoretical background, chapter 2. The advantage of using two zones was explained in section section 3.2 – namely, being able to model the acceleration process time-dependently and thus producing certain spectral patterns that cannot be explained in a simple one zone model. In chapter 3 the analytical model of Kirk et al (1998) was reproduced and thereby some minor errors and imperfections of the original paper were found and – thanks to helpful discussion with Prof. John Kirk – corrected. section 3.4.2 explains why the analytical model gets numerical in the end and shows that good analytic approximations for the transcendental equation responsible for this may be found but in the end one has to use a formular for the synchrotron emissivity that makes it impossible to proceed analytically.

In section 3.5 the calculation of the synchrotron spectra from both zones is shown and the reproduction of the original paper is completed by fitting the model to archival data for the well-studied blazar Mrk 501.

Chapter 4 first gives an overview of how the model would need to be changed to include all implications of IC scattering. It is then argued that for finding the desired spectral behaviour, several terms can be neglected as they do not influence the blazar spectra significantly. The IC spectrum is then calculated from the unaltered photon and electron distributions using an approximation to the full Klein-Nishina cross-section and the spectrum is fitted to recent simultaneous optical, X-Ray and VHE data. Although the

curvature of the IC emission around the peak is not exactly matched, the fit shows that the approximations taken can well reproduce the spectral behaviour.

In chapter 5 it is demonstrated that a flare can be produced in the context of this model by setting the electron injection function temporarily to a higher value. In sections 5.2 and 5.3 the flaring behaviour of the intensity and the spectral index is studied and physical explanations for it are given. A section on timescales, section 5.5, justifies the application of this model not only to the hour-scale variability, it was originally designed for, but also for the much shorter variability times, down to two minutes, that is seen by modern gamma-ray telescopes. Comparing the spectral behaviour of such a flare (Albert et al. (MAGIC collaboration) 2007b) with the theoretical prediction, one finds a nice consistency.

6.2 Discussion

While giving approximate fits to observational data, the time-dependent spectral behaviour can only be claimed to be given qualitatively at the moment, as the curvature of the IC spectrum in the fit Fig. 4.2 is not matched good enough. This might be an effect of overestimation of the high-energy electron population due to the neglectance of the IC losses of the electron distribution. Another indication that the high-energy part of the electron distribution needs to be modified comes from looking at the most recent X-Ray data from the Japanese satellite Suzaku (Hayashida et al. 2007, to be published) for the same source, Mrk 501. Due to the use of first-order differential equations a Θ function appears in the electron distribution that cuts it off in the sharpest possible way: The electron distribution function falls abruptly to zero at $\gamma = \gamma_{max}$. While for the archival data Kirk et al (1998) chose, that produced a very good fit (see, e.g., Fig. 3.9), in the light of more recent observations like the one from the recent Suzaku campaign this aspect of the model needs to be taken to reconsideration as well. An improvement might result from including energy-space diffusion effects (second order derivatives in energy), that would smoothen the cut-off. Webb et al (1984) tried this for a time-independent model which resulted in a set of rather unhandy equations that they solved numerically. Another way to produce a smooter cut-off would be to assume an inhomogeneous source region or different acceleration mechanisms. A power law fit beyond γ_{max} as often included by ad hoc modelers (Krawczynski et al 2004; Tavecchio et al 1998). Although that might readily produce very good fits in terms of small values of χ^2 , I think the more physical approach undertaken here will eventually be more successful in giving a profound physical modelling of the phenomena related to relativistic jets.

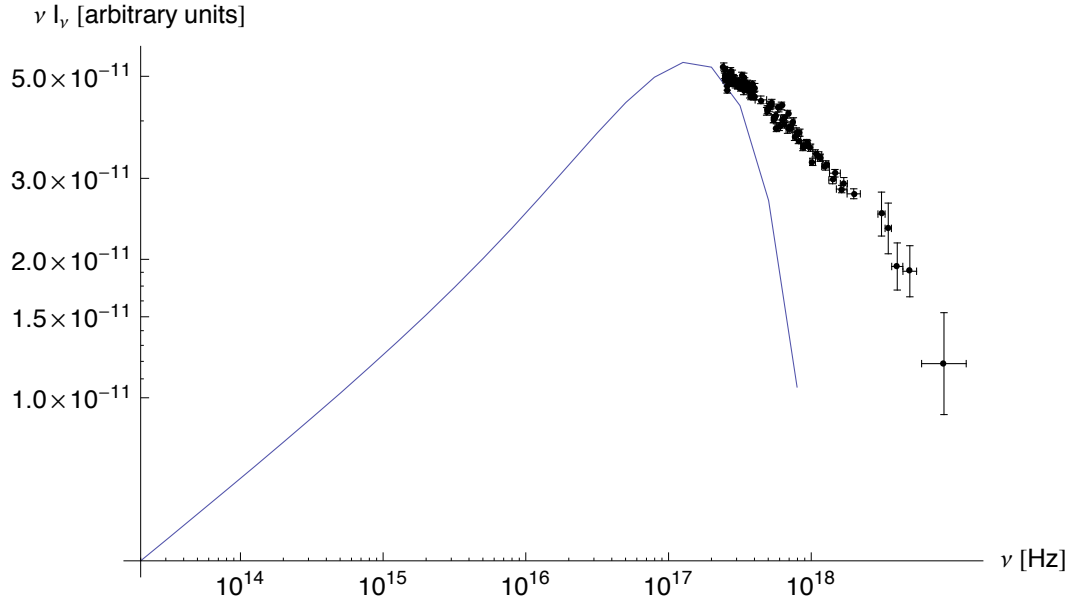


Figure 6.1: After γ_{max} the electron distribution of the model fit is cut-off abruptly as a consequence of using first order differential equations for the electron distribution function. As a result, the synchrotron emission after the peak comes solely from the exponentially decaying part of the synchrotron's emissivity function and falls too steep to explain these recent Suzaku observations (Hayashida et al. 2007, to be published). Further discussion see text.

Acceleration is another weak point of the model. While the use of two zones with its time-dependent modelling of acceleration is a huge improvement over one-zone models, a more physical treatment of acceleration would involve the energy-dependent diffusion coefficients so that the acceleration and escape times would become energy-dependent. Kirk et al (1998) give the energy-dependent solution in the appendix¹ for a simple ‘gyro-Bohm’ diffusion coefficient, i.e. $t_{esc,acc} \propto \gamma$. Bhattacharyya et al (2002) found that in the case of energy-dependent acceleration time, no ‘hard lag’ behaviour is produced. Also, rise and decay times of the flaring behaviour strongly depend on whether or not acceleration and escape are modelled time-dependently, the system reaching a steady state much faster in the case of energy-dependent time scales. As the spectral behaviour of the flares can give clues to the acceleration mechanism involved, a close interplay between model builders and observers is needed to constrain the model further.

Another point that would also need to be overcome in a more physical model is the production of a flare. Here, a flare is modelled as a sudden increase in the particle injection function – which is certainly unphysical. This might actually be a good starting

¹But note that all γ s in the brackets of their Equation (A5) should be squared, as discovered by Bhattacharyya et al (2002))

point for further work as the shape of the particle injection function $Q(t)$ is likely to influence the flares produced.

6.3 Prospects

Several new observatories for the most violent processes at work in the universe are being constructed at the moment. One of the most eagerly longed for is the new Gamma Ray Large Area Space Telescope (GLAST) (Gehrels and Michelson 1999) that will probably detect several hundreds sources of high energy photons greatly improving the statistics on these sources. With an energy range of roughly 20 MeV to 300 GeV and simultaneous observations with ground-based gamma-ray telescopes that cover the energy-range up to several TeV, a much larger part of the VHE part of the spectrum will be accessible for observation. This will also help models such as this one as it will be possible to observe a flare over both the regimes where a hard and a soft lag is expected from this model. If the transition from hard to soft lag in going from frequencies around the peak to smaller ones, is not seen, this two zone model can effectively be ruled out as an approximation to blazar physics. If, on the other hand, both hard and soft lags could be seen from the same flare this would strongly speak in favour of this model.

7 Zusammenfassung (German Summary)

In dieser Arbeit wurde das zeitabhängige Zweizonenmodell von Kirk et al (1998), das die Teilchenbeschleunigung und Synchrotronemission in Blazar-Jets beschreibt, um den Selbst-Compton Beitrag erweitert. Mit dem so erweiterten Modell war es möglich, Strahlungsausbrüche (Flares) im hochenergetischen Gamma-Bereich zu modellieren und den spektralen Verlauf eines Flares qualitativ korrekt zu bestimmen.

Im Einzelnen wurde nach einer Einführung in die Thematik (Kapitel 1), bei der die Verbundenheit des Themas mit zahlreichen anderen aktuellen Fragestellungen aus der Astrophysik und Kosmologie deutlich wurde, und der Erklärung einiger grundsätzlicher Zusammenhänge (Kapitel 2) zunächst das analytische Zweizonen-Modell nachgerechnet (Kapitel 3).

Der Vorteil einer Zweizonen-Geometrie wurde in Abschnitt 3.2 gründlich diskutiert und die Details des Modells in Abschnitt 3.3 vorgestellt. Bei einem Zweizonen-Modell wird die betrachtete Region unterteilt in eine Beschleunigungszone, in dem Teilchen (hier: Elektronen und Positronen) durch Schockbeschleunigung (siehe Kapitel 2.1.3) Energie gewinnen und durch Synchrotronstrahlung Energie verlieren und eine Strahlungszone, in der Teilchen nur noch Energie verlieren. Als wesentlich stellte sich heraus, dass es nur in einem solchen Modell möglich ist, das in manchen Quellen beobachtete ‘hard lag’-Verhalten zu erklären, bei dem das Spektrum einer Quelle während eines Flares zunächst weicher und dann erst härter wird. Bei den meisten Quellen wurde im Röntgenbereich das umgekehrte ‘soft lag’-Verhalten gesehen, das auch mit Einzonensmodellen leicht erklärbar ist. Es tritt auf, wenn der Kühlungsprozess bei größeren Energien effizienter wird, wie es bei der Synchrotronstrahlung der Fall ist, und so bei einem Flare, der durch eine vorübergehend gesteigerte Teilcheninjektion charakterisiert wird, zunächst mehr Strahlung im höherenergetischen Bereich auftritt, bis die Teilchen soweit gekühlt haben, dass das Spektrum abflacht, bevor es wieder seinen stationären Zustand annimmt.

Beim Nachrechnen des Modells wurden einige kleinere Fehler und Unvollständigkeiten im Originalpaper Kirk et al (1998) gefunden, die aber dank hilfreicher Diskussionen mit

Herrn Prof. John Kirk behoben werden konnten.

Im Kapitel 3 wurde auch kurz darauf eingegangen, wieso das analytische Modell am Ende doch numerisch wird und Versuche beschrieben, die transzendente Gleichung, die dafür verantwortlich ist, durch geeignete Ausdrücke zu nähern. Obgleich die Näherung für x_{cool} ausreichend gut war, war es nicht möglich, analytisch weiter zu rechnen, da die einzige in diesem Zusammenhang verwendbare Näherung für die Synchrotronemissivität, die monochromatische oder Delta-Näherung, die Spektren nur sehr verzerrt wiedergab.

Daraufhin wurden die Intensitäten der beiden Zonen numerisch bestimmt und diskutiert. Die gewünschten Verhalten in den Spektren ließen sich reproduzieren, insbesondere der spektrale Bruch bei einer durch die Größe der Quelle bestimmten Frequenz, wurde erzeugt. Die Reproduktionsphase wurde mit einem Fit an historische Daten für den Blazar Markarian 501 abgeschlossen.

Die Erweiterung des Modells um den Beitrag durch den Invers-Compton-Effekt (IC-Effekt) wurde in Kapitel 4 diskutiert. Dabei wurde zunächst aufgeführt, an welchen Stellen das Modell verändert werden müsste, um alle Auswirkungen des neu hinzugefügten Prozesses zu berücksichtigen. Nach vorsichtiger Abwägung wurde festgestellt, dass das gesuchte zeitabhängige IC-Spektrum in einer guten Näherung im Rahmen des semi-analytischen Modells bestimmt werden kann. Die sehr viel aufwändigere Berechnung der Energieverluste der Elektronen durch IC-Streuungen könnten nur in einem numerischen Modell angemessen berücksichtigt werden. Das zeitabhängige IC-Spektrum wurde dann in Abschnitt 4.3 vorgestellt und die Entstehung aus dem Synchrotronspektrum erläutert. Zum Schluss wurde die spektrale Energieverteilung von Mrk 501 modelliert. Dazu wurden das Synchrotron und IC-Spektrum an optische, Röntgen- und Gamma-Daten angepasst. Der so erzeugte Fit wies im Invers-Compton-Bereich eine etwas zu weiche Krümmung des Spektrums auf, so dass nur ein reduziertes χ^2 von 1.79 erreicht werden konnte. Die insgesamt aber dennoch gute Übereinstimmung von Modell und Beobachtungsdaten bei der Wahl von üblichen SSC-Fit-Parametern zeigte aber, dass die Erweiterung um den Invers-Compton-Effekt gelungen ist und die verwendeten Näherungen akzeptabel waren. Im Kapitel 5 ging es schließlich um die Variabilität der Spektren. Dazu wurde zunächst vorgestellt, wie ein Flare im Rahmen des Modells ‘erzeugt’ werden kann, nämlich durch kurzzeitige Erhöhung der Injektionsfunktion, und zu welcher Änderung in der Intensität dies führt. Die einfache Modellierung einer abrupten Zunahme und ebenso abrupten Normalisierung der Injektionsfunktion wurde dabei gewählt, weil so die Injektionsfunktion zeitunabhängig bleiben und die Linearität der Intensität ausgenutzt werden kann, um die Flare-Intensität zu bestimmen. In den folgenden Abschnitten 5.2 und 5.3 wurden Intensität und Spektralindex während eines Flares genauer untersucht und physikalische

Gründe für die Form der Spektren angegeben. In Abschnitt 5.4 wurde schließlich die aus Beobachter-Papieren gewohnte Darstellung für den spektralen Verlauf eines Flares gezeigt, nämlich der parametrische Plot Spektralindex gegen Intensität mit Kurvenparameter Zeit. In Abschnitt 5.5 wurden Zeitskalen für die Hysterese diskutiert. Dabei konnte mittels einer groben Abschätzung gezeigt werden, dass das Modell durchaus nicht nur für Stundenvariabilität geeignet ist, wie sie im Röntgenbereich gesehen und mit diesem Modell erklärt wurde. Mit gewissen Einschränkungen bei der Wahl der Parameter kann es auch die extrem kurzzeitige Variabilität von wenigen Minuten erklären, wie sie moderne Gamma-Teleskope für einige AGNs gemessen haben. Als sehr hoffnungsvoll fiel dabei im letzten Abschnitt des Kapitels, 5.6, auf, dass das spektrale Verhalten des Blazars Mrk 501 während eines Flares im Jahr 2005 qualitativ mit dem von dem Modell erzeugten Verlauf für spektrale Variabilität im entsprechenden Bereich des Spektrums übereinstimmt.

Bibliography

- Aharonian et al. (H.E.S.S. collaboration) 2006** AHARONIAN ET AL. (H.E.S.S. COLLABORATION), F. A.: A low level of extragalactic background light as revealed by γ -rays from blazars. In: *Nature* 440 (2006), april, p. 1018–1021
- Aharonian et al. (H.E.S.S. collaboration) 2007** AHARONIAN ET AL. (H.E.S.S. COLLABORATION), F. A.: Detection of VHE gamma-ray emission from the distant blazar 1ES 1101-232 with H.E.S.S. and broadband characterisation. In: *ArXiv e-prints* 705 (2007), may
- Albert et al. (MAGIC collaboration) 2007a** ALBERT ET AL. (MAGIC COLLABORATION), J.: Detection of Very High Energy Radiation from the BL Lacertae Object PG 1553+113 with the MAGIC Telescope. In: *Astrophysical Journal Letters* 654 (2007), january, p. L119–L122
- Albert et al. (MAGIC collaboration) 2007b** ALBERT ET AL. (MAGIC COLLABORATION), J.: Variable VHE Gamma-Ray emission from Markarian 501. In: *astro-ph/0702008* (2007)
- Antonucci 1993** ANTONUCCI, R.: Unified models for active galactic nuclei and quasars. In: *Annual Review of Astronomy and Astrophysics* 31 (1993), p. 473–521
- Ball and Kirk 1992** BALL, L. ; KIRK, J. G.: Diffusive acceleration of electrons in SN 1987A. In: *Astrophysical Journal Letters* 396 (1992), september, p. L39–L42
- Bhattacharyya et al 2002** BHATTACHARYYA, S. ; SAHAYANATHAN, S. ; KAUL, C. L.: Effect of Particle Acceleration Process on the Flare Characteristics of Blazars. In: *Journal of Astrophysics and Astronomy* 23 (2002), june, p. 95–+
- Blandford and Konigl 1979** BLANDFORD, R. D. ; KONIGL, A.: Relativistic jets as compact radio sources. In: *The Astrophysical Journal* 232 (1979), august, p. 34–48
- Blandford and Znajek 1977** BLANDFORD, R. D. ; ZNAJEK, R. L.: Electromagnetic extraction of energy from Kerr black holes. In: *Monthly Notices of the Royal Astronomical Society* 179 (1977), may, p. 433–456
- Blumenthal and Gould 1970** BLUMENTHAL, G. R. ; GOULD, R. J.: Bremsstrahlung, Synchrotron Radiation, and Compton Scattering of High-Energy Electrons Traversing Dilute Gases. In: *Reviews of Modern Physics* 42 (1970), p. 237–271
- Bronstein et al 2001** BRONSTEIN, I. N. ; SEMENDJAJEW, K. A. ; MUSIOL, G. ; MÜHLIG, H.: *Taschenbuch der Mathematik*. Harri Deutsch, 2001
- Buckley 1998** BUCKLEY, J. H.: ASTROPHYSICS: What the Wild Things Are. In: *Science* 279 (1998), january, p. 676–+
- Carroll and Ostlie 2006** CARROLL, B. W. ; OSTLIE, D. A.: *An introduction to modern astrophysics*. An introduction to modern astrophysics / B. W. Carroll and D. A. Ostlie. 2nd edition. San Francisco: Pearson, Addison-Wesley, ISBN 0-8053-0402-9. 2007, XVI+1278+A32+I31 pp., july 2006
- Catanese et al 1997** CATANESE, M. ; BRADBURY, S. M. ; BRESLIN, A. C. ; BUCKLEY, J. H. ; CARTER-LEWIS, D. A. ; CAWLEY, M. F. ; DERMER, C. D. ; FEGAN, D. J. ; FINLEY, J. P. ; GAIDOS, J. A. ; HILLAS, A. M. ; JOHNSON, W. N. ; KRENNRICH, F. ; LAMB, R. C. ; LESSARD, R. W. ; MACOMB, D. J. ; MCENERY, J. E. ; MORIARTY, P. ; QUINN, J. ; RODGERS, A. J. ; ROSE,

- H. J. ; SAMUELSON, F. W. ; SEMBROSKI, G. H. ; SRINIVASAN, R. ; WEEKES, T. C. ; ZWEERINK, J.: Multiwavelength Observations of a Flare from Markarian 501. In: *Astrophysical Journal Letters* 487 (1997), october, p. L143+
- Comastri et al 1997** COMASTRI, A. ; FOSSATI, G. ; GHISELLINI, G. ; MOLENDI, S.: On the Soft X-Ray Spectra of gamma -loud Blazars. In: *The Astrophysical Journal* 480 (1997), may, p. 534+
- Coppi 2002** COPPI, P. S.: Blazars – Theoretical Aspects. In: *The Universe Viewed in Gamma-Rays (Conference)*, 2002, p. 1–10
- Coppi and Blandford 1990** COPPI, P. S. ; BLANDFORD, R. D.: Reaction rates and energy distributions for elementary processes in relativistic pair plasmas. In: *Monthly Notices of the Royal Astronomical Society* 245 (1990), august, p. 453–507
- Dermer and Schlickeiser 1993** DERMER, C. D. ; SCHLICKEISER, R.: Model for the High-Energy Emission from Blazars. In: *The Astrophysical Journal* 416 (1993), october, p. 458+
- Dondi and Ghisellini 1995** DONDI, L. ; GHISELLINI, G.: Gamma-ray-loud blazars and beaming. In: *Monthly Notices of the Royal Astronomical Society* 273 (1995), april, p. 583–595
- Felten and Morrison 1966** FELTEN, J. E. ; MORRISON, P.: Omnidirectional Inverse Compton and Synchrotron Radiation from Cosmic Distributions of Fast Electrons and Thermal Photons. In: *The Astrophysical Journal* 146 (1966), december, p. 686+
- Fermi 1949** FERMI, E.: On the Origin of the Cosmic Radiation. In: *Physical Review* 75 (1949), april, p. 1169–1174
- Gear et al 1986** GEAR, W. K. ; ROBSON, E. I. ; BROWN, L. M. J.: Infrared variability of the BL Lacertae object OJ287 since its outburst in 1983. In: *Nature* 324 (1986), december, p. 546+
- Gehrels and Michelson 1999** GEHRELS, N. ; MICHELSON, P.: GLAST: the next-generation high energy gamma-ray astronomy mission. In: *Astroparticle Physics* 11 (1999), june, p. 277–282
- Ginzburg and Syrovatskii 1964** GINZBURG, V. L. ; SYROVATSKII, S. I.: *The Origin of Cosmic Rays*. The Origin of Cosmic Rays, New York: Macmillan, 1964, 1964
- Ginzburg and Syrovatskii 1965** GINZBURG, V. L. ; SYROVATSKII, S. I.: Cosmic Magnetobremstrahlung (synchrotron Radiation). In: *Annual Review of Astronomy and Astrophysics* 3 (1965), p. 297+
- Hayashida et al. 2007, to be published** HAYASHIDA ET AL., M.: Wide-range multiwavelength observations of northern TeV blazars with MAGIC/HESS, Suzaku and KVA. In: *Proceedings of the 30th International Cosmic Ray Conference, Merida, Yucatan, Mexiko*, 2007, to be published, p. –
- Jauch and Rohrlich 1976** JAUCH, J. M. ; ROHRLICH, F.: *The theory of photons and electrons. The relativistic quantum field theory of charged particles with spin one-half*. Texts and Monographs in Physics, New York: Springer, 1976, 2nd ed., 1976
- Jones 1994** JONES, F. C.: A theoretical review of diffusive shock acceleration. In: *The Astrophysical Journal Supplement Series* 90 (1994), february, p. 561–565
- Jones and Ellison 1991** JONES, F. C. ; ELLISON, D. C.: The plasma physics of shock acceleration. In: *Space Science Reviews* 58 (1991), p. 259–346
- Jones 1968** JONES, Frank C.: Calculated Spectrum of Inverse-Compton-Scattered Photons. In: *Phys. Rev.* 167 (1968), Mar, Nr. 5, p. 1159–1169

- Kardashev 1962** KARDASHEV, N. S.: Nonstationarity of Spectra of Young Sources of Nonthermal Radio Emission. In: *Soviet Astronomy* 6 (1962), december, p. 317–+
- Katarzyński et al 2001** KATARZYŃSKI, K. ; SOL, H. ; KUS, A.: The multifrequency emission of Mrk 501. From radio to TeV gamma-rays. In: *Astronomy and Astrophysics* 367 (2001), march, p. 809–825
- Kirk et al 1998** KIRK, J. G. ; RIEGER, F. M. ; MASTICHIADIS, A.: Particle acceleration and synchrotron emission in blazar jets. In: *Astronomy and Astrophysics* 333 (1998), may, p. 452–458
- Kneiske et al 2004** KNEISKE, T. M. ; BRETZ, T. ; MANNHEIM, K. ; HARTMANN, D. H.: Implications of cosmological gamma-ray absorption. II. Modification of gamma-ray spectra. In: *Astronomy and Astrophysics* 413 (2004), january, p. 807–815
- Krawczynski et al 2004** KRAWCZYNSKI, H. ; HUGHES, S. B. ; HORAN, D. ; AHARONIAN, F. ; ALLER, M. F. ; ALLER, H. ; BOLTWOOD, P. ; BUCKLEY, J. ; COPPI, P. ; FOSATI, G. ; GOETTING, N. ; HOLDER, J. ; HORNS, D. ; KURTANIDZE, O. M. ; MARSCHER, A. P. ; NIKOLASHVILI, M. ; REMILLARD, R. A. ; SADUN, A. ; SCHROEDER, M.: Multiwavelength Observations of Strong Flares From the TeV-Blazar 1ES 1959+650. In: *The Astrophysical Journal* 601 (2004), p. 151. – URL <http://www.citebase.org/abstract?id=oai:arXiv.org:astro-ph/0310158>
- Longair 1994** LONGAIR, Malcom S.: *High Energy Astrophysics, Volume 2 (Stars, the galaxy and the interstellar medium)*. 2. Cambridge University Press, 1994
- Mannheim 1993** MANNHEIM, K.: The proton blazar. In: *Astronomy and Astrophysics* 269 (1993), march, p. 67–76
- Mannheim and Biermann 1992** MANNHEIM, K. ; BIERMANN, P. L.: Gamma-ray flaring of 3C 279 - A proton-initiated cascade in the jet? In: *Astronomy and Astrophysics* 253 (1992), january, p. L21–L24
- Meier et al 2001** MEIER, D. L. ; KOIDE, S. ; UCHIDA, Y.: Magnetohydrodynamic Production of Relativistic Jets. In: *Science* 291 (2001), january, p. 84–92
- Melrose 1980** MELROSE, D. B.: *Plasma astrophysics. Nonthermal processes in diffuse magnetized plasmas - Vol.1: The emission, absorption and transfer of waves in plasmas; Vol.2: Astrophysical applications*. New York: Gordon and Breach, 1980, 1980
- Meyberg and Vachenaue 2003** MEYBERG, Kurt ; VACHENAUER, Peter: *Höhere Mathematik 2*. 4th. Springer, 2003
- Mirabel and Rodriguez 2002** MIRABEL, I. F. ; RODRIGUEZ, L. F.: Microquasars in the Milky Way. In: *Sky and Telescope* 103 (2002), may, Nr. 5, p. 32–+
- Mukherjee 2002** MUKHERJEE, R.: Blazars – Observational Aspects. In: *The Universe Viewed in Gamma-Rays (Conference)*, 2002, p. 1–10
- Pelletier 1997** PELLETIER, G.: High Energy Plasma Physics in Black Hole Environment with Jets. In: GIRAUD-HERAUD, Y. (Editor) ; TRAN THANH VAN, J. (Editor): *Very High Energy Phenomena in the Universe; Moriond Workshop*, 1997, p. 27–+
- Rachen 2001** RACHEN, J. P.: Hadronic Correlated Flares from Mrk 501. In: AHARONIAN, F. A. (Editor) ; VÖLK, H. J. (Editor): *American Institute of Physics Conference Series*, 2001, p. 704–+
- Rachen and Enßlin 2007** RACHEN, J.P. ; ENSSLIN, T.: Testing the consistency of blazar

Bibliography

- emission models by submillimetre to FIR observations (in preparation). (2007)
- Rees 1984** REES, M. J.: Black Hole Models for Active Galactic Nuclei. In: *Annual Review of Astronomy and Astrophysics* 22 (1984), p. 471–506
- Rieger 2006** RIEGER, F. M.: Fermi acceleration in astrophysical jets. In: *ArXiv Astrophysics e-prints* (2006)
- Rieger and Mannheim 2000** RIEGER, F. M. ; MANNHEIM, K.: Implications of a possible 23 day periodicity for binary black hole models in Mkn 501. In: *Astronomy and Astrophysics* 359 (2000), july, p. 948–952
- Romani 2006** ROMANI, R. W.: The Spectral Energy Distribution of the High-z Blazar Q0906+6930. In: *The Astronomical Journal* 132 (2006), november, p. 1959–1963
- Rybicki and Lightman 1979** RYBICKI, George B. ; LIGHTMAN, Alan P.: *Radiative Processes in Astrophysics*. John Wiley & Sons, 1979
- Schlickeiser 2002** SCHLICKEISER, R.: *Cosmic Ray Astrophysics*. Cosmic ray astrophysics / Reinhard Schlickeiser, Astronomy and Astrophysics Library; Physics and Astronomy Online Library. Berlin: Springer. ISBN 3-540-66465-3, 2002, XV + 519 pp., 2002
- Sembay et al 1993** SEMBAY, S. ; WARWICK, R. S. ; URRY, C. M. ; SOKOLOSKI, J. ; GEORGE, I. M. ; MAKINO, F. ; OHASHI, T. ; TASHIRO, M.: The X-ray spectral variability of the BL Lacertae type object PKS 2155-304. In: *The Astrophysical Journal* 404 (1993), february, p. 112–123
- Sigl 2001** SIGL, G.: Ultrahigh-Energy Cosmic Rays: Physics and Astrophysics at Extreme Energies. In: *Science* 291 (2001), january, p. 73–79
- Sikora et al 1994** SIKORA, M. ; BEGELMAN, M. C. ; REES, M. J.: Comptonization of diffuse ambient radiation by a relativistic jet: The source of gamma rays from blazars? In: *The Astrophysical Journal* 421 (1994), january, p. 153–162
- Spergel et al 2007** SPERGEL, D. N. ; BEAN, R. ; DORÉ, O. ; NOLTA, M. R. ; BENNETT, C. L. ; DUNKLEY, J. ; HINSHAW, G. ; JAROSIK, N. ; KOMATSU, E. ; PAGE, L. ; PEIRIS, H. V. ; VERDE, L. ; HALPERN, M. ; HILL, R. S. ; KOGUT, A. ; LIMON, M. ; MEYER, S. S. ; ODEGARD, N. ; TUCKER, G. S. ; WEILAND, J. L. ; WOLLACK, E. ; WRIGHT, E. L.: Three-Year Wilkinson Microwave Anisotropy Probe (WMAP) Observations: Implications for Cosmology. In: *The Astrophysical Journal Supplement Series* 170 (2007), june, p. 377–408
- Takahashi et al 1996** TAKAHASHI, T. ; TASHIRO, M. ; MADEJSKI, G. ; KUBO, H. ; KAMAE, T. ; KATAOKA, J. ; KII, T. ; MAKINO, F. ; MAKISHIMA, K. ; YAMASAKI, N.: ASCA Observation of an X-Ray/TeV Flare from the BL Lacertae Object Markarian 421. In: *Astrophysical Journal Letters* 470 (1996), october, p. L89+
- Tavecchio et al 1998** TAVECCHIO, F. ; MARASCHI, L. ; GHISELLINI, G.: Constraints on the Physical Parameters of TeV Blazars. In: *The Astrophysical Journal* 509 (1998), december, p. 608–619
- Urry and Padovani 1995** URRY, C. M. ; PADOVANI, P.: Unified Schemes for Radio-Loud Active Galactic Nuclei. In: *Publications of the Astronomical Society of the Pacific* 107 (1995), september, p. 803–+
- Webb et al 1984** WEBB, G. M. ; DRURY, L. O. ; BIERMANN, P.: Diffusive shock acceleration of energetic electrons subject to synchrotron losses. In: *Astronomy and Astrophysics* 137 (1984), august, p. 185–201

A Acknowledgements

This work would not be what it is without the support of many people.

I would like to thank

- Prof. Dr. Karl Mannheim for motivating the work and for giving me the opportunity to work in his group. I am also very grateful for the opportunity to get to know many interesting aspects of theoretical astrophysics.
- Dr. Felix Spanier for his support concerning problems of all kinds, especially mathematical problems, and for insights into the art of programming with Mathematica.
- Prof. Dr. John Kirk of the Max-Planck-Institut für Kernphysik, Heidelberg, for his patience in answering my questions and for two very helpful discussions.
- My roommates and colleagues Dominik Elsässer, Tobias Hein, Surajit Paul, Michael Rieger and Tobias Viering for many fruitful and interesting discussions, not just about astrophysics.
- Stefan Rügamer and Markus Meyer of the MAGIC collaboration for giving many useful insights into observational gamma ray astronomy.
- Gisela Heyder for much help with bureaucracy.

I also acknowledge helpful talks and e-mail correspondence with Dr. Jörg Rachen (MPA, Garching), Dr. Daniel Kranich (ETH, Zürich), Dr. Dieter Horns (Institut für Astronomie und Astrophysik, Universität Tübingen) and Dr. David Paneque (Kavli Institute for Particle Astrophysics and Cosmology, Stanford University).

Apart from technical help from the people stated above I gratefully acknowledge material and immaterial support from my family during all of my studies in physics and astrophysics. I would especially like to thank my parents, Dr. Irmgard and Dr. Helmut Burtscher, and my fiancée, Cordula Overesch, for support over many years.

A Acknowledgements

B Numerical Calculations with Mathematica

For the numerical calculations involved in solving the transcendental equation for x_{cool} Eq. (3.46) and for the numerical integrations that followed to calculate the synchrotron and Inverse Compton spectra, the computer-algebra software MATHEMATICA (version 6.0) by Wolfram Research Inc. was used. MATHEMATICA offers a functional programming language similar to C with a huge library of mathematical functions including the most widely used strategies for numerical integrations within the `NIntegrate` command. The strategy is automatically chosen to best fit the kind of integrand. `NIntegrate` also automatically chooses the kind of adaptive integration method that fits best to the integrand providing a higher resolution at regions where the integrand changes quickly.

The structure of my program (see listing, Appendix C) – consisting of three ‘Notebook’ (`.nb`) files in MATHEMATICA – is as follows: all definitions that do not change (constants, functions) are in `Init.nb` which has to be loaded into memory before the actual integrations are performed in the notebook `Run.nb`. In the latter notebook also all model parameters (`JetB`, `usinc`, `tescintacc`, γ_0 , γ_{max} , `JetDoppler`, `K`, `tbintacc`, `RJet`) are defined so that multiple sets of parameters can be tested easily. The data files (one for each time step) are then exported in `HDF5` format into the directory specified at the beginning of `Run.nb` and read into `Plot.nb` where the evaluation takes place. The evaluation then includes generation of the time-independent spectrum (`tbarintacc=500`) and the evolution of spectral index and intensity over time for a certain frequency. Finally the parametric plot spectral index vs. intensity is generated.

In Mathematica front end (notebook editor) and back end (‘kernel’) are two separate processes that can be run on different machines by defining remote kernels. That’s why calculation and evaluation were split up in two different notebooks: multiple `Run.nb` files can so be run on different ‘kernels’ on different machines, thus parallelising the computation and achieving a result much quicker (or much better resolved) than when computing on a single machine.

C Program Listing

C.1 Init.nb

Natural constants (all in CGS)

```
elementarQ = 4.803*^-10(*esu*);  
me = 9.109*^-28(*g*);  
c = 2.998*^10(*cm/s*);  
h = 6.626*^-27(*erg s*);  
eVinerg = 1.602*^-12;  
r0 =  $\frac{\text{elementarQ}^2}{\text{mec}^2}$ ; (*CGS*)  
 $\sigma T = 6.653*^-25$ ; (*incm^2*)
```

Other relations

```
as:=Sqrt[3]elementarQ^2 $\Omega$ /(2Pic); (*CGS*)  
 $\beta s := \frac{4}{3} \frac{\sigma T}{\text{mec}} \frac{\text{JetB}^2}{8\text{Pi}}$ ; (*1/s; ausBlumenthal&Gould1970*)  
 $a := Q0\text{tacc}\gamma0^{(1/\text{tescintacc})} \left(1 - \frac{\gamma0}{\gamma\text{max}}\right)^{-1/\text{tescintacc}}$ ; (*1/cm^2*)  
 $\Omega := \text{elementarQJetB}/(\text{mec})$ ; (*1/s*)  
 $\beta IC := \frac{4}{3} \frac{\sigma T}{\text{mec}} \text{urad}$ ; (*1/s;  
ausBlumenthal&Gould1970*)  
 $\nu\text{max}[t\text{barintacc}] := 3.7*^6\gamma1[t\text{barintacc}]^2\text{JetB}$   
 $\nu\text{maxmax} := 3.7*^6\gamma\text{max}^2\text{JetB}$   
 $\nu\text{maxmaxobs} := 3.7*^6\gamma\text{max}^2\text{JetB} * 2\text{JetDoppler}$ 
```

Dependent model parameters

```
 $\gamma\text{maxin}\gamma0 := \gamma\text{max}/\gamma0$   
tacc:=1/( $\beta s\gamma\text{max}$ )  
Q0:=0.1cK(*1/(cm^2s)*)
```

Exact solution for y (xcool)

```

ynumerischnorel[logγ-, tbarintacc-]:=
y/.FindRoot [  $\frac{\gamma_{\max}}{10^{\log\gamma}} - tbarintacc + y(1 - usinc) == 1 + (\gamma_{\max} \gamma_0 - 1) \text{Exp}[-y]$ ,
{y, 0} ]
yexaktnorel[logγ-, tbarintacc-]:=
Max[ynumerischnorel[logγ, tbarintacc], tbarintacc - tbintacc]

```

Electron density in radiation zone with exact solution for y (xcool)

```

nradexaktnorel[logγ-, tbarintacc-]:=
Re [ If [ tbarintacc > (1 - usinc) Log [  $\frac{(\gamma_{\max} \gamma_0) - 1}{\frac{\gamma_{\max}}{10^{\log\gamma}} - 1}$  ],
 $\frac{a}{(1 - usinc) \gamma_{\max}^{1/tescintacc + 1}} \left( \frac{\gamma_{\max}}{10^{\log\gamma}} \right)^2$ 
 $\left( \left( \frac{\gamma_{\max}}{10^{\log\gamma}} - 1 \right)^{\frac{1}{tescintacc}} - \left( \frac{\gamma_{\max}}{10^{\log\gamma}} - tbarintacc - 1 + (1 - usinc) yexaktnorel[log\gamma, tbarintacc] \right)^{\frac{1}{tescintacc}} \right), 0 ] ] ;$ 

```

Synchrotron emissivity

```

γ1[tbarintacc-]:=  $\left( \frac{1}{\gamma_{\max}} + \left( \frac{1}{\gamma_0} - \frac{1}{\gamma_{\max}} \right) \text{Exp}[-tbarintacc] \right)^{-1}$ 

```

Melrose approximation

```

znorel[logγ-, logν-]:=  $\frac{4\pi 10^{\log\nu}}{3\Omega \frac{\pi}{4} 10^{2\log\gamma}}$  (*mitSinus - Mittelung*)
SynchrotronPnorel[logγ-, logν-]:=
asznoel[logγ, logν]^0.3 Exp[-znorel[logγ, logν]]

```

Synchrotron spectrum rad zone numerical - Definition of

IO

Multiplied with $10^{\log\gamma}$,
since the integration is over $\log\gamma$, not over γ ...

```

I0norel[logν_, tbarintacc.] :=
NIntegrate [10logγ SynchrotronPnorel[logγ, logν]
nradexaktnorel[logγ, tbarintacc],
{logγ, Log[10, γ0], Log[10, γ1[tbarintacc]]}, WorkingPrecision → 10]

```

Synchrotron spectrum acc zone numerical - Definition of Is and nacc

```

naccnorel[logγ_, tbarintacc.] :=

$$\frac{a}{(1 - \text{usinc}) \gamma_{\text{max}}^{1/\text{tescintacc} + 1}} \frac{\gamma_{\text{max}}^2}{10^{2 \log \gamma}} \left( \frac{\gamma_{\text{max}}}{10^{\log \gamma}} - 1 \right)^{1/\text{tescintacc} - 1}$$

UnitStep[Log[10, γ1[tbarintacc]] - logγ]
Multipliedwith10logγ,
sincetheintegrationisoverlogγ, notoverγ...
Isnorel[logν_, tbarintacc.] :=
NIntegrate [10logγ SynchrotronPnorel[logγ, logν]
naccnorel[logγ, tbarintacc],
{logγ, Log[10, γ0], Log[10, γ1[tbarintacc]]}, WorkingPrecision → 10]

```

Total observed synchrotron intensity (acc + rad zone) incl. Doppler factor - Definition of Iobs

```

I1[logν_, tbarintacc.] :=
I0norel[logν, tbarintacc] + Isnorel[logν, tbarintacc]

```

Definition of Iobs with the ratio of projected jet diameter / distance to blazar, Doppler factor for intensity (boosting) and blue-shift (Observed intensity at ν is related to emitted intensity at ν/δ).

```

Iobs[logν_, tbarintacc.] :=
(PiRJet2) / (DBlazar2) 8JetDoppler3
I1[logν + Log[10, 2JetDoppler], tbarintacc]

```

IC kernel (Blumenthal & Gould)

```

G[q_, Γ_] := 2q Log[q] + (1 + 2q)(1 - q) +  $\frac{1}{2} \frac{(\Gamma q)^2}{1 + \Gamma q} (1 - q)$ 
F[ε1_, ε_, γ_] := If  $\left[ \frac{\frac{\epsilon_1}{\gamma_{\text{mec}}^2}}{\frac{4\epsilon\gamma}{\text{mec}^2} \left(1 - \frac{\epsilon_1}{\gamma_{\text{mec}}^2}\right)} \leq 1 \&\& \frac{\frac{\epsilon_1}{\gamma_{\text{mec}}^2}}{\frac{4\epsilon\gamma}{\text{mec}^2} \left(1 - \frac{\epsilon_1}{\gamma_{\text{mec}}^2}\right)} \geq 1 / (4\gamma^2) \right,$ 

```

$$\frac{2\text{Pi}r_0^2 m e^2 c^5}{\gamma^2 \epsilon} G \left[\frac{\frac{\epsilon_1}{\gamma m e c^2}}{\frac{4\epsilon\gamma}{m e c^2} \left(1 - \frac{\epsilon_1}{\gamma m e c^2}\right)}, \frac{4\epsilon\gamma}{m e c^2} \right], 0 \right]$$

C.2 Run.nb

Modell Parameters

```

JetB = 0.7;
(*G*)
usinc = 0.1;
tescintacc = 2;
 $\gamma_0 = 1$ ;
 $\gamma_{\max} = 5^{*6}$ ;
JetDoppler = 10;
 $K = 7.2^{*5}$ ; (*cm^ - 3*)
tbintacc = 100;

```

Other source-specific parameters, here: Mrk 501

```

DBlazar =  $4.55^{*26}$ ; (*Luminositydistanceforz = 0.034, H0 = 71,
cm*)

```

Synchrotron

Set directory and initiaise array

```

SetDirectory[
"/Users/leo/Documents/Studium/Astro/Diplomarbeit/Mathematica-Files/MMA-
DATA/"];

```

Loop to calculate several timesteps in a single evaluation

```

tbarintaccmin = 4;
tbarintaccmax = 50;
syndataobs = Table[i, {i, 1, tbarintaccmax}];
icdataobs = Table[i, {i, 1, tbarintaccmax}];
Until tbarintacc = 4 nothing happens at all (emission only below  $\nu = 1^{*9}$  Hz, so probably
self-absorbed and not of interest here)
For[tbarintacc = tbarintaccmin, tbarintacc  $\leq$  tbarintaccmax, tbarintacc++,
tablesyn =

```

```

Timing [Table [{10log $\nu$ , I1[log $\nu$ , tbarintacc]},
{log $\nu$ , 13, Log[10,  $\nu$ max[tbarintacc] + 1, 0.1}}];
syn = Re[tablesyn[[2]]];
syndataobs[[tbarintacc]] =
Transpose[{Map[#[[1]]&, syn] * 2JetDoppler,
Map[#[[1]]&, syn] * 2JetDoppler (PiRJet2) / (DBlazar2) 8
JetDoppler3Map[#[[2]]&, syn]}];
Export["syndataobs" <> ToString[tbarintacc] <> ".h5",
syndataobs[[tbarintacc]]];
n $\gamma$ r = Interpolation [Table [{10log $\gamma$ , nradexaktnorel[log $\gamma$ , tbarintacc]},
{log $\gamma$ , 0, Log[10,  $\gamma$ 1[tbarintacc]], 0.01}}];
n $\gamma$ a = Interpolation [Table [{10log $\gamma$ , naccnorel[log $\gamma$ , tbarintacc]},
{log $\gamma$ , 0, Log[10,  $\gamma$ 1[tbarintacc]] - 0.01, 0.01}}];
n $\epsilon$ rad =
Interpolation [Table [{h10log $\nu$ , IOnorel[log $\nu$ , tbarintacc]/(10(log $\nu$ ) * h)},
{log $\nu$ , 9, Log[10,  $\nu$ max[tbarintacc] + 0.2, 0.1}}];
log $\epsilon$ radmin = Log[10, n $\epsilon$ rad[[1]][[1]][[1]]];
log $\epsilon$ radmax = Log[10, n $\epsilon$ rad[[1]][[1]][[2]]];
n $\epsilon$ acc =
Interpolation [Table [{h10log $\nu$ , Isnorel[log $\nu$ , tbarintacc]/(10(log $\nu$ ) * h)},
{log $\nu$ , 9, Log[10,  $\nu$ max[tbarintacc] + 0.2, 0.1}}];
log $\epsilon$ accmin = Log[10, n $\epsilon$ acc[[1]][[1]][[1]]];
log $\epsilon$ accmax = Log[10, n $\epsilon$ acc[[1]][[1]][[2]]];
tableic =
Timing[
Table[
{10log $\epsilon$ 1, NIntegrate [(n $\epsilon$ rad [10log $\epsilon$ ] n $\gamma$ r[ $\gamma$ ] + n $\epsilon$ acc [10log $\epsilon$ ] n $\gamma$ a[ $\gamma$ ])
F [10log $\epsilon$ 1, 10log $\epsilon$ ,  $\gamma$ ] 10log $\epsilon$ , {log $\epsilon$ , log $\epsilon$ radmin, log $\epsilon$ radmax},
{ $\gamma$ , 1,  $\gamma$ 1[tbarintacc]}]}, {log $\epsilon$ 1, -4.5, 1.5, 0.1}}];
ic = Re[tableic[[2]]];
icI =
Transpose[{Map[#[[1]]&, ic]/h,
(Map[#[[1]]&, ic)/h)hMap[#[[2]]&, ic}];
icdataobs[[tbarintacc]] =
Transpose[{Map[#[[1]]&, icI] * 2JetDoppler,
Map[#[[1]]&, icI] * 2JetDoppler (PiRJet2) / (DBlazar2) 8
}];

```

```
JetDoppler^3Map[#[[2]]&, icI}];  
Export["icdataobs" <> ToString[tbarintacc] <> ".h5",  
icdataobs[[tbarintacc]]];  
]
```

Plot.nb

Model

```
SetDirectory[
"/Users/leo/Documents/Studium/Astro/Diplomarbeit/Mathematica-Files/MMA-
DATA/"];
tbarintaccmin = 4;
tbarintaccmax = 50;
```

Synchrotron data

```
syndata = Table[i, {i, 1, 500}];
For[tbarintacc = tbarintaccmin, tbarintacc ≤ tbarintaccmax,
tbarintacc++, syndata[[tbarintacc]] =
Import["syndataobs" <> ToString[tbarintacc] <> ".h5",
{"Datasets", "/Dataset1"}]]
syndata[[500]] = Import["syndataobs500.h5", {"Datasets", "/Dataset1"}];
```

IC data

```
icdata = Table[i, {i, 1, 500}];
For[tbarintacc = tbarintaccmin, tbarintacc ≤ tbarintaccmax,
tbarintacc++, icdata[[tbarintacc]] =
Import["icdataobs" <> ToString[tbarintacc] <> ".h5",
{"Datasets", "/Dataset1"}]]
icdata[[500]] = Import["icdataobs500.h5", {"Datasets", "/Dataset1"}];
```

Plot spectra

Temporal evolution

```
ListLogLogPlot[{syndata[[20;50]]}, Joined → True]
```

Time - independent spectrum

```
ListLogLogPlot[{syndata[[500]]}, Joined → True]
```

Produce flares (Synchrotron + IC)

```

synflaredata[frqpart.]:=
Table[{tbarintacc, syndata[[500, frqpart, 2]]+
(If[Length[syndata[[tbarintacc]]] ≥ frqpart,
syndata[[tbarintacc, frqpart, 2]], 0)}-
If[tbarintacc - 10 > 1, If[Length[syndata[[tbarintacc - 10]]] ≥ frqpart,
syndata[[tbarintacc - 10, frqpart, 2]], 0, 0)}],
{tbarintacc, 2, tbarintaccmax}]
icflaredata[frqpart.]:=
Table[
{tbarintacc, icdata[[500, frqpart, 2]]+
2(If[Length[icdata[[tbarintacc]]] ≥ frqpart,
icdata[[tbarintacc, frqpart, 2]], 0)}-
If[tbarintacc - 10 > 1, If[Length[icdata[[tbarintacc - 10]]] ≥ frqpart,
icdata[[tbarintacc - 10, frqpart, 2]], 0, 0)}],
{tbarintacc, 2, tbarintaccmax}]
ListPlot[{synflaredata[51]}, Joined → True]
ListPlot[{icflaredata[51]}, Joined → True]

```

Spectral index

```

αdatasyn[frqpart.]:=
Table[
{tbarintacc,
Log[10, If[Length[syndata[[tbarintacc]]] ≥ frqpart + 1,
synflaredata[frqpart + 1][[tbarintacc, 2]], 0]/
synflaredata[frqpart][[tbarintacc, 2]]]/
Log[10, syndata[[500, frqpart + 1, 1]]/syndata[[500, frqpart, 1]]]},
{tbarintacc, tbarintaccmin, tbarintaccmax - 1}]
αdataic[frqpart.]:=
Table[
{tbarintacc,
Log[10, If[Length[icdata[[tbarintacc]]] ≥ frqpart + 1,
icflaredata[frqpart + 1][[tbarintacc, 2]], 0]/
icflaredata[frqpart][[tbarintacc, 2]]]/

```

```
Log[10, icdata[[500, frqpart + 1, 1]]/icdata[[500, frqpart, 1]]],  
{tbarintacc, 9, tbarintaccmax - 1}]  
ListPlot[ $\alpha$ datasyn[50], PlotRange  $\rightarrow$  All, Joined  $\rightarrow$  True]  
ListPlot[ $\alpha$ dataic[50], PlotRange  $\rightarrow$  All, Joined  $\rightarrow$  True]
```

Hysteresis

Adjust these values according to your set of parameters! Depending on the parameter set the flare will start at different times.

```
a = 5;  
b = 3;  
imin = 6;  
imax = 43;  
ai = 5;  
bi = 3;  
imini = 6;  
imaxi = 43;  
synhystdata[frqpart.]:=  
Table[{synflaredata[frqpart][[i + a, 2]],  $\alpha$ datasyn[frqpart][[i + b, 2]]},  
{i, imin, imax}];  
ichystdata[frqpart.]:=  
Table[{icflaredata[frqpart][[i + ai, 2]],  $\alpha$ dataic[frqpart][[i + bi, 2]]},  
{i, imini, imaxi}];
```

D Eigenständigkeitserklärung (Declaration of Autonomy)

Hiermit erkläre ich, dass ich die vorliegende Arbeit ohne unerlaubte fremde Hilfe angefertigt und keine anderen als die angegebenen Hilfsmittel und Quellen verwendet habe.

Würzburg, 3. Juli 2007

Leonard Burtscher